Development of Nanostructured Polyaniline-Based Electrode Materials for High-Performance Supercapacitors

by

Ali Khosrozadeh

A Thesis submitted to the Faculty of Graduate Studies of
the University of Manitoba
in partial fulfilment of the requirements of the degree of

Doctor of Philosophy

Department of Mechanical Engineering
Faculty of Engineering
University of Manitoba
Winnipeg, Canada

Abstract

Electrochemical energy storage and conversion devices are among clean energy technologies that play an important role in overcoming global pollution and utilizing sustainable and renewable energy resources. Supercapacitors (SCs) are an important class of energy storage devices owing to their fast charge-discharge rate, high power density, low maintenance, and long cycle life. They bridge the gap between conventional capacitors and rechargeable batteries and are most useful in applications that require a fast power boost and delivery. Electrode materials play a vital role in the performance of SCs and thus the prospect of developing proper electrode materials is an exciting direction in the field. Polyaniline (PAni) is a promising conducting polymer with the advantages of high pseudocapacitance, environmental stability, low cost and ease of synthesis. However, there are few shortcomings that limit the practical application of PAni as an electrode material for SCs. PAni suffers from poor cycle life which considerably compromises the advantage of long cycle life of SCs over batteries. In addition, it is difficult to produce mechanically robust films from pristine PAni since it is a brittle material. To overcome the limitations of PAni, this thesis explores various approaches to construct a flexible PAni-based composite film by combining PAni with other nanomaterials. This is achieved by utilizing several nanostructures in one composite with multiple benefits to address the disadvantages of individual components. A low-cost PAni-based electrode for solid-state SCs is developed on the basis of PAni and acid-treated carbon particles. Phytic acid is utilized as a crosslinker and co-dopant of PAni, and a gel electrolyte is used to address the poor cycle life of PAni. Later on, a new strategy to construct a flexible PAni-based electrode with an adjustable mass-loading of active materials is introduced. Cellulose is employed as a backbone

for a composite film of PAni, reduced graphene oxide, and silver nanowires. In a similar approach, a flexible electrode for high-performance SCs is developed on basis of PAni, cellulose, graphite-based exfoliated graphite, and silver nano-particles. This strategy allows designing composite electrodes with large surface area and porosity, and adjustable energy and power densities. The fabricated SC shows a combination of good rate capability, cycling stability and high areal specific capacitance. Another strategy to construct a flexible PAni-based electrode and address the poor cycle life of PAni is growing PAni on nanofibrous and cushiony substrates. A flexible electrode for SCs with a remarkable cycling stability is developed using electrospun polyurethane as a cushiony support for growing flower-like PAni. Moreover, a novel flexible electrode is constructed by growing PAni on graphene-coated cross-linked polyvinyl alcohol nanofibers. The as-prepared SC maintains its capacitive performance for 84k cycles of charge-discharge at 35 mA indicating an extraordinary cycling stability. In addition, PAni-coated nanofibrous film show a unique acid-base shape memory phenomenon which could be utilized in chemo-mechanical actuation devices.

Acknowledgments

I would like to express my sincerest thanks to my supervisor, Dr. Malcolm Xing, for his guidance and encouragement throughout the course of this research. Dr. Xing has been so influential in ensuring my academic and professional well-being ever since I started to work with him. Without his constant support, this work would not have been possibly done. I also would like to show gratitude to my advisory committee members, Dr. Yunhua Luo and Dr. Jun Cai, for their advice and their constructive comments on my thesis. I would like to express my appreciation to Dr. Heather Andreas from Dalhousie University for her through review of my thesis and constructive comments. Many thanks to my former supervisor professor Quan Wang for his continuous support and encouragement.

I would like to thank my friends in Winnipeg as well as current and former colleagues in Dr. Xing's lab for their support. Special thanks to Dr. Yuqing Liu and Mohammad Ali Darabi.

I am thankful to Dr. Michael S. Freund letting me use his electrochemical testing facilities in 2013. I also thank Dr. Michael McDonald for showing me how to operate of Solartron 1287.

I acknowledge the funding received from the NSERC Discovery Grant and the University of Manitoba Graduate Fellowship to support this research. I appreciate the Department of Mechanical Engineering crew for their support during my PhD. I really enjoyed working and teaching in this department.

I wish to thank my parents, brother and sister for their love and support in every stage of my life. Finally, I am undoubtedly grateful to the most important person in my life, my wife Anna for her love, support, encouragement, and patience during this difficult journey.

Dedication

To my wife, parents, brother and sister

Contributions of Authors

This thesis is comprised of four published journal papers and a prepared manuscript. Ali Khosrozadeh is the first author and the major contributor in all papers. In chapter 5, M. A. Darabi carried out the PU electrospinning procedure. In chapter 6, G. Singh performed some of the PVA electrospinning procedure and PVA crosslinking experiment.

List of Copyrighted Material

- Khosrozadeh, A.; Xing, M.; Wang, Q., A High-Capacitance Solid-State Supercapacitor Based on Free-Standing Film of Polyaniline and Carbon Particles. *Applied Energy* 2015, 153 (0), 87-93. Copyright (2015) Elsevier. The whole content of this paper is included in Chapter 2.
- Khosrozadeh, A.; Darabi, M. A.; Xing, M.; Wang, Q., Flexible Cellulose-Based Films of Polyaniline–Graphene–Silver Nanowire for High-Performance Supercapacitors. *Journal of Nanotechnology in Engineering and Medicine* 2015, 6 (1), 011005-011005. Copyright (2015) ASME. The whole content of this paper is included in Chapter 3.
- Khosrozadeh, A.; Darabi, M. A.; Xing, M.; Wang, Q., Flexible Electrode Design: Fabrication of Freestanding Polyaniline-Based Composite Films for High-Performance Supercapacitors. *ACS Applied Materials & Interfaces* 2016, 8 (18), 11379-11389. Copyright (2016) American Chemical Society. The whole content of this paper is included in Chapter 4.
- Khosrozadeh, A.; Darabi, M. A.; Wang, Q.; Xing, M., Polyaniline Nanoflowers Grown on Vibration-Isolator-Mimetic Polyurethane Nanofibers for Flexible Supercapacitors with Prolonged Cycle Life. *Journal of Materials Chemistry A* 2017, 5 (17), 7933-7943. Copyright (2017) The Royal Society of Chemistry. The whole content of this paper is included in Chapter 5.
- Winter, M.; Brodd, R. J., What Are Batteries, Fuel Cells, and Supercapacitors? *Chemical Reviews* 2004, 104 (10), 4245-4270. Copyright (2004) American Chemical Society. Figure 1.1 is adapted from this paper.

- Zhang, L. L.; Zhao, X. S., Carbon-Based Materials as Supercapacitor Electrodes. *Chemical Society Reviews* 2009, 38 (9), 2520-2531. Copyright (2009) The Royal Society of Chemistry. Figure 1.2 and Figure 1.3 are adapted from this paper.
- Gospodinova, N.; Terlemezyan, L., Conducting polymers prepared by oxidative polymerization: polyaniline. *Progress in Polymer Science* 1998, 23 (8), 1443-1484. Copyright (2004) Elsevier. Figure 1.5 is adapted from this paper.

Contents

List of Tables

List of Figures

List of Abbreviations

TCPs	acid-treated carbon particles
APS	ammonium peroxydisulfate
AFM	atomic force microscopy
CNF	carbon nanofiber
CNT	carbon nanotube
CV	cyclic voltammetry
DMF	dimethylformamide
EDL	electrical double-layer
EDLC	electrical double-layer capacitor
EIS	electrochemical impedance spectroscopy
EDS	energy-dispersive X-ray spectroscopy
ESR	equivalent series resistance
EG	ethylene glycol
ExG	exfoliated graphite
FTIR	Fourier transformed infrared
GCD	galvanostatic charge/discharge
GNS	graphene nanosheet
GO	graphene oxide
OHP	outer Helmholtz plane
IHP	inner Helmholtz plane

PExG	partial-exfoliated graphite
PVP	poly(vinylpyrrolidone)
PAni	polyaniline
PPy	polypyrrole
PU	polyurethane
PVA	polyvinyl alcohol
RGO	reduced graphene oxide
SEM	scanning electron microscope
AgNPs	silver nanoparticles
AgNWs	silver nanowires
SC	supercapacitor

Nomenclature

A	area of each electrode (cm^2)
C	capacitance (F) or specific capacitance (F/cm^2 or F/g)
E	energy density (Wh/kg or mWh/cm^2)
I	current (A)
m	mass of one electrode or total mass of two electrodes (g)
M	molar (1 mole of a compound is dissolved in a total volume of 1 L)
P	power density (W/kg or mW/cm2)
v	potential scan rate (mV/s)
V	potential in one sweep segment (V)
ΔV	potential window or the potential change after a full discharge (V)
V_{IR}	potential drop at the initial discharge stage (V)
$R_{\square}$	sheet resistance ($\Omega/\square$)
Δt	time for a full discharge (s)
A	ampere
F	farad
h	hour
L	litre
min	minutes
N	newton
P	pascal

S	siemens (electrical conductivity)
V	volt
W	watt
Ω	ohms

Chapter 1:

Introduction

1.1 Background

Clean energy technologies play an important role in overcoming fossil fuel exhaustion and global pollution for the sustainable development of energy worldwide [1]. Electrochemical energy storage and conversion devices, such as batteries, fuel cells and supercapacitors (SCs), are feasible, environmentally friendly, and sustainable clean energy technologies [1-2]. Developing relevant energy storage devices is crucial in utilizing sustainable and renewable energy resources. SCs, an important class of energy storage devices, have attracted intensive attention in recent years owing to their fast charge-discharge rate, high power density, low maintenance, and long cycle life [3-4]. SCs, also known as electrochemical capacitors, are most useful in applications that require a fast power boost and delivery. SCs support a broad spectrum of applications in areas including power electronics, memory protection, battery enhancement, portable energy sources, power quality improvement, adjustable speed drives, high power actuators, hybrid electric vehicles, renewable and off-peak energy storage, and military and aerospace applications [2]. For example, SCs are used in emergency doors of Airbus A380 [5] and in the drill that astronauts use to work on the International Space Station [6]. SCs are also utilized in hybrid electric cars as backup power sources and in hybrid

electric buses with stop-start engines [6]. All of the above examples justify the importance of research and development of high-performance SCs.

Eelectrostatic and electrolytic capacitors are considered the first and second generation capacitors. These early capacitors were utilized as primary circuit elements in holding small charges of direct current or to filter frequencies for alternating current circuits. With the rapid advances in the material science, the third generation known as SC was invented. SCs differ from conventional capacitors as they have smaller power densities, greater energy densities, and different material requirements [2]. The earliest SC with high capacitance was invented by Becker in 1957, electrodes of which were carbon material. The rapid developments in electronics and alternative-energy vehicles created a need for high power energy storage devices, which led to substantial advancement in SCs. In the early 1990s, the US Department of Energy strongly recommended funding for battery and SC research [2]. In a report by the US Department of Energy in 2007, the research need for SCs and batteries as the future energy storage devices was equally highlighted [5]. Therefore, great efforts have been dedicated to SC research and development of electrode materials, hybridizations, and electrolytes for performance improvement and costs reduction.

Figure 1.1 illustrates a simplified Ragone plot (power density versus energy density) for the various electrochemical energy conversion systems as well as conventional capacitors and internal combustion engines and turbines [3]. SCs bridge the gap between conventional capacitors and rechargeable batteries. SCs store much more energy density than conventional capacitors, while their power density is normally less than that of conventional capacitors. On the other hand, SCs generally have energy densities that are smaller than batteries, while they exhibit a greater power density. According to Figure 1.1, fuel cells are considered to be high-energy devices, and SCs are

usually regarded as high-power systems among electrochemical energy conversion devices. In terms of power and energy density, batteries are intermediate devices. With the fast pace of scientific advances in the electrochemical energy conversion devices, the boundaries and overlap in energy and power of SCs, fuel cells, and batteries are always increasing [3]. Batteries can keep electronic devices working for a long period of time owing to their high energy density, but it takes hours to recharge when they are discharged. Batteries are not suitable for applications that require high power due to undesirable chemical and physical changes to active materials during high-power operations [6]. Another shortcoming of batteries is their poor cycle life. SC are a good candidate for rapid power delivery and recharging owing to their high power density [7]. In addition to fast charge-discharge rate and high power density, SCs possess a long cycle life. However, the lower energy density of SCs compared to batteries is yet to be improved.

Batteries, fuel cells and SCs are all electrochemical energy conversion devices because their mechanism of operation is based on the fundamentals of electrochemical thermodynamics and kinetics. All three are useful for various applications depending on the requirements of energy and power, and thus none of them can serve all applications by itself [3]. Moreover, it is seen from Figure 1.1 that no single electrochemical energy conversion device can match the high energy and power merits of the internal combustion engine. High power and high energy to the level of combustion engines and turbines can best be achieved by combining the available electrochemical power systems [3].

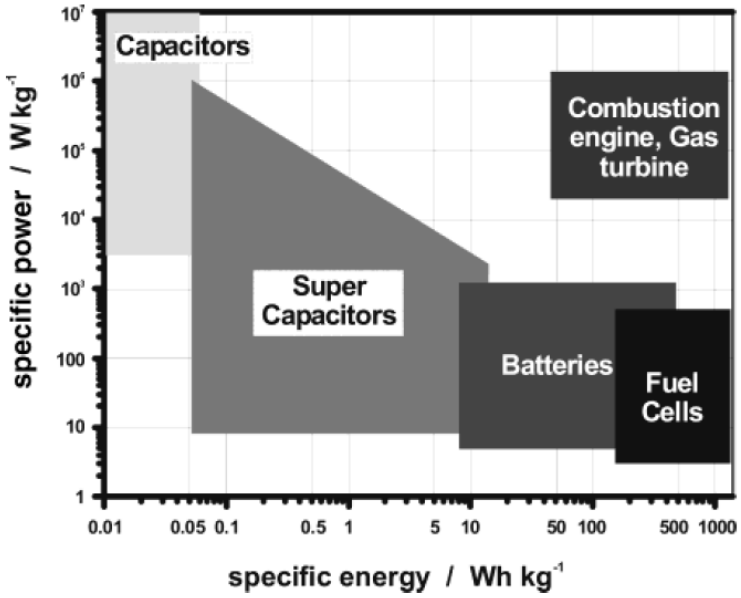

Figure 1.1. Simplified Ragone plot for various electrochemical energy conversion systems compared to conventional capacitors and internal combustion engines and turbines. Used with permission [3].

1.2 Components of SCs

A SC device is commonly composed of two electrodes separated by an ion permeable separator, an electrolyte ionically connecting both electrodes, and two current collectors directly attached to electrodes. Designing a SC requires the selection of proper electrode materials, electrolytes, separator, and sealants.

1.2.1 Electrodes and Current Collectors

Electrode materials are considered to play the substantial role in the performance of SCs and thus selecting and designing proper electrodes are the key. Electrode materials must be conductive and highly porous to increase charge transfer and charge storage ability [2]. Some other requirements for an electrode include having a high capacitance, high-temperature stability, long-term stability, and being environmental friendly and low cost. Generally, non-metal porous electrodes are utilized in SCs rather than the metal plates used in conventional capacitors. Electrodes of commercial SCs are

often constructed by coating a thin layer of active material on a conductive current collector [2]. Current collector plates are mostly required to enhance the conduction of electrons from electrodes to the outer circuit. Current collectors must be in good contact with the electrode surface, remain stable during charge and discharge, and possess a good conductivity to enhance electron transport [2]. In the Section 1.3, two charge storage mechanisms which take place in electrodes of a SC will be discussed.

1.2.2 Electrolytes

The capacitive performance of a SC is affected by the electrolyte in addition to electrode materials. There are several requirements for an ideal electrolyte: high ionic conductivity; large operating voltages; chemical and electrochemical stability; chemical inertness to current collectors, separator, electrode materials and packaging; wide operating temperature; safety and environmental friendly; and a low cost [2, 8]. There is no electrolyte that meet all of these factors, and thus an appropriate electrolyte is normally selected according to the type of electrode materials as well as the mentioned requirements. Depending on the type of SCs and other requirements, different categories of electrolytes can be used: aqueous, organic, ionic liquids, solid-state, and redox-active electrolytes [8].

H_2SO_4 is the most utilized electrolyte among aqueous electrolytes for SCs owing to its high ionic conductivity. It should be noted that 1 M H_2SO_4 aqueous solution is commonly used in SCs since its highest ionic conductivity at room temperature is reached with 1 M [8].

1.2.3 Separators and Sealants

Separators are electronically insulating to prevent short circuits between the two electrodes, while they are ion-conducting to allow the electrolyte ions to reach the electrode surface [2]. In addition,

separators should have good mechanical strength and durability as well as chemical and electrochemical stability in the electrolyte used in the device [2]. In SC design, separators are commonly made from microporous or non-woven thin films or membranes. The most common separator materials are glass fibres, cellulose derivatives, and polymer membranes (which includes polyolefins such as polypropylene, polyethylene, polytetrafluoroethylene, polyvinylidene fluoride, and polyvinyl chloride) [2, 8].

Application of a sealant depends on a SC cell type. Sealants must be electrically and ionically non-conductive and resistant to corrosion and degradation. Sealants are generally prepared form low-temperature-melting polyethylene material or viscous fast setting polymers such as epoxies. Sealants are useful for safety and preventing the water in the electrolyte to evaporate. A seal failure could lead to short circuits within assembled SC cells [2].

1.3 The energy storage mechanism

In general, the combination of electrode materials and electrolyte type define the performance of a SC. The energy storage mechanism of a SC is on the basis of two types of capacitive behavior that take place in electrodes: the electrical double-layer (EDL) capacitance from the pure electrostatic charge accumulation at the electrode interface, and the pseudocapacitance originated from fast and reversible redox reactions [2, 9-10]. EDL capacitance can happen on any solid-electrolyte interface. Carbonaceous materials, such as activated carbons, carbon nanotubes (CNTs), and graphene, are commonly used in EDL SCs owing to their high surface area, low cost, abundance, and relatively environmental friendly [2-3, 9-10]. Transition metal oxides and conducting polymers show pseudocapacitance properties as electrode materials [11]. Two mechanisms can function simultaneously depending on the nature of the electrode materials. Pseudocapacitors can provide

higher specific capacitance and energy density than EDL capacitors, although their power density and cycle life are generally inferior [12-13].

1.3.1 The energy storage mechanism of EDL

To fully grasp the charge storage mechanism of EDL materials, the characteristics of the EDL is described herein. Upon immersion of an electrode into an electrolyte solution, there is a spontaneous rearrangement of charges at the surface of the electrode as well as in the electrolyte facing the electrode. This EDL forms at the electrode-electrolyte interface with one layer inside the electrode surface and the other layer in the electrolyte as shown in Figure 1.2a (simple Helmholtz model). The two charged layers behave similar to a conventional capacitor with a distance of the order of molecular dimensions (denoted by "d" in Figure 1.2a). The properties of the EDL depend on the structure of electrode surface, the electrolyte composition, and the potential field between the charges at the interface [3]. Figure 1.2b shows the Stern model, a more complex model of the EDL [10]. The inner Helmholtz plane (IHP) passes through the centres of closest specifically adsorbed ions (generally anions) and/or adsorbed solvent molecules to the electrode surface. The outer Helmholtz plane (OHP) passes through the centres of closest non-specifically adsorbed ions (generally cations) in the electrolyte solution. Cations usually keep their solvation shells, while anions can lose their solvation shells. Hence, solvated cations are normally larger than the less solvated anions and thereby they populate the OHP [3]. This separation of charge in Helmholtz double layer at the electrode-electrolyte interface is the origin of the EDL capacitance. The EDL capacitance of carbonaceous materials is much greater than conventional capacitors owing to their high surface area of as well as nano-level thickness of the double layer. Figure 1.3 schematically illustrates an EDL capacitor made of porous carbon electrode.

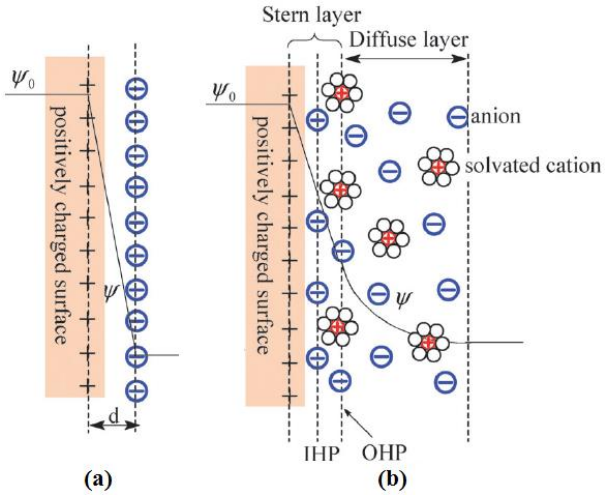

Figure 1.2. Models of the EDL at a positively charged surface: (a) the Helmholtz model, and (b) the Stern model, showing the inner Helmholtz plane (IHP) and outer Helmholtz plane (OHP). Used with permission [10].

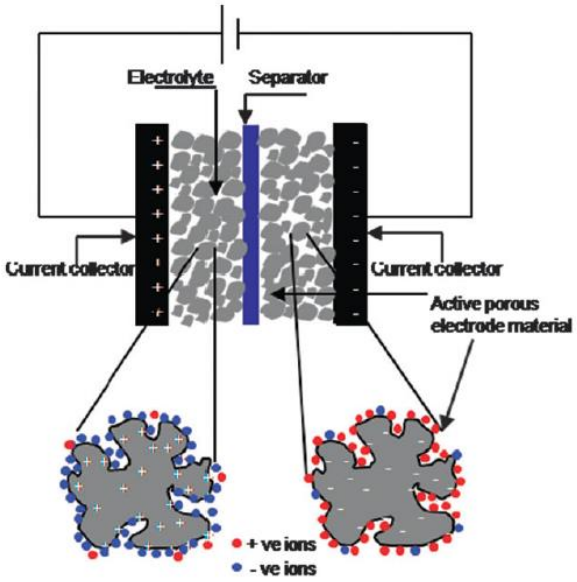

Figure 1.3. Schematic representation of an EDL capacitor based on porous electrode materials. Used with permission [10].

1.3.2 The energy storage mechanism of pseudocapacitance

The energy storage mechanism of pseudocapacitance is on the basis of fast and reversible redox reactions (faradic charge transfer) between the electrolyte and redox-active electrode rather than physical ion movements in the EDL capacitance (electric charge storage) [9-10, 14].

Only reversible or quasi-reversible redox materials are suitable to be used as a pseudocapacitor. The most commonly known active species are transition-metal oxides such as ruthenium oxide, manganese oxide, vanadium nitride, and iron oxide, as well as electrically conducting polymers such as polyaniline, polypyrrole, and polythiophene [10].

It should be noted that the EDL at the electrode-electrolyte interface forms and relaxes instantly with a time constant of ~10^{-8} s. Hence, the EDL material is able to respond quickly to potential changes because the process involves only a charge rearrangement, not a chemical reaction [3]. The instantaneous response of the EDL to potential changes is in contrast to the case of redox reactions. The time constant of redox reactions is generally is in the range of 10^{-2}-10^{-4} s depending on the reaction impedance and type of redox reaction (much slower than ~10^{-8} s for EDL) [3].

Generally, pseudocapacitance electrodes provide higher specific capacitance and energy density than EDL capacitors. Pseudocapacitors show inferior rate capability since there is a limited time for redox reactions to happen when a pseudocapacitor is charge-discharged with a high rate. This can be explained by the longer time constant of the redox reactions as opposed to the shorter time constant of the EDL process. In addition, pseudocapacitors suffer from limited cycling stability, whereas EDL capacitors show a long cycle life since no redox reaction is involved in the EDL process. In sum, while pseudocapacitance can be larger than EDL capacitance, it suffers from the drawbacks of poor cycling stability and rate capability. It should be noted that nanostructure and porosity of the electrode affect the rate capability in addition to the type of material.

1.4 Supercapacitor types

The type of a SC is usually determined by its structure and active materials. As described before, SCs store electrical energy with two different storage mechanism, i.e. EDL capacitance and pseudocapacitance. The contribution of the two mechanisms on the total capacitance of a SC depends on the type of active materials and structure of the SC. Hence, a SC can be categorized into three kinds depending on the electrode types [15]: EDL capacitors, pseudocapacitors, and hybrid capacitors. A general classification of SCs is shown in Figure 1.4. Hybrid SCs are based on both EDL capacitance and pseudocapacitance and are often asymmetric. In general, a SC can be constructed by symmetric electrodes (similar positive and negative electrodes) or asymmetric electrodes, and each individual electrode can be EDL, pseudocapacitance or combination of them. A composite electrode for SCs is a combination of two materials mostly a carbon-based material and a pseudocapacitive material (see section 1.7). In an asymmetric hybrid SC, the positive electrode is based on a pseudocapacitive material (or a composite electrode) and the negative electrode is an EDL material.

Another type of hybrid SC is called lithium-ion capacitors, in which one electrode is a rechargeable battery-type (negative electrode) and the other is an EDL or pseudocapacitive electrode.

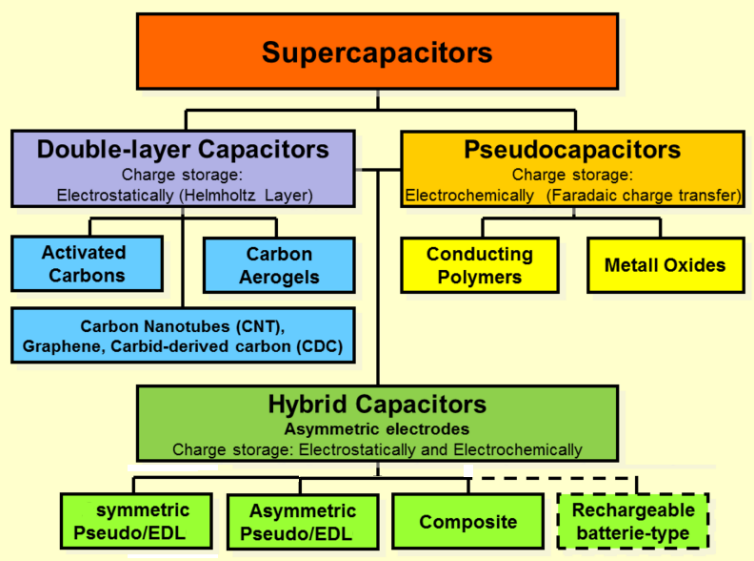

Figure 1.4. Classification of SCs [16].

1.5 Polyaniline

Polyaniline (PAni) is an electrically conducting and organic polymer. Among pseudocapacitance materials, PAni has been considered as one of the most promising electrode materials owing to its low cost, ease of synthesis, controllable electrical conductivity, high specific capacitance, environmental stability, and color change corresponding to diverse redox states [1].

PAni can be synthesized both chemically and electrochemically by polymerizing the inexpensive aniline monomer in acidic media (such as H_2SO_4, HCl, $HClO_4$, etc.) [17]. The electrochemical polymerization or electropolymerization of aniline involves the use of an electrical potential as a driving force [18]. The chemical synthesis of PAni is carried out using a powerful oxidizing agent such as ammonium persulfate. Different PAni nanostructures can be synthesized using both the chemical oxidative polymerization and the electropolymerization by adjusting the experimental conditions. For example, high-quality PAni nanofibers can be formed using two routes: rapidly mixed polymerization [19] and aqueous/organic interfacial polymerization [20-21].

Synthesis, properties and applications of PAni nanostructures have been extensively reported in review articles [22-24].

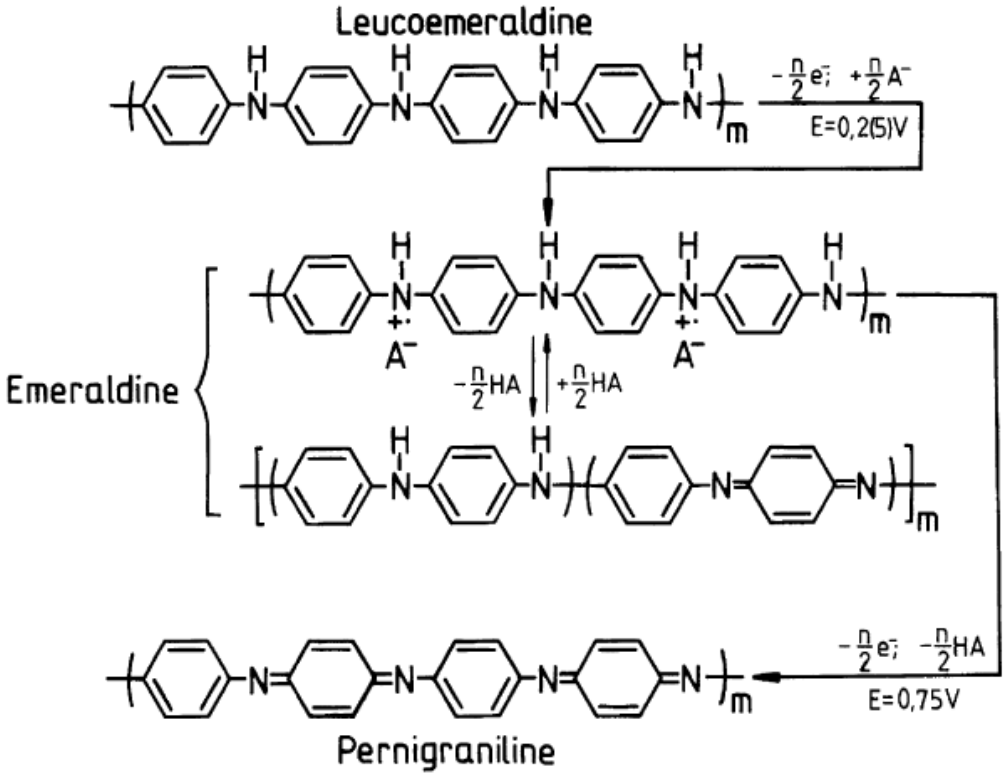

Figure 1.5. Three main oxidation states of PAni: leucoemeraldine, emeraldine and pernigraniline. Used with permission [22]

PAni exists in three main oxidation states: fully-reduced leucoemeraldine, the intermediate emeraldine and fully-oxidized pernigraniline (Figure 1.5) [22]. The chains of emeraldine form of PAni have alternating phenyl rings and nitrogen-containing groups. In this ordered structure, PAni chain forms in a zigzag in one plane and π-electron clouds extend over and below the plane (polyconjugation). The lone electron pair of the nitrogen also creates polyconjugation in a similar fashion as π-electrons. This polyconjugation is formed during PAni oxidation and creates charge carrier mobility, the source of conductivity in emeraldine [25]. During PAni oxidation, positive polaron is generated in the PAni chain and deforms the chain structure. The content of oxidized nitrogen atoms in the PAni chain can change from zero in the fully reduced form (leucoemeraldine,

all the nitrogen atoms are amine) to nearly one in the fully oxidized form (pernigraniline, all the nitrogen atoms are imine). In the emeraldine state of PAni (called emeraldine base), every second nitrogen atom is oxidized and PAni chains possess equal number of oxidized and reduced units [25]. Upon doping emeraldine base with an acid (i.e. the imine nitrogen protonated by an acid.), the resulting emeraldine salt form of PAni is highly electrically conducting (conductivity of 1-10 S/cm) [22, 25]. Emeraldine base is obtained by deprotonation of emeraldine salt upon neutralizing acid with a base, resulting in a decrease of conductivity by ten orders of magnitude. Emeraldine base is considered as the most useful form of PAni owing to its high stability at room temperature and high conductivity of protonated emeraldine [22]. The color of emeraldine base is blue and emeraldine salt is green. Leucoemeraldine form is electrically insulating (its conductivity is 10^{-8}-10^{-10} S/cm [25]) and is colorless. Pernigraniline form is also electrically insulating (conductivity of protonated pernigraniline is less than 10^{-2} S/cm [25]) and its color is blue/violet.

As an electrode material for SCs, PAni has several advantages such as high pseudocapacitance, low cost and ease of synthesis. However, there are few limitations of PAni that yet to be addressed in order to be able to compete with commercial EDL SCs. PAni suffers from poor cycling stability in aqueous electrolytes rooted in the repeated volumetric swelling and shrinking as a result of insertion/de-insertion of counterions during the charge-discharge cycles [26]. The repeated volume change of PAni causes structural instability and undesirable changes to the morphology of PAni, and thus the degradation of capacitive performance over cycling. The poor cycle life of PAni considerably compromises the advantage of the long cycle life of a SC over batteries [27]. PAni also exhibits a lower power density and rate capability than many EDL SCs [1]. In addition, it is formidable to produce mechanically robust films from pristine PAni since it is a brittle material with poor ductility [28]. To overcome the limitations of PAni, composite electrode materials are

expected to be developed by combining PAni with other nanostructures. Moreover, properly engineering PAni nanostructure could improve rate performance, cycle life and power density of PAni.

1.6 Graphene and Exfoliated Graphene

Graphene is a one-atom-thick, two-dimensional allotrope of carbon in which carbon atoms are bonded together in a hexagonal honeycomb lattice. Graphene is the basic structural element of graphite in which sheets of graphene are stacked on top of each other. Since the Nobel Prize in physics was awarded for graphene research in 2010, graphene has attracted tremendous attention as a promising material for electrochemical energy storage devices owing to its outstanding electronic conductivity, high surface area, excellent mechanical strength, low mass density, reasonable chemical stability, and superior thermal conductivity [4, 29-30].

Graphene can be synthesized in large quantities from inexpensive graphite by several techniques including reduction of graphene oxide (GO), liquid-phase exfoliation, and electrochemical exfoliation of graphite [30-31]. Other methods of graphene production includes micro-mechanical cleavage, chemical vapor deposition, and thermal decomposition of silicon carbide [30-31].

GO is produced in large scale by the oxidation of graphite in the presence of strong acids and oxidants using the modified Hummers method [32-37]. The common reduction of GO to graphene oxide (RGO) involves using chemical reducing agents such as hydrazine hydrate [38], hydroiodic acid [39], ascorbic acid [40], and sodium borohydride [41], etc. GO can also be reduced to RGO using other methods including thermal annealing, microwave and photo reduction, electrochemical reduction, and solvothermal reduction [31].

Owing to the high surface area and electrical conductivity of graphene, it can be used as an electrode material in double-layer SCs as long as its nanostructure is properly engineered.

1.7 PAni-Based Composite Electrodes

To overcome the limitations of PAni as an electrode material, composite electrode materials are usually developed by combining PAni with other nanostructures. For instance, improved energy storage can be achieved by designing composite materials from carbon nanostructures and PAni. In such a composite electrode, PAni provides a source of high pseudocapacitance, while carbonaceous materials ensure good cycling stability and high power density [1, 10, 28, 42-43]. There has been an extensive research on developing PAni-based composite electrodes with good cycling stability, high energy density, and high power density. Some examples of PAni-based composite electrodes for SCs are CNTs/PAni [44-49] and graphene/PAni [50-58], and carbon nanofibers/PAni [42, 59].

1.8 Design Factors for SCs

Designing a high-performance SC requires a proper engineering and selection of electrode materials, electrolyte, separator as well as suitable device assembly. Among SC elements, the electrode materials play a vital role in capacitive performance of a SC. The ideal factors for a SC to consider in a design of electrode materials are specific capacitance, power and energy density, cycling stability, rate capability, and manufacturing cost [28].

According to references [4, 60] and personal research experience in electrode design, ideal electrode materials are required to possess:

- intrinsically high specific capacitance (double layer and/or pseudocapacitance)
- a large specific surface area, which is directly related to the specific capacitance,

- a proper porosity and density, which affect the specific capacitance, rate capability, and power density,
- high electronic conductivity, which is crucial to the rate capability and the power density,
- chemical, mechanical and thermal stability, which is vital to the cycle life,
- inexpensive raw materials and manufacturing, and
- safe operation and nontoxic in case a leakage occurs.

A properly engineered nanostructure of electrode materials is crucial in securing many of the above properties. Designing the electrode nanostructure can be achieved using material and chemical characterizations along with electrochemical tests of assembled SCs. There is no solid rules or protocols to follow in designing a composite electrode materials. The above points and other basic theoretical concepts can assist selecting suitable trials in electrode composition and nanostructure. For example, bulk PAni (compacted polymer) is unsuitable as an electrode material because of its low accessible surface area and porosity. Very small pores prevent electrolyte ions to penetrate into active materials not in the immediate vicinity of the surface (low ion-transfer conductivity). The limited accessibility of electrolyte ions to active materials leads to inferior capacitance and rate capability as well as low power density (due to larger potential drop during charge-discharge). On the other hand, very large pores in an electrode morphology decrease the material continuity and thus limit its electronic conductivity. Another example is a graphene film [61] prepared by vacuum filtration of a RGO dispersion followed by drying, in which graphene sheets are stacked on top of each other. Although the stacked and layered structure of graphene film shows a very high electronic conductivity, it is unfit as an electrode material of a double-layer SC since

its low porosity prevent electrolyte ions from penetrating into the film (limited accessibility of graphene sheets).

1.9 Characterization and Electrochemical Measurements

1.9.1 Materials characterization

The surface morphology of samples is investigated using a scanning electron microscope (SEM) and atomic force microscopy (AFM). A nonconductive sample is usually coated with gold nanoparticles using a gold sputter before performing SEM. Fourier transformed infrared (FTIR) spectra are obtained using Thermo Nicolet iS10 FTIR Spectrometer. The electrical conductivity of films is measured by the standard four-probe method. For comparison between different samples an ohm meter is also used. Tensile tests are conducted using a material testing machine. To characterize nano-mechanical properties of membranes, quasi-static nanoindentation experiments are performed using a nano-mechanical testing machine.

1.9.2 Electrochemical measurements

Electrochemical experiments are carried out using an electrochemical workstation (potentiostat/galvanostat and with a frequency response analyzer). The electrochemical performances of assembled SCs are analyzed by means of three common electrochemical experiments: galvanostatic charge/discharge (GCD), cyclic voltammetry (CV), and electrochemical impedance spectroscopy (EIS).

GCD experiment is the most common technique to study the electrochemical performance of an assembled SC. GCD is performed by repetitive charging and discharging of a SC (or the working electrode in three-electrode systems) at a constant current. GCD curves are commonly shown as a

plot of the potential versus time [62]. Many required capacitive parameters (such as capacitance, resistance, energy and power density) can be calculated from GCD curves. The cycling stability of SCs is mostly evaluated using GCD tests.

The current used in GCD tests is commonly reported by researchers in A, A/g, A/cm^2, or A/cm^3. Generally, there is a lower and upper limit for the current that a SC can be charged or discharged, which is directly related to the rate capability of SCs. If one reports the current density but not mass loading or sizes of electrodes, the charge/discharge currents in A cannot be calculated making it difficult to compare or evaluate the results. In this thesis, therefore, lower and upper limits for the charge-discharge currents were defined and reported and/or area and mass loading of electrodes were given so that one can calculate the lower and upper limits for the charge-discharge currents. CV is a type of potentiodynamic electrochemical technique that can be used to study electrochemical reactions including electrochemical kinetics, reaction reversibility, reaction mechanisms, and effects of electrode structures on these parameters [2]. In CV tests, a potential is ramped linearly versus time between positive and negative electrodes for two-electrode configurations, or between reference and working electrodes for three-electrode systems. The current is recorded and plotted versus the applied potential to give CV curves. The speed of the potential change in mV/s is called the sweep rate or scan rate, and the range of potential change is called the potential window or operating potential. After reaching the potential window, the potential is ramped in the opposite direction to return to the initial potential. CV test may be repeated as many times as needed [62]. CV can be also utilized to determine capacitance of a SC cell and can provide information about redox and electrochemical reaction.

EIS measures the impedance of an electrochemical system as a function of frequency by applying a low-amplitude alternative potential (5 or 10 mV). The resulting data obtained by

EIS is expressed graphically in a Nyquist plot (imaginary and real parts of impedances in a complex plane) or a Bode plot [62]. The capacitive behavior of SCs can also be investigated using EIS tests presented in the form of Nyquist plots. In addition, EIS can be used to estimate the equivalent resistance and the charge-transfer resistance of a SC. EIS tests are commonly conducted over a frequency range from 10^5 to 0.01 Hz at an AC amplitude of 10 mV and zero DC amplitude.

In this thesis, all three electrochemical experiments (GCD, CV, and EIS) are used to assess performance of a SC. However, GCD curves are mostly used to estimate capacitive parameters including specific capacitance, energy density, power density and equivalent series resistance (ESR).

Two major experimental setups commonly used to evaluate electrochemical performances of fabricated electrodes are symmetric two-electrode and three-electrode configurations. A three-electrode system is consist of a working electrode, a reference electrode, and a counter electrode. They are usually used in electrochemical research and accurately determining capacitance of electrode materials (working electrode) [62-63]. Three-electrode configurations can overestimate the capacitance and underestimate the equivalent resistance of which an assembled SC can achieve [64]. SC prototypes or final products for the market are two-electrode systems. Hence, using two-electrode cells in design assessments is vital for estimating the capacitance, energy density, power density, and cycle life [64]. In this thesis, capacitive performances of fabricated electrodes are evaluate in a symmetric two-electrode system (assembled SC prototypes). Figure 1.6 shows the schematic arrangement of elements in an assembled SC (left), and the photograph of two electrodes placed on current collectors before assembly in a two-electrode system.

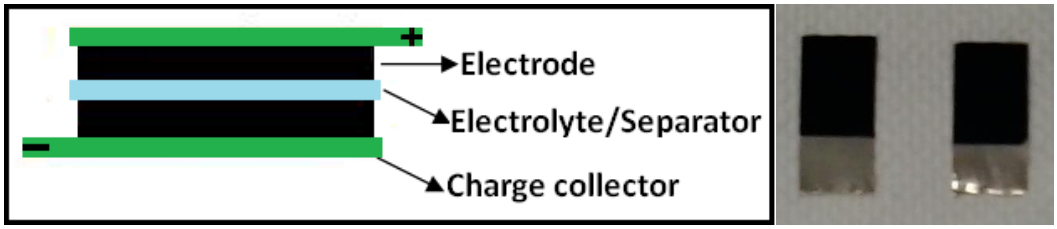

Figure 1.6. Schematic of an assembled SC (left), and the photograph of two electrodes placed on current collectors before the assembly (right).

The experimental setup in each chapter of the thesis is discussed in detail. In addition, the calculation procedure for obtaining capacitive parameters (the equivalent resistance, specific capacitance, energy density, power density, etc.) is provided in each chapter. 1 M sulfuric acid is used as an electrolyte in all experiments throughout this thesis.

1.10 Research Objectives

Despite the extensive research in the electrode design for SCs, the prospect of developing PAni-based electrode materials with superior capacitive performance is an important direction that has yet to be realized. Even though PAni has the advantage of having a high pseudocapacitance and being low cost, there are few shortcomings that limit the application of PAni as an electrode material for SCs. In addition to suffering from a poor cycle life, PAni exhibits a lower power density and rate capability than many electrical double-layer SCs. Moreover, preparing mechanically robust films from pristine PAni is difficult since it is a brittle material with poor ductility. To overcome the limitations of PAni, flexible PAni-based composite films are expected to be developed by combining PAni with other nanostructures. This could be achieved by utilizing several nanostructures in one composite to overcome the disadvantages of individual components and build a nanostructures structure with multiple benefits. Therefore, the objective of this thesis is exploring various approaches to develop PAni-based composite films as flexible electrodes of high-performance SCs. This goal is accomplished by utilizing advanced nanomaterials such as

PAni, graphene, carbon fibers, carbon nanotubes, cellulose, silver nanoparticles, silver nanowires, electrospun polyurethane and electrospun polyvinyl alcohol. To achieve the objective in this thesis, each chapter introduces an approach to tackle limitations of PAni and develop a PAni-based composite electrode.

1.11 Thesis Organization

This thesis is comprised of four published papers and a prepared manuscript, and it is organized in seven chapters as follows:

Chapter 1: Introduction

This chapter introduces the background of the SC research, justifies the importance of the present work, and summarizes the research objectives. The principle of operation of SCs and technical aspect of the current research is also covered.

Chapter 2: A Solid-State Supercapacitor Based on Polyaniline and Carbon Particles [1]

This chapter describes construction of a low-cost PAni-based electrode for solid-state SCs with high energy density and good cycling stability. The electrode of the SC is composed of a composite film of PAni and acid-treated carbon particles. Phytic acid is utilized as a crosslinker and co-dopant, and the gel electrolyte is used to address the poor cycle life of PAni and is composed of sulfuric acid and PVA.

Chapter 3: Flexible Cellulose-Based Films of Polyaniline-Graphene-Silver Nanowire for High-Performance Supercapacitors [65]

Chapter 3 reports a new strategy to construct a flexible PAni-based electrode for SCs with an adjustable mass-loading of active materials. The electrode is a flexible cellulose-based composite film of PAni, RGO and AgNWs.

Chapter 4: Flexible Electrode Design: Freestanding Polyaniline-Based Composite Films for High-Performance Supercapacitors [28]

This chapter presents a simple and low-cost approach to fabricate a high-performance SC on the basis of a flexible film of PAni, cellulose, ExG and AgNPs. This novel strategy allows designing PAni-based composite electrodes with a very high mass-loading of active materials, large surface area and porosity, and adjustable energy and power densities.

Chapter 5: Polyaniline Nanoflowers Grown on Vibration-Isolator-Mimetic Polyurethane Nanofibers for Flexible Supercapacitors with Prolonged Cycle Life [27]

This chapter introduces a new approach to construct a flexible electrode for SCs with an excellent cycling stability by coating flower-like PAni on CNT-reinforced PU nanofibers. This strategy addresses the poor cycle life of PAni and constructs a flexible PAni-based film by growing PAni on a cushiony support.

Chapter 6: Extraordinary Cycling Stability of Supercapacitors Based on Polyaniline Grown on Crosslinked Nanofibrous Films with Chemical Shape Memory

In chapter 6 a novel flexible electrode with an outstanding cycling stability is developed by growing PAni on ExG-coated cross-linked PVA nanofibers. In addition, a unique acid-base shape memory phenomenon is introduced for the PAni-coated PVA film.

Chapter 7: Conclusions and Future Work

This chapter summarizes the conclusions and contributions of the present research, and outlines the recommendations for the future work.

Chapter 2:

A Solid-State Supercapacitor Based on Polyaniline and Carbon Particles

2.1 Abstract

Polyaniline tends to degrade with cycling in aqueous electrolytes which can be alleviated using gel electrolytes. A low-cost solid-state supercapacitor of high energy density and good cycling stability is fabricated with a facile method. The electrodes of the supercapacitor are made of a freestanding composite film of polyaniline and acid-treated carbon particles using phytic acid as a crosslinker, and the gel electrolyte is composed of sulfuric acid and polyvinyl alcohol. The electrochemical performances of the as-fabricated supercapacitor are investigated with cyclic voltammetry, galvanostatic charge/discharge and electrochemical impedance spectroscopy. Our results show that a maximum capacitance of 272.6 F/g (3.63 F/cm^2) at a current density of 0.63 A/g can be achieved by the supercapacitor, which is significantly higher than most solid-state ones reported in the literature. The ability to achieve a high-capacitance supercapacitor with good cycling stability is mainly attributed to excellent infiltration of the gel electrolyte into the electrodes. The developed lightweight, thin, flexible, and environmental friendly supercapacitor would have potential applications in various energy storage devices, such as wearable electronics and hybrid electric vehicles.

2.2 Introduction

Electrode materials are usually considered to play the most important role in designing SCs. SCs store energy using either ion adsorption (electrical double-layer capacitors, EDLCs) or fast and reversible redox reactions (pseudocapacitors) [4]. The former uses carbonaceous materials with a large specific surface area, such as porous carbons, carbon fibers, CNTs, and graphene. The latter uses transition metal oxides or conducting polymers as electrode materials [11]. Two mechanisms can function simultaneously depending on the nature of the electrode materials. Pseudocapacitors can provide higher specific capacitance and energy density than EDLCs, although their power density and cycle life are generally slightly inferior [12-13]. Improved energy storage could be achieved by designing electrode materials to combine double layer capacitance together with fast and reversible pseudocapacitance. In such a composite electrode, pseudocapacitance materials provide the source of high specific capacitance and high energy density, while the carbon nanostructures ensure good rate capability, cycling stability and high power density at a large current [10].

Among pseudocapacitance materials, polyaniline (PAni) has been considered as one of the most promising electrode materials owing to its low cost, ease of synthesis, relatively good conductivity, good environmental stability, and color change corresponding to diverse redox states. However, PAni tends to be a brittle material with poor ductility. Although films of PAni nanofibers can be cast onto substrates, it is not possible to produce films, mechanically robust enough to be freestanding [66].

To achieve synergistic performances of composite electrodes, carbonaceous materials with their characteristics of high surface area, tunable surface functionalities, dimensional stability, and transport property can be combined with tunable redox state, and environmental stability of PAni

[42-43]. To date, extensive efforts and many approaches have been developed to prepare PAni-based composites. Long et al. [67], for the first time, synthesized a CNTs/PAni composite showing enhanced electrical properties. Zhou et al. [44] showed that a composite electrode made of CNTs/PAni exhibited much higher specific capacitance and better power characteristics than a pure PAni electrode in an aqueous electrolyte. Yan et al. [50] synthesized a graphene nanosheet (GNS)/PAni composite using *in situ* polymerization. They concluded that the enhanced specific capacitance of the composite was due to the synergistic effect between GNS and PAni. Later on, several research have been focused on developing composite electrodes based on CNTs/PAni [45-49] and graphene/PAni [51-54]. Jang et al. [42] successfully coated PAni on carbon nanofibers (CNFs) using one-step vapor deposition polymerization technique. They investigated the feasibility of PAni coated CNFs as electrode materials for SCs. A freestanding, flexible CNF/PAni composite paper was fabricated via *in situ* polymerization of aniline on an electrospun CNF paper as substrate [59]. The resulting composite paper displayed enhanced electrochemical capacitance in an aqueous electrolyte compared with a CNF paper. Nevertheless, a lot of research are still going on to produce composite electrodes having good cycling stability, high energy density, and high power density.

So far, majority of SCs have been fabricated using liquid electrolytes, which are usually hazardous to the environment. Therefore, sealing of the electrolyte and housing of the devices is inevitable, making them unsuitable for thin and lightweight applications [68]. In contrast, gel and solid polymer electrolytes combine the function of an electrolyte and a separator into a single component to reduce the number of parts and increase the potential window through the higher stability offered by a polymer matrix. Gel electrolytes offer a slightly lower conductance than liquid ones, but they provide more efficient mechanisms of ion transport and better cycle life [2]. In addition, electrodes containing PAni tend to degrade in aqueous acidic electrolytes resulting in a

poor cycling stability and a lower capacitive performance. This finding justifies the usage of gel electrolytes for PAni-based electrodes to achieve higher stability. Pan et al. [69] developed phytic acid-crosslinked PAni hydrogels with porous 3D nanostructures. Phytic acid molecules dope several PAni chains resulting in an interconnected nanostructure of PAni with improved mechanical stability. However, our experiments showed that such an interaction between phytic acid and PAni chain is still insufficient to prevent degradation of PAni in aqueous acidic electrolytes. Therefore, application of gel electrolytes could address the stability issue of phytic acid-crosslinked PAni. Hence, developing solid-state PAni-based SCs is highly desired for flexible, wearable and miniaturized electronics. Meng et al. [47] reported an ultrathin all-solid-state SC with composite electrodes produced by coating PAni on CNT films. Although the developed flexible SC showed a good cycling stability and specific capacitance as high as 175 F/g, designing a solid-state SC showing better performance in capacitance is yet to be realized. Even though electrodes show good electrochemical performances in aqueous electrolytes, there are different design factors that should be considered in fabricating a solid-state SC, such as providing a good penetration of gel electrolyte into electrodes, optimizing an amount of gel electrolyte provided to electrodes, adjusting the thickness of electrodes, selecting suitable and flexible current collectors, and a proper assembly.

Here a fabrication of a low-cost high-capacitance solid-state SC based on a composite film of acid-treated carbon particles (TCPs)/PAni with a well-impregnated sulfuric acid/polyvinyl alcohol (PVA) gel as the electrolyte is reported. The fabrication process is quite simple and the materials are low-cost and environmental friendly. In addition, the degradation problem of PAni or its poor cycling stability is addressed herein. In a typical synthesis process, a composite consist of nano-sized TCPs and PAni nanofibers is prepared by an *in situ* polymerization of aniline in the presence

of hydrochloric acid and phytic acid. Then a freestanding thin film of TCPs/PAni is formed by vacuum-filtering of the as-prepared mixture (Figure 2.1a). In addition to doping of PAni, phytic acid acts as a crosslinker of PAni nanofibers [69], which facilitates fabrication of a freestanding composite film. Finally, two TCPs/PAni electrodes are assembled into a solid-state SC by using sulfuric acid/PVA gel electrolyte and stainless-steel current collectors as shown in Figure 2.1b. The electrochemical performances of the solid-state SC are analyzed by means of cyclic voltammetry (CV), galvanostatic charge/discharge (GCD) and electrochemical impedance spectroscopy (EIS). In addition, effects of different parameters on the design and performance of the device are studied in detail.

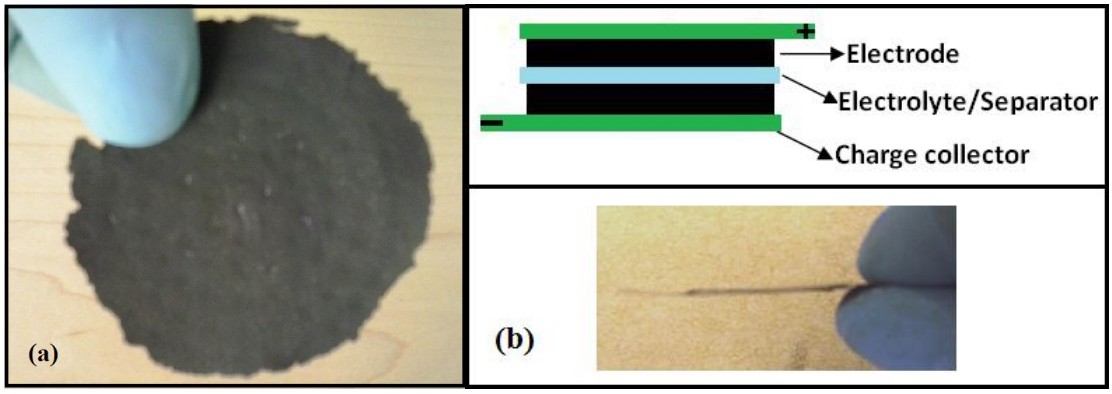

Figure 2.1. (a) Photograph of the freestanding TCPs/PAni film, (b) Side-view photograph of the fabricated SC (bottom) and its schematic diagram (top).

2.3 Experimental Methods

2.3.1 Preparation of TCPs/PAni

TCPs are produced using a similar method as preparation of quantum dots reported in [70], but with a less extreme procedure. Bundles of carbon microfibers are sliced and then ground with a mortar and pestle to obtain fine macro-sized ground carbon fibers. 0.4 g ground carbon fibers are added into a mixture of concentrated H_2SO_4 (30 mL) and HNO_3 (10 mL). The mixture is sonicated for an

hour and stirred for 5 hours at 80 °C. After diluting the cooled solution with deionized water, the pH is increased with NaOH. The resulting mixture is centrifuged to remove large particles and then dialysed in a dialysis bag (retained molecular weight: 1000 Da.) for 4 days to obtain nano-sized TCPs.

To produce TCPs/PAni composite, 0.15 g of TCPs is added to a solution containing 0.3 mL aniline and 5 mL of 1 M HCl. The mixture is then sonicated for an hour and stirred for a day to allow the adsorption of aniline monomers on the surfaces of TCPs. Afterward, another solution containing 0.16 g ammonium peroxydisulfate (APS), 5 mL of 1 M HCl, and 0.6 mL of phytic acid is added to the former mixture allowing the reaction to continue for 6 h at 4 °C. Phytic acid plays roles of a dopant and a crosslinker which increases the consistency of the final composite film [69]. Each phytic acid molecule is able to dope several PAni chains leading to an interconnected nanostructure of PAni [69]. Since phytic acid is a weak acid, 1 M HCl is also utilized as a co-dopant of PAni to offer a high conductivity to PAni. The as-prepared TCPs/PAni mixture is vacuum-filtered using Whatman filter paper (grade 1 with pore size of 11 μm) to remove excessive liquids, reactants and small particles. Finally, the thin film of TCPs/PAni is peeled off from the filter paper after moderately drying in the room temperature. The dried freestanding film of TCPs/PAni (Figure 2.1a) has an approximate thickness of 0.25 mm.

2.3.2 Fabrication of SCs

To make H_2SO_4/PVA solution, 0.5 g of H_2SO_4 is added into 5 mL of deionized water, and then 0.5 g of PVA powder is added. The whole mixture is heated to 90 °C under stirring until the solution becomes clear. The as-prepared TCPs/PAni film is then cut into two rectangular strips (1.5cm×2cm) as electrodes of the SC. Each electrode has an approximate dried weight of 40 mg

(13.33 mg/cm^2). Two electrodes are further attached to stainless-steel sheets as current collectors with silver epoxy. In order to assemble the solid-state device, the surfaces of two electrodes are wetted with H_2SO_4/PVA solution four times with a delay of approximately three hours between each wetting to allow the polymer electrolyte to efficiently penetrate into pores of TCPs/PAni electrodes. The mass-loading of the gel electrolyte on each electrode is approximately 90 mg. After the last coating, they are kept untouched at room temperature for 12 h to allow the evaporation of excess water. Then, the two electrodes are gently pressed together and air-dried at the room temperature for a day to form the solid-state SC (Figure 2.1b). Note that H_2SO_4/PVA gel acts as a separator in addition to an electrolyte.

2.3.3 Characterization

The surface morphology of TCPs/PAni film is observed under a scanning electron microscope (SEM) (JEOL, JSM-5900LV) at an accelerating voltage of 10 kV. The AFM topographies of TCPs/PAni composite and TCPs are carried out using Nanosurf easyScan 2 (NANOSURF AG). The electrical conductivity of the film is measured by the standard four-probe method. All electrochemical experiments are carried out using a potentiostat/galvanostat (Solartron 1287a) paired with a frequency response analyzer (Solartron 1260a). The electrochemical impedance spectroscopy (EIS) measurements are performed over a frequency range from 10^5 to 0.01 Hz at an AC amplitude of 10 mV. Galvanostatic charge/discharge (GCD) measurements are run from 0 to 0.7 V at constant currents ranging from 2 to 100 mA. Cyclic voltammetry (CV) tests are recorded from 0 to 0.8 V at different scan rates ranging from 1.5 to 100 mV/s. The capacitance derived from CV curves is calculated according to the following equation: $C = 2(\int IdV)/v\Delta V$, where I is the voltammetric current, v is the potential scan rate, V is the potential in one sweep segment, and ΔV

is the potential window. Mass-specific capacitance and areal-specific capacitance are determined by dividing *C* by *m* and *A*, respectively, where *m* is the mass of one electrode, and *A* is the area of one electrode. The capacitance derived from GCD curves is estimated from the discharging slope after the IR drop, V_{IR} (the potential drops at the initial discharge stage, which is mainly attributed to the intrinsic resistance of the electrode material and the resistance of the gel electrolyte), based on $C = 2I\Delta t/(\Delta V - V_{IR})$, where *I* is the discharge current, Δt is the time for a full discharge, and ΔV represents the potential change after a full discharge. The equivalent series resistance (ESR) is obtained using $ESR = V_{IR}/2I$. The energy density (*E*) and power density (*P*) are calculated by using the equations $E = C(\Delta V - V_{IR})^2/2m$ and $P = E/\Delta t$, respectively. All electrochemical parameters are calculated for one electrode.

2.4 Results and Discussion

Figure 2.1a shows the photograph of the freestanding TCPs/PAni film. The flexibility of the whole device depends on the current collectors, thin stainless-steel sheets, which have enough flexibility for wearable electronic applications. Using the four-probe method, $R_{\square}$ and the conductivity of the film are determined to be 48.5 Ω/□ and 0.82 S/cm, respectively. The electrical conductivity of pure PAni is approximately 0.6 S/cm [59], showing improved conductivity of our TCPs/PAni composite film.

SEM image of TCPs/PAni film is shown in Figure 2.2 demonstrating well-grown PAni on a particle of carbon fiber. AFM topography of TCPs/PAni composite in areas of 7.68μm×7.68μm and 3.84μm×3.84μm are provided in Figure 2.3a and b, respectively. AFM and SEM images confirm the highly porous structure of TCPs/PAni composite, which facilitates effective penetration of polymer electrolyte into the composite electrode materials. Furthermore, high

surface area of TCPs/PAni structures can be observed, which provides effective ion adsorption and desorption enhancing redox reactions. AFM topography of TCPs in Figure 2.3c and d indicates nano-sized carbon particles offering high overall surface area when coated with PAni nanofibers. It should be noted that the process of acid treatment largely enhance PAni grafting by carbon fiber particles owing to partial oxidation of the surface of carbon. In addition, a freestanding thin film cannot be produced without using TCPs since PAni fibers themselves show little mechanical integrity in a film form [66]. In fact, both TCPs and phytic acid (acts as a dopant and crosslinking agent) contribute to obtaining a freestanding composite film that can be used in constructing a flexible solid-state SC.

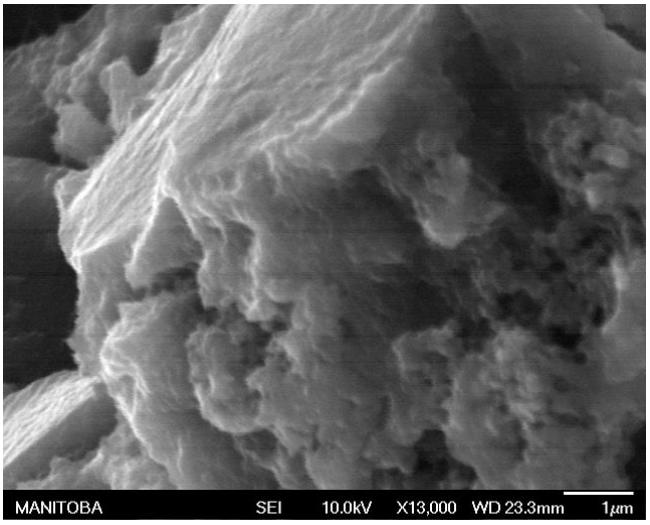

Figure 2.2. SEM image of TCPs/PAni film.

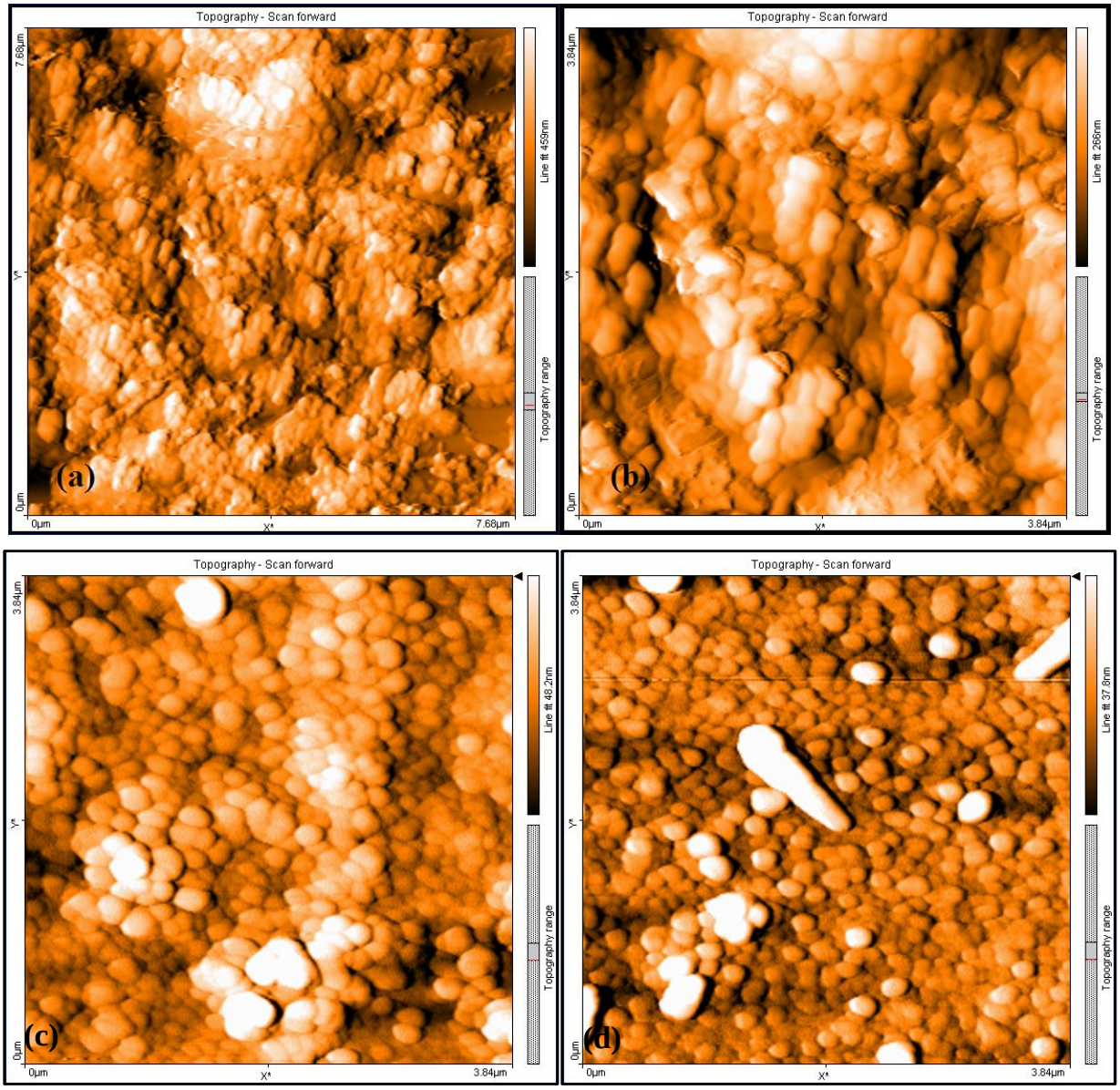

Figure 2.3. (a) and (b) AFM topography of TCPs/PAni composite, (c) and (d) AFM topography of TCPs (diameter: 100-200 nm and thickness: 10-20 nm).

The capacitive performance of the SC is evaluated by CV and GCD tests. CV curves of the device are plotted in Fig. 4a in the range 0 to 0.8 V and with scan rates recorded from 0.0015 to 0.1 V/s. An oblique angle of the loops in the CV curves is mainly due to its ESR. The capacitance is usually calculated from GCD curves. However for the sake of comparison, the mass- and areal-specific capacitance at different scan rates based on CV curves is estimated and presented in Figure 2.4b. It is observed that the capacitance is highly decreased with an increase in the scan rate due to

the limited mass transfer and limited time for ion movements to make redox reactions happen at higher scan rates. To demonstrate the applicability of the fabricated SC in a wider potential window, CV curves at three different potential windows are displayed in the inset of Figure 2.4b. However, it is more efficient to operate a SC in a smaller potential window since it is more prone to get hot in larger potential windows. In addition, rate of self-discharge is higher in larger potential windows leading to lower power density.

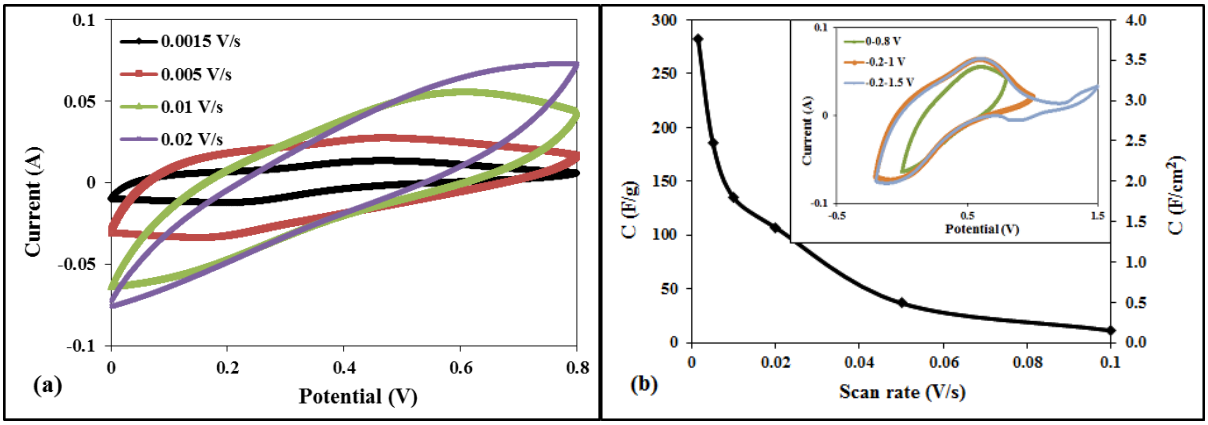

Figure 2.4. (a) CV curves at different scan rates, (b) corresponding mass- and areal-specific capacitance of one electrode at different scan rates and CV curves at three different potential windows (Inset).

GCD curves for different current densities are shown in Figure 2.5a. According to GCD tests, the calculated specific capacitance and ESR versus current density are illustrated in Figure 2.5b and c, respectively. The corresponding Ragone plots (power density versus energy density), at different current densities, are also depicted in Figure 2.5d. It can be seen that the specific capacitance, ESR, power density and energy density are all dependent on the current density. According to Figure 2.5b, the specific capacitance increases from 100.74 F/g (1.34 F/cm^2) to 272.62 F/g (3.63 F/cm^2) with an increase in the current density from 0.05 to 0.63 A/g, which could be attributed to higher rates of self-discharge at lower current densities. However, it reduces to 198.37 F/g (2.64 F/cm^2) when the current density is further increased to 2.50 A/g, due to larger IR drops at higher current densities. It is observed from Figure 2.5c that ESR increases with a decrease

in the current density, in contrast to conventional capacitors that the resistance remains constant. At a lower current, ions penetrate deeper into the electrode resulting in a higher charge transfer resistance. Additionally, a lower current facilitates more ion penetration and more redox reactions in PAni chains resulting in an increase in resistance due to the transition between a conducting state (emeraldine) and a semiconducting state (pernigraniline). Figure 2.5d indicates that the SC exhibits a lower power density when the current density is decreased, which is due to an increase in ESR. In other words, power density is inversely proportional to ESR of the device.

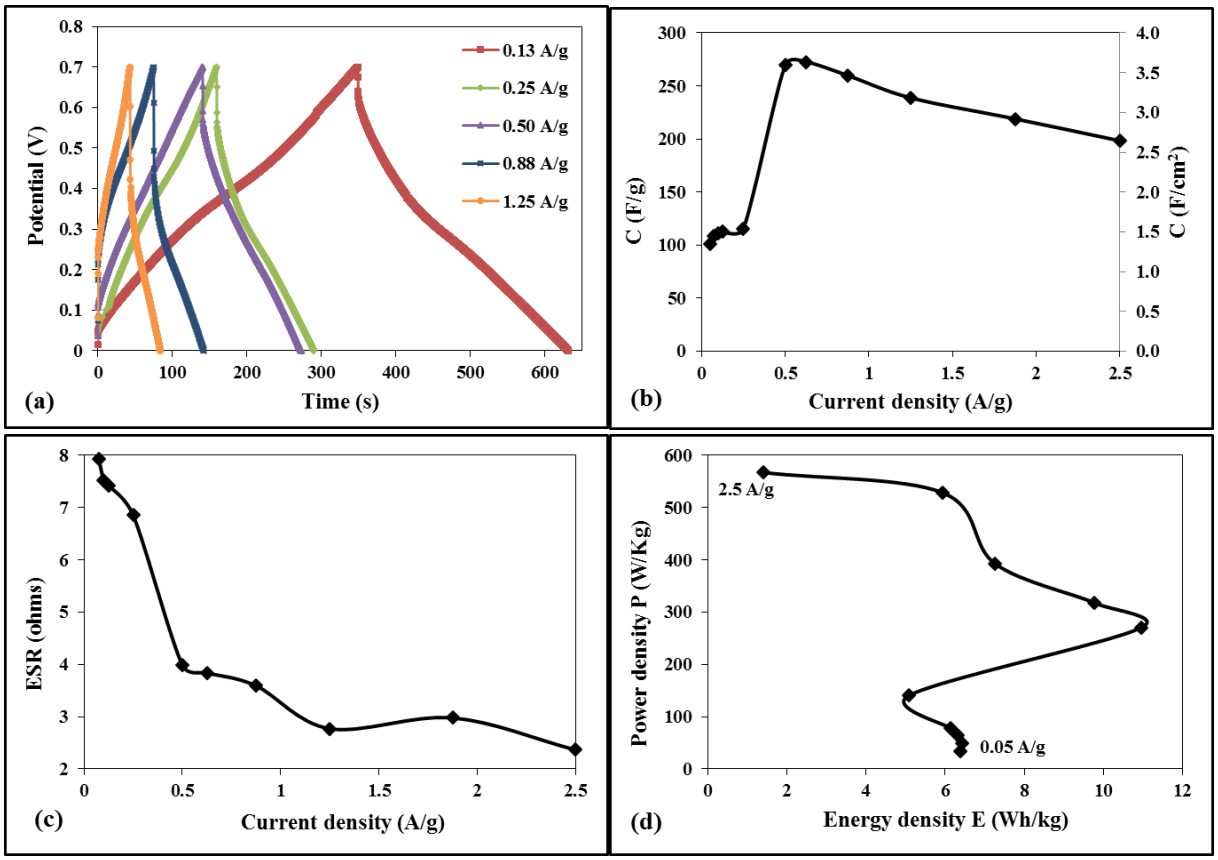

Figure 2.5. (a) GCD curves at different current densities, (b) mass- and areal-specific capacitance versus current densities, (c) ESR versus current densities, (d) Ragone plot. All values are calculated for one electrode.

Figure 2.6 shows good cycling stability of the fabricated SC with 95.7% capacitance retention after 501 cycles of GCD at a current density of 1.25 A/g. This could be due to the usage of gel electrolytes in contrast to aqueous electrolytes that cause a degradation of PAni. To show the

practical feasibility of the work, the picture of two fabricated SCs in series lighting a red light-emitting-diode is provided in the inset of Figure 2.6.

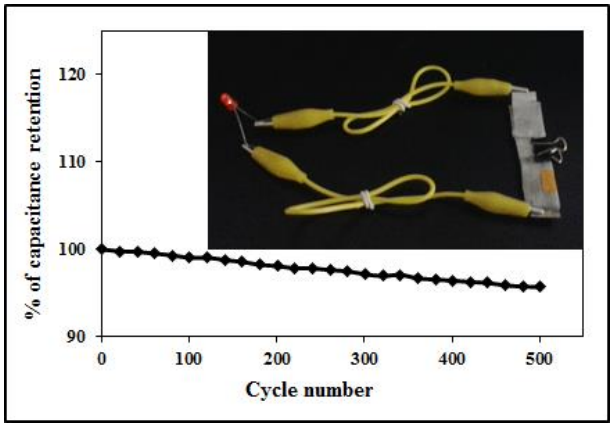

Figure 2.6. Cycling performance of the SC a current density of 1.25 A/g and a digital picture of two SCs in series lighting a red light-emitting-diode (Inset).

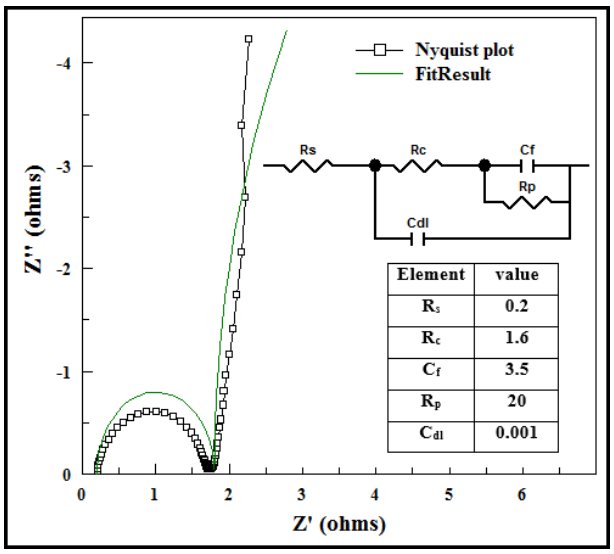

Figure 2.7. Nyquist plot, corresponding fitted results of the equivalent circuit and its proposed equivalent circuit (Inset).

Nyquist plot and its equivalent circuit, obtained from EIS, is depicted in Figure 2.7. The proposed equivalent circuit of the SC and its corresponding fitted parameters are provided in the inset of Figure 2.7, where R_s is the series resistance due to connection resistance, R_c is the charge transfer resistance of the electrochemical reaction producing pseudocapacitance, C_f is the pseudocapacitance, R_p is the parallel resistance of the leakage reaction, and C_{dl} is the double-layer

capacitance. It can be seen from the equivalent circuit that the double-layer capacitance is much smaller than the pseudocapacitance of PAni, as expected.

Parameters of some flexible solid-state SCs in the literature are listed in Table 1. According to Table 1, the estimated mass- and areal-specific capacitances of TCPs/PAni based solid-state SC are substantially higher than those of previously reported solid-state devices. For instance, the highest specific capacitance of our SC, estimated from the GCD at a current density of 0.63 A/g is 272.6 F/g (3.63 F/cm^2), which is higher than the highest specific capacitance (175 F/g, 425.25 mF/cm^2) reported for a solid-state SC made of CNT/PAni composite films [47]. The ability to achieve a high mass-specific capacitance and an ultra-high areal-specific capacitance in our SC could be attributed to the large specific surface area of the electrode, large mass-loading of active materials, high pseudocapacitance of PAni and the excellent infiltration of the gel electrolyte into the electrode network. In addition, the combination of TCPs with phytic acid-crosslinked PAni with porous 3D nanostructure lead to the construction of a film with a large mass-loading of active materials (13.33 mg/cm^2).

Table 2.1. Comparison of parameters of previous flexible solid-state SCs.

Reference	**Electrode material**	**Highest mass-specific capacitance (F/g)**	**Highest areal-specific capacitance (mF/cm^2)**	**Thickness (µm)**	**density (g/cm^3)**
This work	TCPs/PAni	272.6	3630	250	0.53
[47]	CNTs/PAni	175	425.25	22-37	0.81
[71]	Graphene	186	372	120	0.17
[72]	Graphene	203.8	7.34	7.6	0.05
[73]	CNTs	110	3.67	0.6	0.55
[74]	Polypyrrole/paper	118.6	420	147	0.24

2.5 Conclusion

In summary, a low-cost solid-state SC has been developed using a composite film of TCPs/PAni as the electrode and H_2SO_4/PVA gel as the electrolyte. The entire device has a suitable thickness, flexibility, cycling stability and shows an outstanding capacitive behaviour. The combination of TCPs and phytic acid-crosslinked PAni, effective infiltration of the gel electrolyte into the electrodes, and large mass-loading of active materials also contribute to the high capacitance of the as-prepared SC. Furthermore, it is a lightweight and environmental-friendly device with a high energy density and a potential application in wearable electronics. It is also concluded that electrochemical performances of PAni-based SCs depend on methods of charging and discharging, such as current and scan rate.

In this work, a free-standing composite film of TCPs and phytic acid-crosslinked PAni with a porous nanostructure is developed. The composite film possesses a large mass-loading of active materials leading to an ultra-high areal-specific capacitance. In addition, gel electrolyte was employed to address the poor cycle life of PAni and construct a low-cost solid-state SC. There is, however, a major limitation to a solid-state PAni-based SC: it suffers from lower rate capability compared to aqueous electrolyte SCs. In the next chapter, another approach will be introduced to construct a free-standing PAni-based film as the electrode without using gel electrolyte.

Chapter 3:

Flexible Cellulose-Based Films of Polyaniline-Graphene-Silver Nanowire for High-Performance Supercapacitors

3.1 Abstract

A facile fabrication of a high-performance supercapacitor (SC) using a flexible cellulose-based composite film of polyaniline (PAni), reduced graphene oxide (RGO), and silver nanowires (AgNWs) is reported. The flexibility, high capacitive behaviour, cycling stability and enhanced rate capability of the entire device make it a good candidate for flexible and wearable SCs. Our results demonstrate that a capacitance as high as 73.4 F/g (1.6 F/cm^2) at a discharge rate of 1.1 A/g is achieved. In addition, the SC shows a power density up to 468.8 W/kg and an energy density up to 5.1 Wh/kg. The flexibility of the composite film is owing to the binding effect of cellulose fibers as well as AgNWs. The superb electrochemical performance of the device is found to be mainly attributed to the combination of PAni/RGO/AgNWs ternary in a cushiony cellulose scaffold and porous structure of the composite.

3.2 Introduction

SCs are generally composed of two electrodes, an electrolyte, a separator, and current collectors. Electrode materials play a vital role in the performance of SCs. By improving the design of electrode materials, we can achieve low-cost SCs with high energy density,

high power density, good rate capability, and cycling stability. Polyaniline (PAni) is a widely-used pseudocapacitance material for electrodes of SCs owing to its low cost, ease of synthesis, good conductivity, and good environmental stability. However, PAni tends to degrade with cycling due to its structural instability resulted from repeated volumetric swelling and shrinking during the charge-discharge process [13].

The properties of PAni can be greatly enhanced by forming composites between the PAni and other materials such as carbon nanostructures. In such composite electrodes, PAni is expected to provide a source of high capacitance, and the carbonaceous materials improve rate capability, cycling stability and conductivity [10, 13, 42-43]. Graphene has been extensively used in developing graphene/PAni composite electrode materials [50-57]. For instance, a graphene/PAni composite was synthesized using the in-situ polymerization of PAni on graphene nanosheets [50]. It was concluded that graphene sheets could provide active sites for the growth of PAni as well as an excellent electron transfer path, resulting in an enhanced electrochemical performance.

To enhance the electrical conductivity and mechanical flexibility of graphene-containing composite films, silver nanowires (AgNWs) were often incorporated into composites [75-76]. Therefore, AgNW is a good candidate to improve the electrical conductivity and mechanical flexibility of PAni/graphene composite films. AgNWs can be readily synthesized using a simple solvothermal method [77].

It is still a challenge to effectively fabricate freestanding and flexible composite films of PAni-based composites due to the brittle nature of PAni. Cellulose, a low-cost and environmentally-friendly organic polymer, is a good candidate to help the formation of a flexible PAni-based composite film, while maintaining necessary features of the composite.

The inexpensive, renewable, biodegradable, biocompatible, and highly flexible material has been widely used for its physical properties and chemical reactivity [78-79]. Solid-state flexible SCs were fabricated from an in-situ polymerization of PAni on a cellulose aerogel coated with silver nanoparticles [80]. CNT/cellulose/PAni composite films were prepared via an in-situ polymerization of PAni on CNT/cellulose flexible films for high-capacitance SCs with good cycle stability [81].

Despite the extensive progress in designing PAni-based composite films for SCs, it is indispensable to design composite electrodes that combine all the features, specifically being flexible, and low cost while showing good cycling stability, rate capability, and acceptable energy and power density. To this end fabrication of a low-cost high-performance SC based on a flexible composite film of PAni/graphene/cellulose/AgNWs is reported for the first time. PAni acts as a pseudocapacitance material, the main element of the composite electrode; graphene is vital to enhance capacitance and ensure good rate capability and cycling stability of the SC; cellulose acts as a scaffold and binder of materials ensuring the consistency and flexibility of the composite film; and finally AgNWs play the role of framework to enhance the conductivity and mechanical flexibility of the composite electrode. In a typical preparation, first PAni/graphene oxide (GO) nano-composite is prepared by an in-situ polymerization of aniline in the presence of GO, followed by reduction of GO in the composite to reduced graphene oxide (RGO). Afterwards, the as-prepared PAni/RGO composite is added to cellulose fibers/AgNWs suspension. A freestanding thin film is then formed by vacuum-filtering of the as-prepared mixture followed by a controlled shrinkage by a drying treatment.

3.3 Experimental Methods

3.3.1 Preparation of Cellulose

Cellulose fibers are prepared from a piece of tissue wiper (Light-duty, virgin-fiber tissue wipers; VWR, USA) pulped in a water-containing beaker by means of a mechanical homogenizator (9000 rpm for 15 min). To wash and remove aggregated fibers and unpulped cellulose from cellulose fibers, the mixture is then centrifuged at a speed of 4000 rpm followed by pouring out the excess water. The cellulose cake at the bottom of the tube has two phases recognizable by the eye. The cellulose fibers are then collected from the upper phase with a spatula leaving a portion of the lower phase behind to be on the safe side. The centrifugation process is repeated two more times to make sure all aggregations are separated.

3.3.2 Preparation of AgNWs

AgNWs with a diameter of about 170 nm are synthesized by the reduction of silver nitrate ($AgNO_3$, ≥99.0%) in ethylene glycol (EG) in the presence of poly(vinylpyrrolidone) (PVP) and iron chloride ($FeCl_3$), according to a solvothermal method reported previously [75, 77]. Briefly, a 20 mL EG solution of 0.2 mM $FeCl_3$ is stirred after the addition of 0.7 g PVP. The mixed solution is added drop by drop into 20 mL of a magnetically stirred EG solution of $AgNO_3$ (0.1 M). Then, the solution is poured into a Teflon-lined autoclave tube and is sealed and heated at 160 °C for 2.5 h. AgNWs are collected by the repetitive addition of acetone and centrifugation.

3.3.3 Preparation of PAni/RGO/Cellulose/AgNWs Composite Film

In a typical preparation of the composite, 50 mg GO (The Sixth Element Inc.) is added into 50 mL deionized water and sonicated in a bath-sonicator (VWR International, LLC.) for 20 min. After an addition of 0.28 mL aniline, the mixture is sonicated in the bath-sonicator for another 20 min. To carry out the polymerization of aniline, another solution containing 0.35 g ammonium persulfate (APS) in 10 mL of 1 M H_2SO_4 is added to the mixture to allow a reaction to finish under a mild stirring at the ambient temperature for 4 hours. The molar ratio of aniline/APS is 2. The as-prepared PAni/GO composite is then washed with water by centrifugation for several times. By dispersing the composite in 50 mL of 0.05 M aqueous sodium borohydride solution at 90 ºC for 2 hours, GO is reduced to RGO and PAni is simultaneously dedoped. Afterwards, a 50 mL dispersion of 22 mg cellulose fibers and 20 mg AgNWs in deionized water is poured into the PAni/RGO mixture. The as-prepared composite mixture is vacuum-filtered through a Whatman filter paper (grade 5) followed by an addition of deionized water to remove excess reactants. The flexible thin film of PAni/RGO/cellulose/AgNWs is peeled off from the filter paper after a moderate drying. Finally, the freestanding composite film is soaked in 1 M H_2SO_4 to redope PAni. The mass-loading of active materials in each electrode is approximately 10.67 mg/cm^2.

3.3.4 Characterization

The surface morphology of films is observed under a scanning electron microscope (SEM, JEOL, JSM-5900LV). To carry out electrochemical experiments, SCs are assembled in a symmetric two-electrode system as follows. Two rectangular strips of as-prepared films (1.5 cm×2 cm) as electrodes are soaked in 1 M H_2SO_4; and they are separated by a filtrate

paper wetted with 1 M H_2SO_4. Two stainless-steel foils are used as the current collectors and all of the components are assembled into a layered structure sealed with a parafilm to avoid the evaporation of water.

All electrochemical experiments are carried out using CS350 electrochemical workstation (CorrTest Instruments Co.). EIS measurements are performed over a frequency range from 10^5 to 0.01 Hz at an AC amplitude of 10 mV. GCD tests are run from 0 to 0.8 V at constant currents ranging from 10 to 300 mA. Mass-specific capacitance of an entire SC derived from GCD curves is estimated from the discharging slope after the IR drop, V_{IR} (the potential drops at the initial discharge stage), based on $C = 0.5I\Delta t / m(\Delta V - V_{IR})$, where I is the discharge current, Δt is the time for a full discharge, m is the mass of one electrode, and ΔV represents the potential change after a full discharge. The equivalent series resistance (ESR) is estimated by $ESR = V_{IR}/2I$. The energy density (E) and power density (P) for an entire device are calculated according to the following equations: $E = 0.5C(\Delta V - V_{IR})^2 = I(\Delta V - V_{IR})\Delta t / 4m$ and $P = E/\Delta t$, respectively.

3.4 Results and Discussions

The resulting disintegrated cellulose contains microfibers, nanofibers, and nanosheets as it can be seen in the SEM images of gold-coated cellulose samples (Figure 3.1). Figure 3.2 shows the optical microscope images of AgNWs.

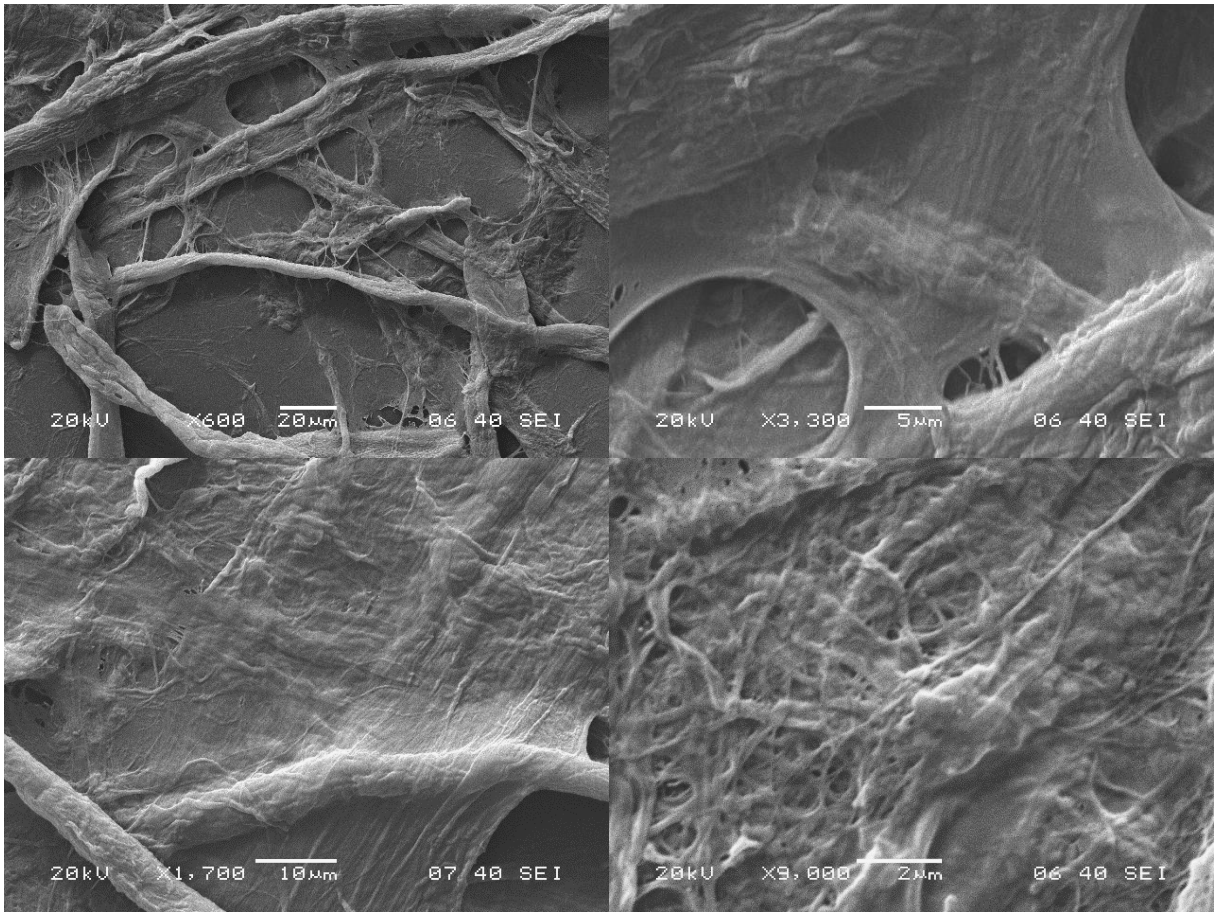

Figure 3.1. SEM images of disintegrated cellulose samples after gold-coating.

Figure 3.3a shows a photograph of the freestanding of PAni/RGO/cellulose/AgNWs composite film. The flexibility of the composite film is owing to the employment of the cellulose fibers that binds composite materials together. The controlled in-plane drying of the film causes more efficient binding and assembly of composite components. The SEM image in Figure 3.3b and its corresponding EDS spectrum in Figure 3.3c reveal the presence of AgNWs in the nanocomposite. The highly wrinkled and porous structure of the composite as well as the presence of AgNWs can be observed in SEM images provided in Figure 3.4. It should be noted that AgNWs contribute to the mechanical flexibility of the composite film in addition to improving its electrical conductivity. SEM images of the surface of PAni/cellulose film (without RGO and AgNWs) along with optical picture of the

film are provided in Figure 3.5 for comparison. Cellulose microfibers can be clearly recognized in Figure 3.5.

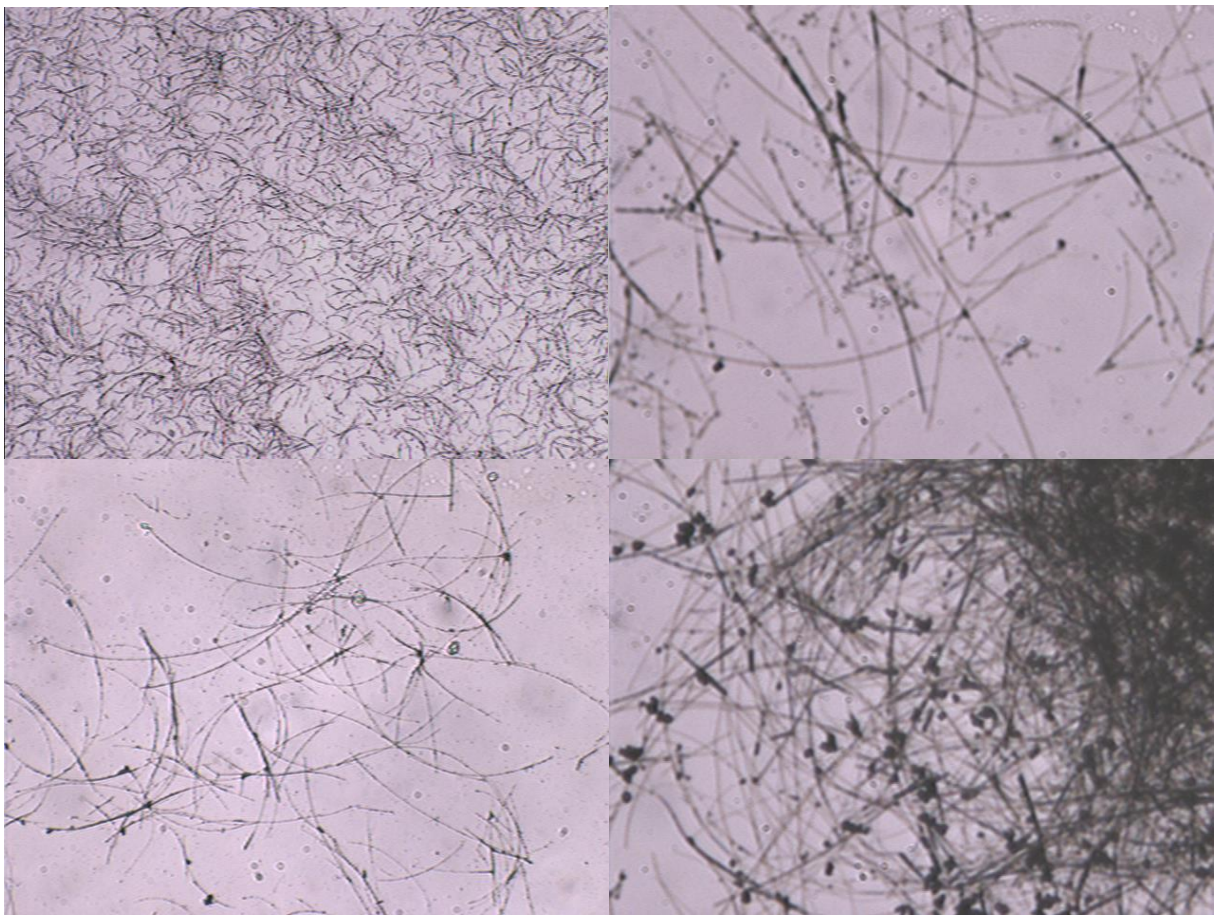

Figure 3.2. Optical microscope images of AgNWs.

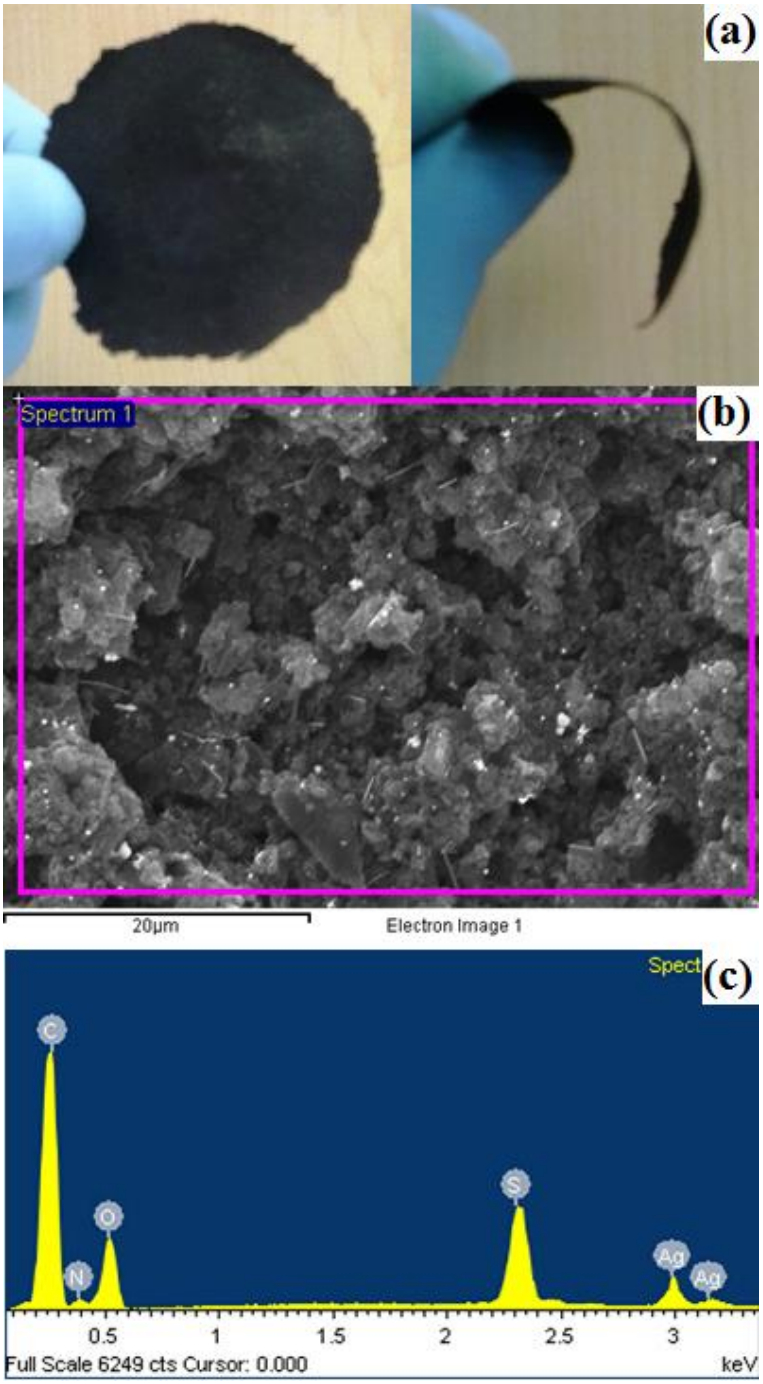

Figure 3.3. (a) Freestanding film of PAni/graphene/cellulose/AgNWs, (b) SEM images of the film, and (c) the corresponding EDX analysis of the film.

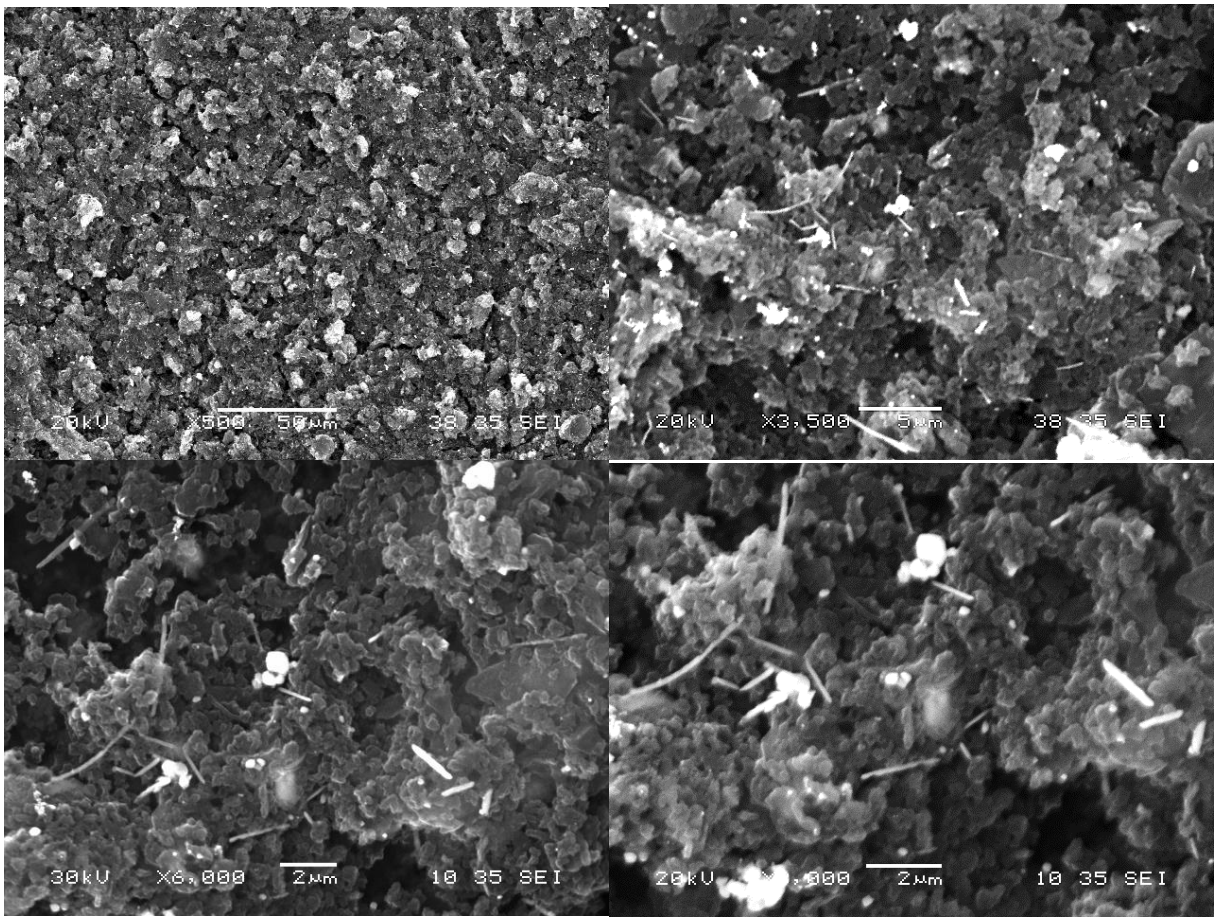

Figure 3.4. SEM images of the composite film with different magnifications.

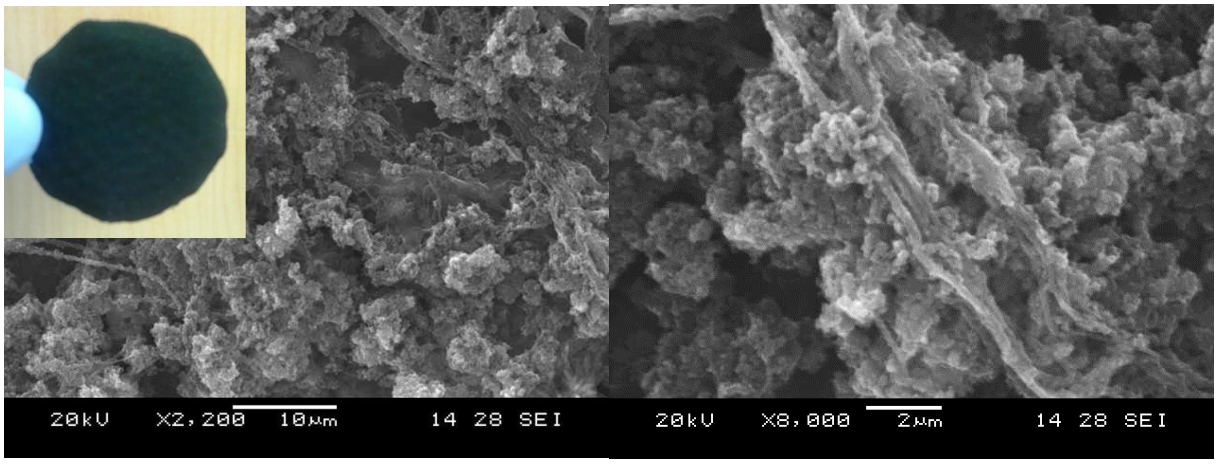

Figure 3.5. SEM images of the surface of PAni/cellulose film along with optical picture of the film.

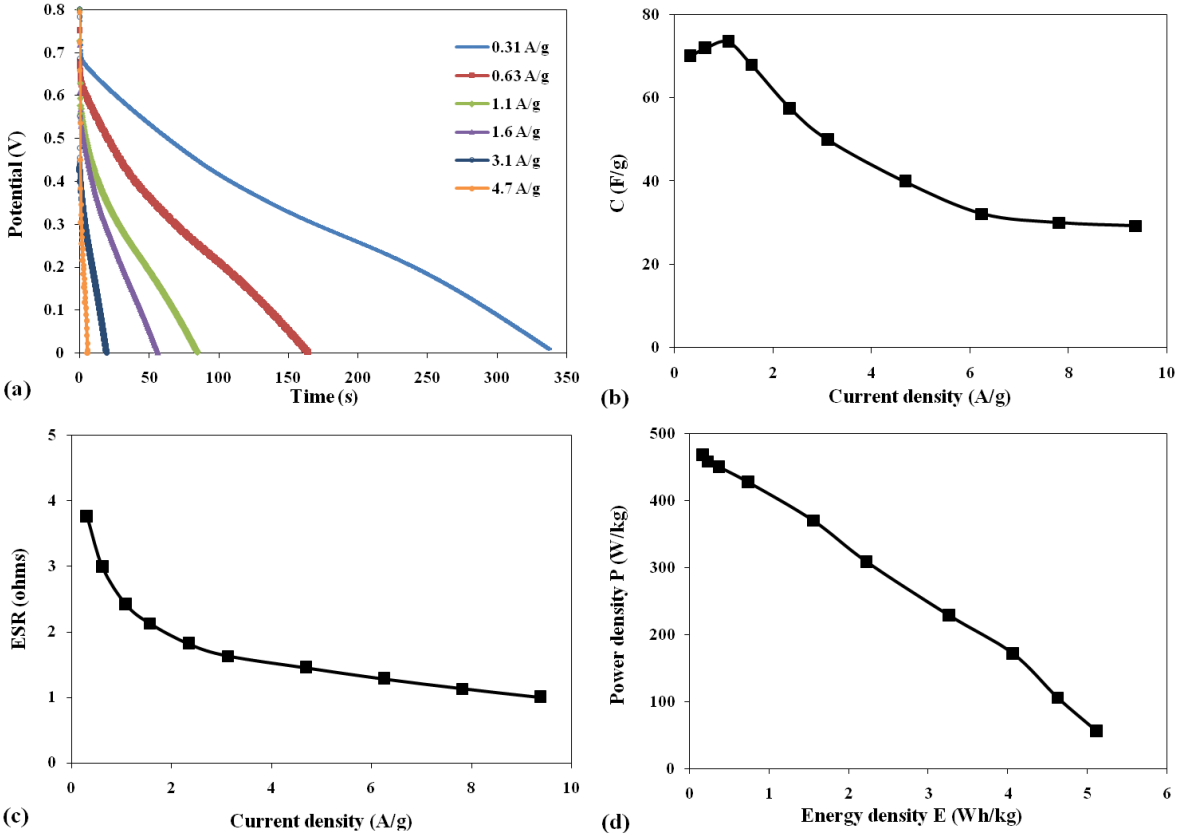

Figure 3.6. (a) GCD curves for different current densities, (b) Mass-specific capacitance versus current density, (c) ESR versus current density, and (d) Ragone plot.

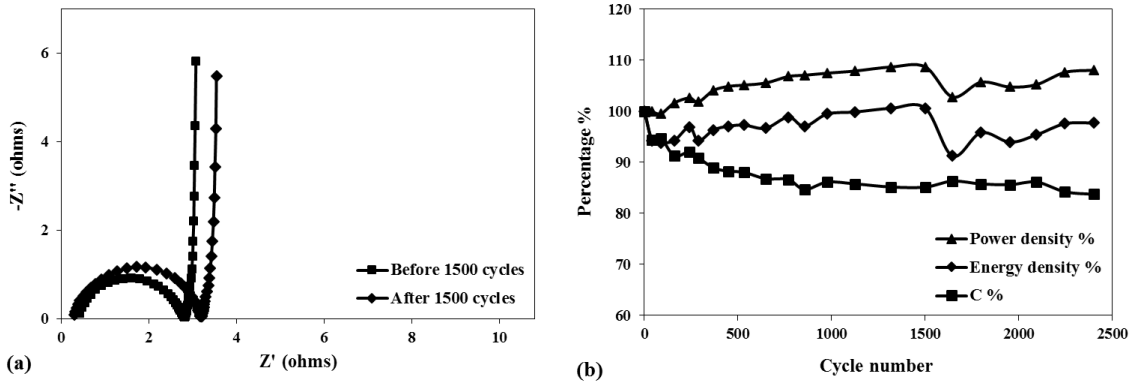

Figure 3.7. (a) Nyquist plots before and after 1500 cycles of GCD, (b) Cycling performance of the device for 2400 cycles of GCD at 1.6 A/g (percentages of power density, energy density, and capacitance versus cycle).

The electrochemical performance of the fabricated SC from the composite film of PAni/RGO/cellulose/AgNWs is evaluated by GCD and EIS tests. GCD curves for different current densities are plotted in Figure 3.6a to exhibit the electrochemical behavior of the SC.

It is observed that the potential drop decreases and the discharge time increases with a decrease in the current density as expected. Based on GCD tests, mass-specific capacitance versus current density, the corresponding Ragone plots (power density versus energy density), and ESR versus current density are illustrated in Figure 3.6b-d, respectively. It is noted that the electrochemical characteristics are calculated and presented for the whole fabricated device, i.e. two symmetric electrodes. According to Figure 3.6b, the specific capacitance first increases from 70.0 F/g (1.5 F/cm^2) to 73.4 F/g (1.6 F/cm^2) with an increase in the current density from 0.3 to 1.1 A/g; Then it reduces to 29.3 F/g (0.6 F/cm^2) when the current density is further increased to 9.4 A/g. Such gradual decrease in capacitance could be due to a reduction of redox reactions in PAni for larger current densities since the time constant for the redox reactions is much slower than that of double layer [3]. It should be noted that pseudocapacitance of PAni is the main source of capacitance in the composite material. The achieved maximum areal-specific capacitance of 1.6 F/cm^2 in the current design is higher than 0.5 F/cm^2, reported for a SC based on a 3D-RGO/PAni composite film with similar design and test conditions [55]. The as-prepared SC can be charge-discharged up to 9.4 A/g similar to 10 A/g, the maximum reported charge-discharged rate in the literature for PAni/graphene-based SCs [55-56], showing an excellent rate capability of the SC.

Contrary to constant resistance in conventional capacitors, ESR increases with decreasing the current in pseudocapacitance materials [1]. According to Figure 3.6c, ESR decreases with an increase in the current density due to a reduction of redox reactions for larger current densities. In other words, a lower current density facilitates more efficient redox of PAni and increases resistance due to transitions between emeraldine and pernigraniline states. Figure 3.6d indicates that the power density and energy density are inversely

proportional. In other words, with an increase in the current density, the power density increases while energy density decreases. It is observed that the as-prepared SC device exhibits a maximum power density of 468.8 W/kg at the discharge rate of 9.4 A/g and a maximum energy density of 5.1 Wh/kg at the discharge rate of 0.3 A/g.

Fig. 4a depicts Nyquist plots of the SC obtained from EIS before and after 1500 cycles of GCD at a current density of 1.6 A/g. The estimated ESR of the whole device from the Nyquist plot is 2.8 ohms (3.2 ohms after 1500 GCD cycles). The good cycling performance of the SC is inferred from the almost-unchanged shape of the Nyquist plot after 1500 cycles of GCD. To further study the cycling performance of the device, 2400 cycles of GCD are run at a current density of 1.6 A/g and the variation of percentages of power density, energy density, and capacitance versus cycle number are plotted in Fig. 4b. The percentages of power density, energy density, and capacitance are 108%, 98%, and 84%, respectively, showing the excellent cycle stability of the SC, which could be explained by the effective combination of PAni and RGO in the composite. In addition, the cellulose scaffold cushions the volume expansion of brittle PAni during repetitive doping/dedoping, which could contribute in improving the cycle life of PAni-based composites.

3.5 Conclusion

A high-performance SC has been developed using a flexible cellulose-based composite film of PAni, RGO and AgNWs. Cellulose fibers, extracted from tissue wiper, bind composite materials together and ensure flexibility of the composite film. AgNWs contribute to the mechanical flexibility of the composite film in addition to providing fast electron transportation channels to achieve high capacitance. The entire device has a suitable

flexibility, cycling stability and shows high capacitive behaviour. The ability to achieve a high specific capacitance could be attributed to high pseudocapacitance of PAni, the porous structure of the composite, the combination of PAni and RGO, and enhanced electron path provided by AgNWs. The quantities of PAni, RGO and AgNWs could be tuned to attain required power and energy density of the SC. A power density as high as 468.8 W/kg and an energy density as high as 5.1 Wh/kg can be obtained from the as-prepared SC device. The high capacitance, cycling stability, rate capability as well as facile fabrication process of flexible composite film make it a good candidate for wearable SCs.

In this work, AgNWs are utilized to enhance the conductivity of the electrode, and thus ultimately improve the power density of the PAni-based electrode. However, AgNWs precipitate from the dispersion due to their relatively heavy weight, leading to a nonhomogeneous composite film. In the next chapter, silver nanoparticles will be employed to enhance the conductivity of PAni-based electrodes. Moreover, high-quality graphene requires a cumbersome and costly procedure, and thus exfoliated graphite will be used instead of reduced graphene oxide because of its low cost and high conductivity. In the next chapter, flexible PAni-based composite films are designed to show superior electrochemical performances including excellent cycling stability and tunable energy and power densities.

Chapter 4:

Flexible Electrode Design: Freestanding Polyaniline-Based Composite Films for High-Performance Supercapacitors

4.1 Abstract

Polyaniline (PAni) is a promising pseudocapacitance electrode material. However, its structural instability leads to low cycling stability and limited rate capability which hinders its practical applications. In view of the limitations, flexible PAni-based composite films are developed to improve the electrochemical performance of electrode materials. This research reports a facile and cost-effective approach for fabrication of a high-performance supercapacitor (SC) with excellent cycling stability and tunable energy and power densities. SC electrode containing a very high mass-loading of active materials is a flexible film of PAni, tissue wiper-based cellulose, graphite-based exfoliated graphite (ExG) and silver nano-particles with potential applications in wearable electronics. The optimum preparation weight ratios of silver nitrate/aniline and ExG/aniline used in the research are estimated to be 0.18 and 0.65 (or higher), respectively. Our results show that an ultrahigh capacitance of 3.84 F/cm^2 (240.10 F/g) at a discharge rate of 5 mA can be achieved. In addition, our study shows that the power density can be increased form 1531.3 W/kg to 3000 W/kg by selecting the weight ratio of ExG/aniline more than 0.65, with a sacrifice in the energy density. The obtained promising electrochemical properties are found to be mainly attributed to an

effective combination of PAni, ExG, cushiony cellulose scaffold, and silver as well as the porosity of the composite.

4.2 Introduction

In designing SCs, electrode materials play an important role in their performance. The major factors on the design of electrode materials for SCs are capacitance, power and energy density, cycle life and stability, rate capability, and manufacturing cost. Polyaniline (PAni), a promising conducting polymer, has been extensively applied for SCs because of its faradaic pseudocapacitance, environmental stability, low cost, easy processability, and relatively good conductivity. However, PAni is a brittle material, exhibits poor cycling stability and limited rate capability, and has a low power density at a large current due to repeated swelling and shrinking resulted from the charge/discharge process.

To overcome the limitations of PAni, composite electrode materials are expected to be developed by combining carbon nanostructures with PAni. In such composites, PAni provides a source of high pseudocapacitance, while a carbonaceous material improves cycling stability and rate capability, and ensures a high power density at a large current. [10, 42-43] Graphene is a carbon nanostructures that has been widely employed in developing PAni-based composites. Yan et al. [50] constructed a graphene nanosheets/PAni composite by an in-situ polymerization of aniline in the presence of graphene. They found that not only graphene provides more active sites for the nucleation of PAni, but also it establishes a fast electron transfer path to facilitate an enhanced capacitance.

Later on, a lot of research has been conducted to develop graphene/PAni composite electrodes that have good cycling stability, high energy density, and high power density [51-

[58]. Despite the extensive research in graphene-based materials, there are still some issues such as the low specific area and conductivity of graphene-based composites [82]. On the other hand, because of the high cost and cumbersome production of good-quality graphene, alternative cheaper carbon nanostructures, such as exfoliated graphite (ExG) [83-87] , could be also used in designing PAni-based composites.

To further enhance the performance of PAni-based composites for SCs, silver nanoparticles (AgNPs) were often incorporated into composites [88-92]. AgNPs were found to not only improve the conductivity of PAni-based composites but also enhance their capacitance [89, 91]. Xia et al. [88] synthesized highly conductive PAni/AgNPs composites by an addition of sodium borohydride to PAni/silver nitrate solution. A composite of PAni/graphene/AgNPs was obtained using an in-situ polymerization of PAni in the presence of silver ions and graphene oxide (GO) for SCs with high specific capacitance and capacity retention [89]. The electrode was fabricated by spray-coating of the composite powder on a carbon fiber paper inferring that the as-prepared composite could not be formed into a flexible film. In addition to the high cost of a good-quality carbon fiber paper, its limited mass-loading of active materials (~4 mg/cm^2 in this case) makes the design not suitable for high energy and power applications. In other words, a SC design with small electrode mass-loading shows low area-specific capacitance although it might exhibit large mass-specific capacitance.

In recent years, much effort has been dedicated to achieve low-cost, environmentally-friendly, and flexible energy storage devices for wearable and portable electronics [93-94]. A major challenge is how to effectively construct a flexible film from a PAni-based composite. Therefore, an addition of a material that helps the formation of a freestanding and flexible

film, while maintaining electrochemical properties of an electrode, is indispensable. Cellulose, the most abundant organic polymer on earth, is a good candidate as an element of nano-composites for flexible electronic devices owing to its chemical reactivity and physical properties. Due to the presence of multiple hydroxyl groups on cellulose [79], numerous hydrogen bonds can be formed with a wide range of materials. In addition, this abundant, economical, environmentally-friendly, biodegradable, renewable, and flexible polymer has received a great deal of attention for flexible electronics [78-79]. Zhang et al. [80] constructed a solid-state SC by electrodepositing PAni onto cellulose aerogel/AgNPs. Their flexible device exhibited a small specific capacitance of 176 mF/cm^2 at 10 mV/s possibly due to the limited mass-loading of PAni. PAni was in-situ synthesised in a cellulose/CNT matrix. Shi et al. [81] fabricated a cellulose/CNT film as a template for in-situ synthesis of PAni for flexible SCs with enhanced cycling stability. However, the limited mass-loading of PAni on a cellulose/CNT films (~1.3 mg/cm^2 in this case) could restrict the high energy and power requirements for most practical applications in wearable electronics. Hence, it is indispensable to design flexible PAni-based electrodes of SCs that are low cost and environmentally friendly and could have high mass-loading of active materials, while exhibiting long cycle life, rate capability, high power density, and high energy density.

Here a new design for the fabrication of a flexible film based on PAni, cellulose, ExG and AgNPs for low-cost high-performance SCs is reported. The quantity of each component in the composite is carefully engineered through experiments to fulfill all the above-mentioned features of a high-performance SC. The idea is to incorporate several components in one composite structure to overcome the disadvantage of each component and build a structure with multiple benefits. PAni is the main source of the faradic charge

storage of the composite film. ExG enhances the capacitance through double-layer charge storage and improves the conductivity, cycling stability, and rate capability of the composite electrode. Cellulose is the backbone and the source of flexibility and the consistency of the composite film. Finally, AgNPs enhance the capacitive performance of the composite electrode [89, 91]. The fabrication process is pretty simple and the materials are low cost and environmental friendly. In a typical preparation process, first ExG is synthesized through an electrochemical exfoliation of graphite rods followed by a post-exfoliation in a microwave. Afterwards, aniline is in-situ polymerized in the presence of ExG, cellulose, and silver nitrate to prepare a nano-composite mixture. The as-prepared mixture is then vacuum-filtered to obtain a freestanding thin film followed by a controlled in-plane drying. To attain the best electrochemical performances, the ratios of ExG and silver nitrate to aniline are optimized through various experiments.

4.3 Experimental Methods

4.3.1 Preparation of the ExG

Parvez et al. [87] conducted an electrochemical exfoliation of graphite flakes in aqueous solutions of different inorganic salts such as ammonium sulfate, sodium sulfate, and potassium sulfate. However, the majority of the products based on this method are graphitic particles (micro- and nano-particles) rather than graphene. To enable mass-production of highly conductive ExG, we use a similar procedure to obtain graphite particles followed by a post-exfoliation in a microwave [95-96], which results in ExG with higher conductivity than graphitic particles. In other words, graphene layers attached together in graphitic particles are further exfoliated. In a typical synthesis in the fume hood, two graphite rods (6.3 mm in

diameter), as an anode and a cathode, are displaced a distance of 1 cm apart in 0.1 M aqueous solutions of sodium sulfate. A voltage (12 V) is applied to carry out the electrochemical exfoliation of the anode. The product is then sonicated at a low power for 30 min and is maintained for 10 min to precipitate large-sized graphite particles. The top part of the dispersion is washed with deionized water by vacuum filtration through a Whatman filter paper (grade 5 with pore size of 2.5 μm) and dried in a vacuum oven overnight. To obtain the ExG, the graphite particles are then irradiated in a microwave under the power of 700 W for 20 to 50 seconds depending on the quantity of particles. After microwave irradiation, which might be accompanied by fuming and lightening, the volume expansion of the ExG powder is clearly observed.

To further investigate the distribution of graphite particles, smaller sized particles are extracted by centrifuging at a speed of 2000 rpm and collecting the top part of the dispersion.

4.3.2 Preparation of PAni/ExG/Cellulose/AgNPs Composite Film

A combination of 0.05 g silver nitrate ($AgNO_3$, ≥99.0%) and 182 mg ExG are added into 20 mL deionized water and sonicated with a probe Q700 sonicator (Qsonica, LLC., China) at 300 W for 30 min (6 s on and 1 s off in an ice bath). After the addition of 0.28 mL aniline (≥99.5%), the mixture is sonicated in an ultrasonic cleaner (VWR International, LLC., USA) at 100 W for another 30 min.

Cellulose fibers are prepared from a tissue wiper pulped in a water-containing beaker by means of a mechanical homogenizator according to Section 3.3.1.

Following the sonication, 22 mg cellulose fibers dispersed in 22 mL of 1 M H_2SO_4 are slowly poured into the aniline/ExG/$AgNO_3$ mixture and stirred for 30 min to let the aniline

and ExG be absorbed in the cellulose matrix (solution A). The concentration of cellulose is adjusted to result in a composite film with a desired flexibility. Another solution is also prepared by adding 0.35 g ammonium persulfate (APS, ≥98.0%) to 10 mL of 1 M H_2SO_4 (solution B). To carry out the in-situ polymerization of aniline in the presence of cellulose, ExG and $AgNO_3$, solution B is added into the solution A and stirred at the ambient temperature for 6 hours (the mixture turns dark green after 15 min). It is noted that APS is a strong oxidant and $AgNO_3$ is a weak oxidant. One part of silver ions are reduced while aniline is being oxidized to PAni; and excess silver ions are reduced to AgNPs with formerly produced PAni nanofibers (PAni in emeraldine form is able to reduce silver ions to silver and PAni is converted to pernigraniline form at the same time) [92]. To form a thin film, the as-prepared mixture is then vacuum-filtered through a filter paper (Whatman, grade 5) followed by washing with deionized water. The composite film of PAni/ExG/cellulose/AgNPs is then obtained by peeling it off from the filter paper. Finally, the diameter of the freestanding and flexible composite film is reduced from 44 mm to around 30 mm by a controlled in-plane contraction through drying between two plastic sheets at the ambient temperature.

A similar procedure is used to prepare PAni/cellulose/AgNPs composite by only omitting ExG. To study and find an optimal composition of PAni/ExG/AgNPs with the best possible electrochemical performance, seven different samples are presented herein (Table 1). The weight ratio of $AgNO_3$/aniline in PAni/cellulose/AgNPs composite is first studied with samples S1, S2, and S3. Then, the effect of weight ratio of ExG/aniline in PAni/ExG/cellulose/AgNPs composite is demonstrated with samples S4, S5, S6, and S7.

Table 4.1. Composition of different samples fabricated based on weight ratios to aniline.

Sample	Aniline (μL)	ExG/ aniline	$AgNO_3$/ aniline	Cellulose/ aniline
S1	330	0	0.13	0.067
S2	330	0	0.18	0.067
S3	330	0	0.24	0.067
S4	280	0.76	0.18	0.079
S5	280	0.65	0.18	0.079
S6	280	0.58	0.18	0.079
S7	280	0.50	0.18	0.079

4.3.3 Characterization

A scanning electron microscope (SEM; JSM-5900LV, SEMTech Solution, USA) is used to observe the morphology of films. The atomic force microscopy (AFM) topographies of ExG before and after post-exfoliation are obtained using Nanosurf easyScan 2 (Nanoscience Instruments, Inc.; ACLA probe, Applied NanoStructures, Inc., USA). The sheet resistance of films is measured by the standard four-probe method. Fourier transformed infrared (FTIR) spectra are recorded on a Thermo Nicolet iS10 FTIR Spectrometer.

To perform electrochemical tests, flexible composite films are assembled in a symmetric two-electrode system to form a SC. Briefly, two rectangular strips (2 cm×1.5 cm) of a fabricated film as electrodes are soaked in 1 M H_2SO_4 for 5 hours to redope PAni. Then, the two electrodes, separated by a filter paper (Whatman, grade 5) wetted in 1 M H_2SO_4, are sandwiched between two thin stainless-steel sheets as the current collectors into a layered structure. The as-prepared SC is then sealed using a parafilm to prevent water evaporation. The approximate dried weight of each electrode in preparations of samples ranges from 45 to 63 mg.

The electrochemical performances of assembled SCs from each sample are investigated using an electrochemical workstation (CS350, WUHAN CorrTest Instruments Inc., China). The electrochemical impedance spectroscopy (EIS) tests are carried out with a frequency range from 10^5 to 0.01 Hz and an AC amplitude of 10 mV and zero DC amplitude. The galvanostatic charge/discharge (GCD) measurements are performed from 0 to 0.8 V at a constant current ranging from 5 to 400 mA. The cyclic voltammetry (CV) curves are recoded from 0 to 0.8 V at scan rates ranging from 0.002 to 1 V/s. The capacitance derived from GCD curves is estimated from the discharging slope after the IR drop, V_{IR} (the potential drops at the initial discharge stage, which is mainly attributed to the intrinsic resistance of the electrode material and the resistance of the electrolyte), based on $C = 2I\Delta t/(\Delta V - V_{IR})$, where, Δt represents the time of a full discharge, I is the discharge current, and ΔV is the potential change after a full discharge. Mass-specific capacitance and areal-specific capacitance are determined by dividing C by m and A, respectively, where m is the mass of one electrode (which includes PAni, ExG, cellulose and silver), and A is the area of one electrode. The equivalent series resistance (ESR) is calculated using $ESR = V_{IR}/2I$. The energy density (E) and power density (P) are estimated according to the following equations: $E = C(\Delta V - V_{IR})^2/2m = I(\Delta V - V_{IR})\Delta t/2m$ and $P = E/\Delta t$ respectively. The mass loading (in mg/cm^2) was calculated by dividing the total weight of an electrode by its geometric area.

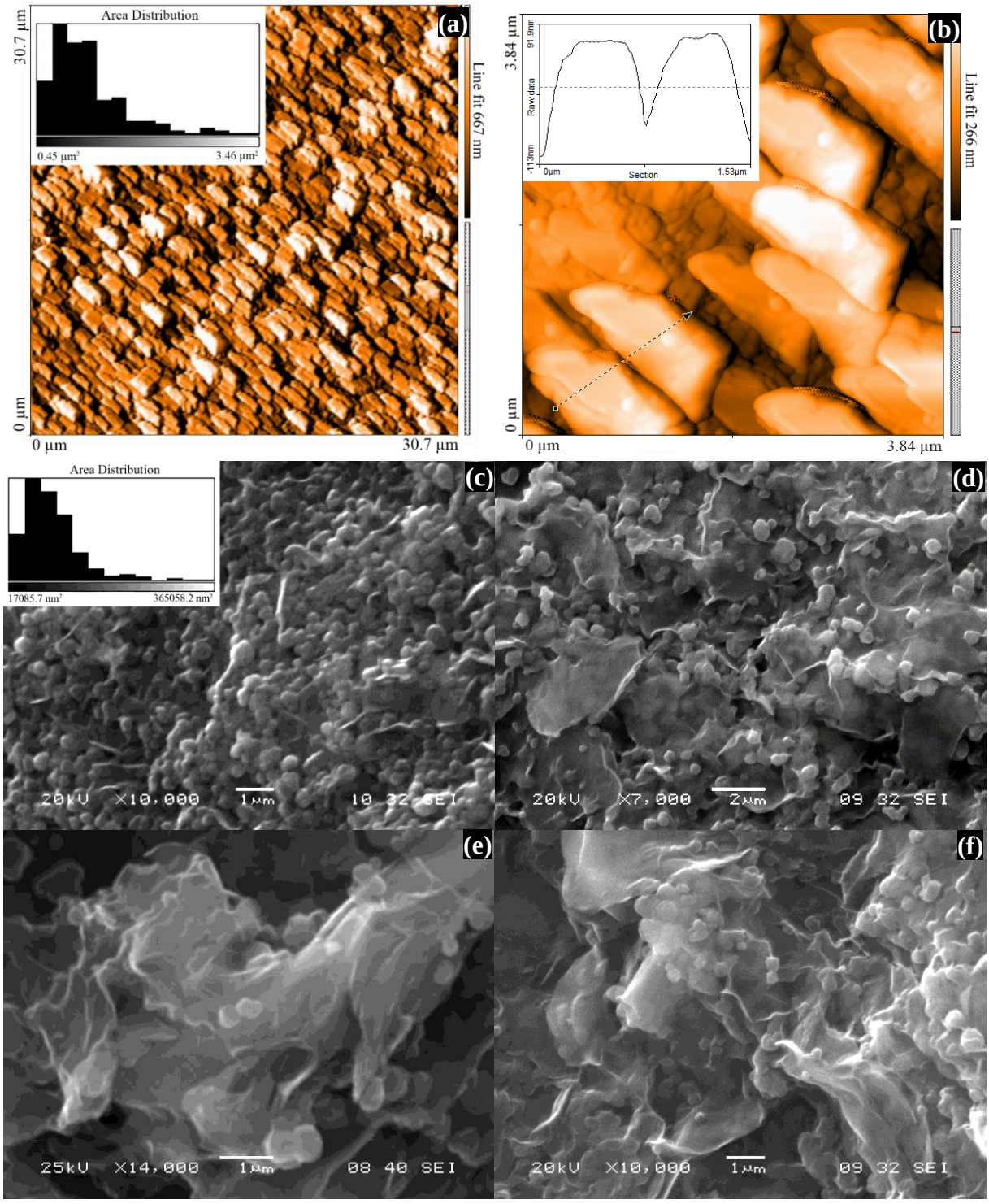

Figure 4.1. (a) AFM image of graphite micro-particles (inset: area distribution), (b) higher magnification AFM image of graphite particles (inset: cross-section of two particles), (c,d) SEM images of small-size graphite particles along with single-layered graphene, (e,f) SEM images of ExG.

4.4 Results and Discussion

The products of electrochemical exfoliation of graphite rods includes micro- and nano-sized graphite particles in addition to graphene sheets. Figure 4.1a shows AFM image of the micro-sized graphite particles (before microwave irradiation) and the corresponding in-plane area distribution of particles in the image. Figure 4.1b exhibits higher magnification AFM image of the graphite particles and the cross-section of two particles. As seen in Figure 4.1b, graphite particles contain nano-sized particles as well. To further characterize the distribution of smaller sized particles, the dispersion graphite particles in water are centrifuged at a speed of 2000 rpm and the top part of the dispersion is collected. The nano-sized graphite particles along with some single-layered graphene are observed in SEM image (Figure 4.1c and d). SEM image in Figure 4.1d more clearly shows high-quality single-layered graphene sheets. According to in-plane area distribution of graphite particles, micro-sized and nano-sized particles have an average in-plane area of 1.14 μm^2 and 0.09 μm^2, respectively. In the post-exfoliation process, microwave irradiation of graphite particles causes a separation of graphene layers in each graphite particle and consequently large volume expansion of particles. Therefore, the post exfoliation yields more high-quality graphene through further exfoliation of graphite particle. The wrinkled structure of graphene layers is observed in the SEM images of ExG (graphite particles after microwave irradiation) provided in Figure 4.1e and f. According to Energy-dispersive X-ray spectroscopy (EDS) spectrum of graphite particle and ExG (see Figure 4.2 and Table 4.2), a slightly higher atomic percentage of oxygen in ExG implies a very slight oxidation of graphite particles during microwave irradiation due to fuming and lightening. The tiny amount of oxygen in graphite particles originated from the oxidation of graphite by OH^-

ions during the electrochemical exfoliation process [87]. Using a four-point probe system, sheet resistances ($R_{\square}$) of graphite particles/cellulose and ExG/cellulose films are determined to be 437 Ω/□ and 116 Ω/□, respectively. Hence, the as-prepared ExG is four times more conductive than graphitic particles confirming the effective post-exfoliation of graphitic particles.

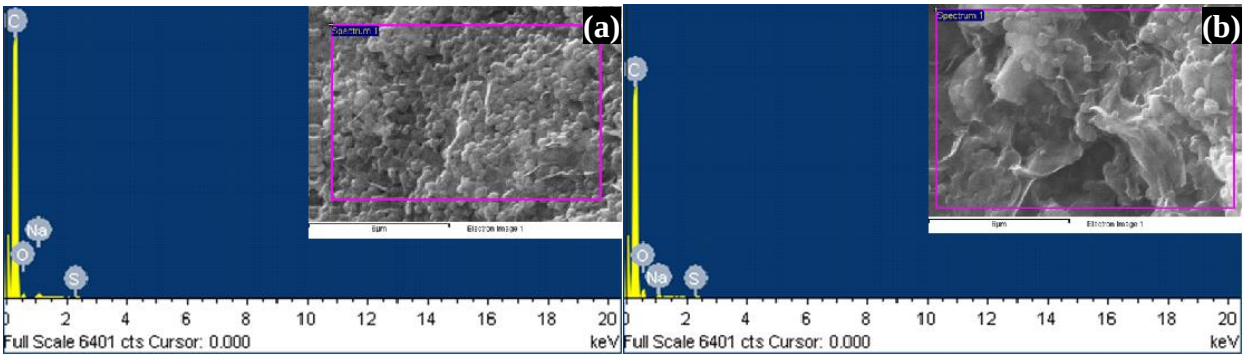

Figure 4.2. EDS spectrum of (a) graphite particles, and (b) ExG.

Table 4.2. Atomic percentage of elements in the EDS spectrums in Figure 4.2.

Sample	C Atomic%	O Atomic%	Na Atomic%	S Atomic%
Graphite particles	93.69	5.78	0.45	0.08
ExG	88.57	11.02	0.27	0.14

Figure 4.3a displays a photograph of the freestanding and the flexible composite film of PAni/ExG/cellulose/AgNPs (S5), which have enough flexibility for wearable electronic applications. The high flexibility of the film is attributed to the usage of the cellulose scaffold that binds the composite components together. In addition, the effective binding and assembly of composite components in the cellulose network is enabled through the controlled in-plane drying of the film [65].

The EDS spectrum of the composite film in Figure 4.3b demonstrates the presence of AgNPs as well as other constructing elements of the composite film such as carbon, nitrogen, oxygen, and sulfur. In addition, the well distribution of AgNPs in the film of PAni/ExG/cellulose/AgNPs can be seen from the EDS mapping of silver in Figure 4.4.

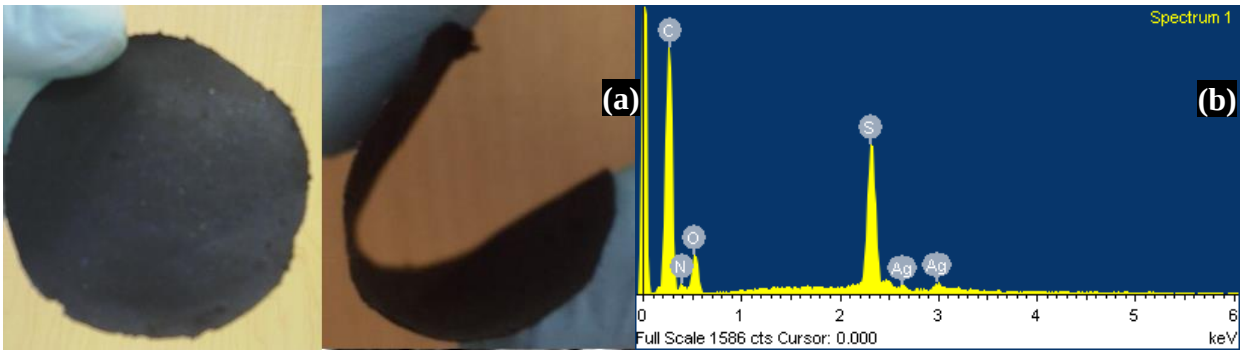

Figure 4.3. Freestanding film of PAni/ExG/cellulose/AgNPs,(b) EDS spectrum of the film.

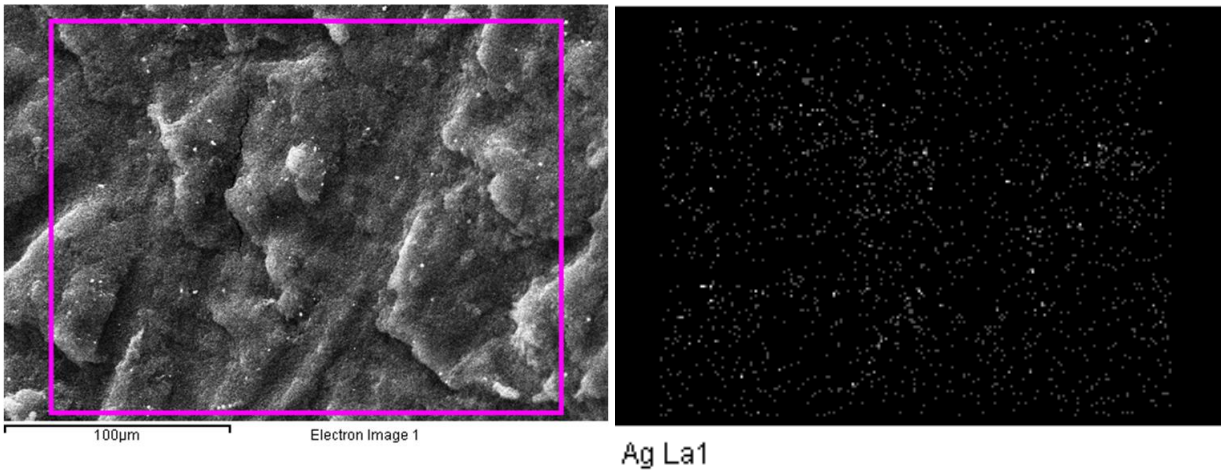

Figure 4.4. EDS mapping of silver in the film of PAni/ExG/cellulose/AgNPs

SEM images in Figure 4.5 confirm the highly porous structure of the composite, which facilitates an effective penetration of the electrolyte into the composite electrode materials. Two forms of PAni can be observed from SEM images (top-right image particularly) in Figure 4.5: short PAni nanowires grown on graphene layers of ExG and interconnected PAni nanofibers grown in the texture of cellulose fibers. Figure 4.6 exhibits SEM images of the

surface of PAni/cellulose/AgNPs film (S2). Well-grown interconnected PAni nanofibers in the texture of cellulose fibers and high porosity of the composite can be observed.

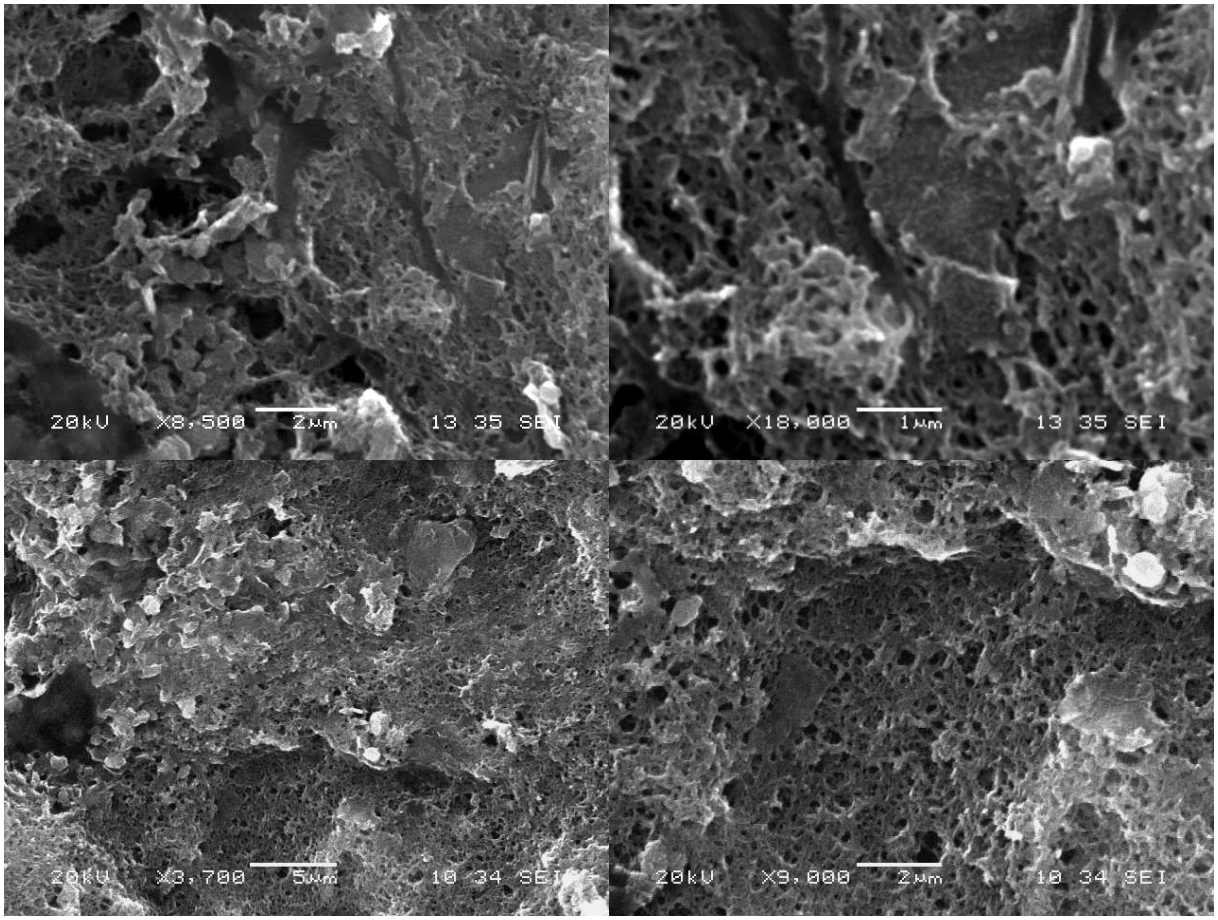

Figure 4.5. SEM images of PAni/ExG/cellulose/AgNPs film surface.

FTIR spectra of ExG, graphite particles, PAni, PAni/cellulose, PAni/cellulose/AgNPs (S2), PAni/ExG/cellulose/AgNPs (S5), and cellulose (tissue wiper) are shown in Figure 4.7. The FTIR spectrum of graphite particles displays peaks at 1575 cm^{-1} (strong; aromatic C=C), 1635 cm^{-1} (aromatic C=C), 1717 cm^{-1} (C=O), 2851 cm^{-1} (C-H), 2920 cm^{-1} (C-H) and 3434 cm^{-1} (O-H), all of which are due to stretching vibrations and are similar to those of graphene [55, 89] functionalities. The FTIR spectrum of ExG also contains the same peaks but with lower intensities. In addition, the band of C-O stretching vibration at 1225 cm^{-1} in the

graphite particles is due to the slight oxidation of graphite during the electrochemical exfoliation process. In the FTIR spectrum of ExG, the new peaks at 1055 cm^{-1}, 1264 cm^{-1}, and 1299 cm^{-1} are attributed to C-O stretching vibration, which again confirm a further oxidation of graphite particles during microwave irradiation. Moreover, the FTIR spectrum of ExG shows new peaks at 690 cm^{-1} (sp^2 C-H bending), 1402 cm^{-1} (sp^3 C-H bending), and 3138 cm^{-1} (O-H stretching).

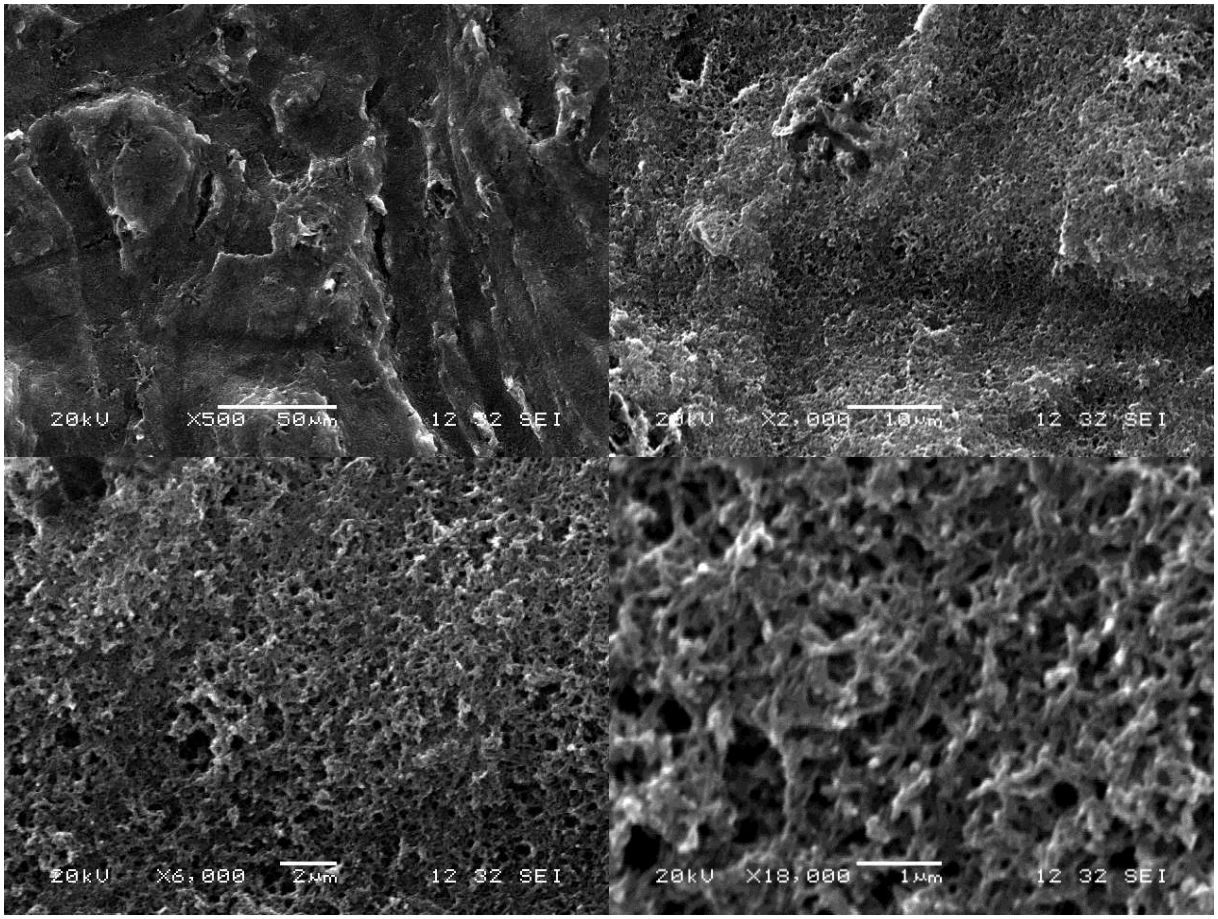

Figure 4.6. SEM images of the surface of PAni/cellulose/AgNPs film (low to high magnification).

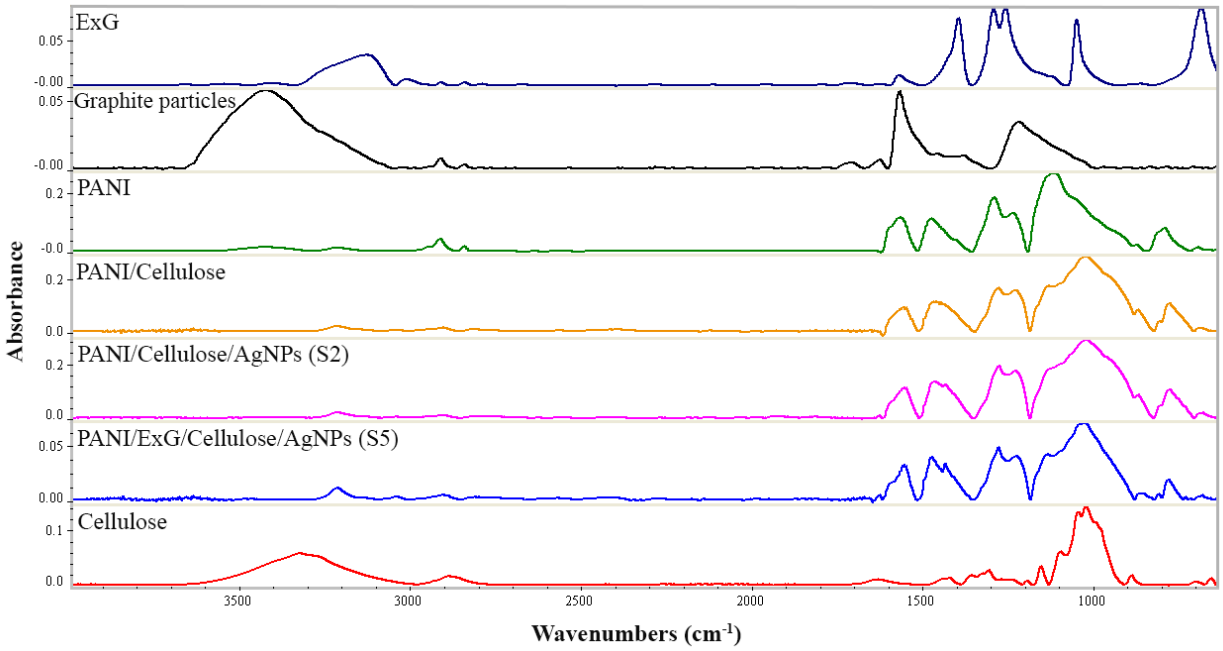

Figure 4.7. FTIR spectra of different samples.

The FTIR spectrum of PAni gives typical peaks at 798 cm^{-1} (aromatic C-H out-of plane bending), 1123 cm^{-1} (aromatic C-H in-plane bending), 1298 cm^{-1} (aromatic amine C-N stretching), 1485 cm^{-1} (benzenoid ring C=C stretching), 1566 cm^{-1} (quinoid ring C=C stretching), and 3437 cm^{-1} (N–H stretching), indicating that PAni is in the emeraldine salt state [53, 55, 97].

The FTIR spectrum of tissue wiper presents typical peaks of cellulose at 896 cm^{-1} (C-H bending), 1031 cm^{-1} (C-O stretching), 1162 cm^{-1} (C-O stretching), 1429 cm^{-1} (alkane C-H bending), 1640 cm^{-1} (O-H bending of absorbed water), 2897 cm^{-1} (C-H stretching), and 3333 cm^{-1} (O-H stretching).

According to FTIR spectra of PAni/cellulose, PAni/cellulose/AgNPs (S2), and PAni/ExG/ cellulose/AgNPs (S5), all three samples have all absorption peaks of pure PAni, indicating that PAni has been successfully coated on cellulose and ExG. As seen in Figure 4.7, all three cellulose-containing samples have an additional absorption peak at 1030 cm^{-1}

(C-O stretching vibration), originated form cellulose. It should be noted that the FTIR spectrum of S5 has absorption peaks with lower intensity compared to those of PAni/cellulose and S2, since a large amount of infrared beam is absorbed by ExG.

The assembly mechanism of the composite components can be briefly explained as follows. ExG is absorbed by cellulose fibers through hydrogen bonding between multiple hydroxyl groups of cellulose and hydroxyl groups of ExG. At the same time, aniline is adsorbed on cellulose fibers and ExG through amino group of aniline by hydrogen bonding. Upon the in-situ polymerization of aniline, PAni fibers are coated on both cellulose and ExG via hydrogen bonding with amine group groups [81] of PAni. Lastly, silver ions are reduced to AgNPs during the polymerization of aniline.

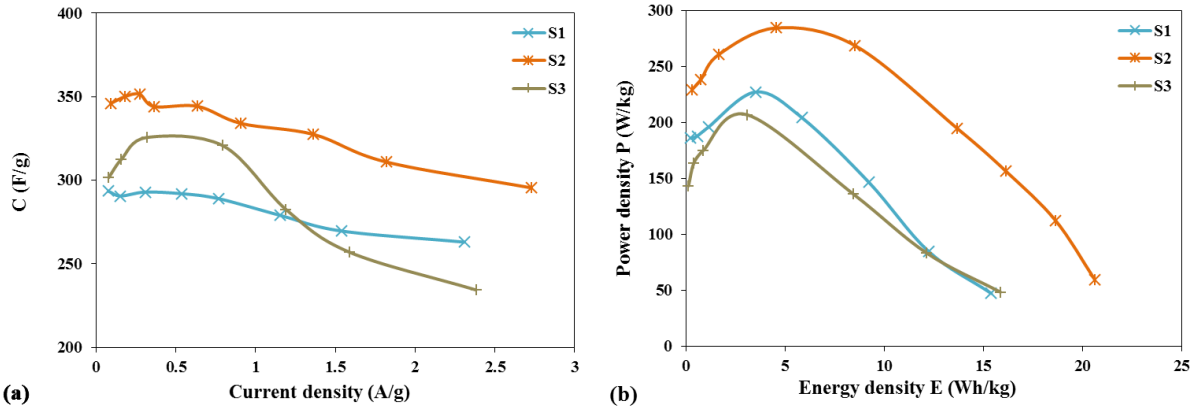

Figure 4.8. SCs based on PAni/cellulose/AgNPs; (a) Mass-specific capacitance versus current density, (b) Ragone plots, for three weight ratios of $AgNO_3$/aniline. All values are calculated based on one electrode.

The electrochemical performance of SCs assembled from different samples is evaluated by GCD and EIS tests in two-electrode systems. The positive effect of AgNPs on the capacitance of PAni-based composites has been already acknowledged. [89, 91] Therefore, we adjust the $AgNO_3$/aniline ratio to achieve the best electrochemical performance. To demonstrate the effect of the weight ratio of $AgNO_3$/aniline on the performance of PAni/cellulose/AgNPs composite, mass-specific capacitances versus current density for

three samples (S1, S2, and S3) are calculated from GCD tests and illustrated in Figure 4.8a. The corresponding Ragone plots (power density versus energy density), at different current densities, are also depicted in Figure 4.8b. It is found that the specific capacitances of samples S1, S2, and S3, estimated at a discharge current of 75 mA, are 278.97, 327.36, and 286.96 F/g, respectively. We can conclude that, for a value of current density, the specific capacitance, power density and energy density of S2 are higher than those of S1 and S3, implying that the optimum weight ratio of $AgNO_3$/aniline in the composite is around 0.18. Furthermore, at the same discharge current of 75 mA, the power densities of samples S1, S2, and S3 are 195.67, 260.84, 174.83 W/kg, respectively; and their corresponding energy densities are 1.11, 1.66, 0.86 Wh/kg. Interestingly S3, with 0.24 $AgNO_3$/aniline weight ratio, shows inferior electrochemical performance compared to S2 due to two possible reasons. Firstly, in spite of enhancing the conductivity of the composite, silver deducts the share of PAni in a mass unit of the composite. So there should be a balance in the amount of silver in the composite in order to attain the best possible performance. Secondly in the process of preparing PAni/AgNPs, some amount of emeraldine PAni (conducting state) is converted to pernigraniline (semiconducting state) in the reduction of excess silver ions to AgNPs. Therefore, S3 would have more PAni in pernigraniline state compared to S2 since S3 has more silver ions. It is also observed that the S2 film had a dark-green color while S3 film had a dark-blue/purple color implying the difference in the amount of pernigraniline form of PAni.

After adjusting $AgNO_3$/aniline weight ratio, the effect of ExG/aniline weight ratio on the performance of PAni/ExG/cellulose/AgNPs composite is investigated. Based on GCD curves for different current densities, mass-specific capacitance, Ragone plots, and ESR for

five samples (S4, S5, S6, S7 and S2) are illustrated in Figure 4.9a-c, respectively. In addition, their corresponding Nyquist plots obtained from EIS are plotted in Figure 4.9d.

According to Figure 4.9c, ESR decreases by increasing the discharge current in all samples and this decrease rate is larger for current densities lower than ~2 A/g. For a low current density (<~2 A/g), there is more time for redox reactions of PAni to occur which leads to more effective oxidation of PAni from the emeraldine (conducting state) to the pernigraniline (semiconducting state) in one electrode and reduction in the other electrode. Therefore, the total resistance of the SC is higher when it is discharged with a lower current density due to the partly or fully transformation of PAni to other states (transitions between a conducting state and a semiconducting state) [1]. In contrast, for a larger discharge current, there is a limited time for redox reactions of PAni to happen in the electrodes due to the longer time constant of the redox reactions (as opposed to the shorter time constant of the electrical double-layer process that happens in ExG). Therefore, the variation of ESR for current densities higher than ~2 A/g is small, similar to the case for carbon nanostructures such as graphene, and ExG. In addition, ESR and the potential drop (V_{IR}) are smaller for samples with a higher ExG amount, which reveals that an incorporation of ExG into the composite improves the charge-transfer of the electrochemical process. For instance, ESR of S4, S5, S6, S7 and S2 are determined at a discharge current of 50 mA as 1.01, 2.17, 2.49, 3.69, and 4.87 Ω. Nyquist plots in Figure 4.9d, consistent with Figure 4.9c, also confirm that the charge-transfer resistance of the electrochemical process is lower for samples with a higher ExG amount.

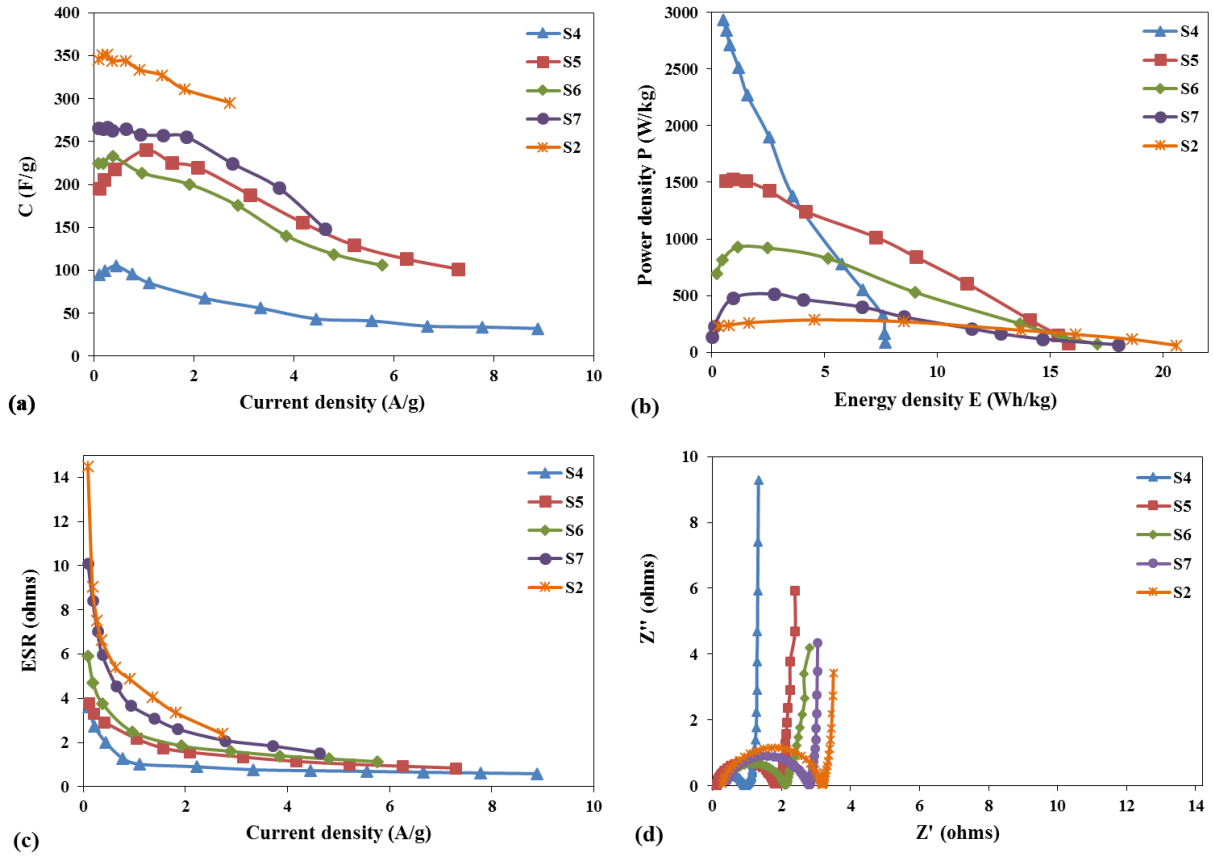

Figure 4.9. SCs based on PAni/ExG/cellulose/AgNPs; (a) Mass-specific capacitance versus current density, (b) Ragone plots, (c) ESR versus current density, and (d) Nyquist plots, for five weight ratios of ExG/aniline. All values in (a-c) are calculated for one electrode.

It is seen from Figure 4.9a and c that S4, S5, S6, S7 and S2 can be charged and discharged with current densities up to 8.89, 7.29, 5.77, 4.63, and 2.72 A/g, respectively. This indicates that samples with a higher ExG amount show better rate capability since they can operate in larger current densities.

According to Figure 4.9a, the specific capacitances of S4, S5, S6, S7 and S2, calculated at a discharge current of 100 mA, are 67.38, 219.83, 200.22, 255.57, and 310.90 F/g, respectively. Hence it is concluded that S4 and S2 exhibit the lowest and highest capacitance, respectively; and the capacitances of S5, S6, and S7 are in a similar range. The highest specific capacitance of S5 is 240.10 F/g (3.84 F/cm^2), estimated from GCD at a

discharge rate of 1.04 A/g; which is 2.3 times larger than highest capacitance of S4. The pseudocapacitance of PAni in the composite film is enhanced by highly conductive components, i.e. ExG and AgNPs, through forming conducting networks for improving the redox activity of PAni.

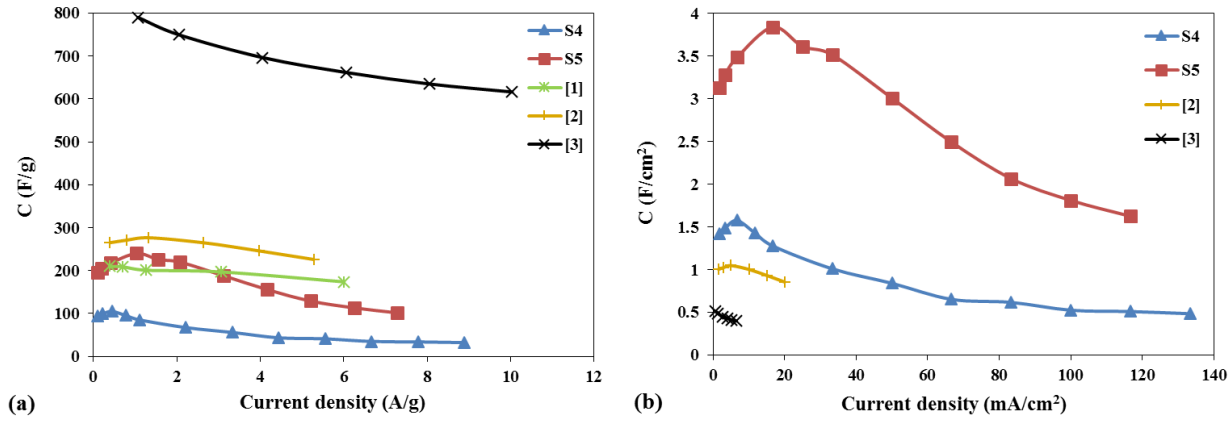

Figure 4.10. Comparison of mass-specific capacitance (a) and area-specific capacitance (b) of S4 and S5 with those of three references [51, 55-56] based on flexible films of PAni/graphene.

To highlight the large area-specific capacitance of our device, we compare mass-specific capacitance and area-specific capacitance of S4 and S5 with those of three references based on flexible films of PAni/graphene and with similar test conditions (Figure 4.10). The maximum capacitance of each electrode in the current work (S5), references [51], [55], and [56] are 240 F/g (3.84 F/cm^2; mass-loading of one electrode is 16.00 mg/cm^2), 210 F/g (no electrode mass was reported), 277 F/g (1.05 F/cm^2; ~3.75 mg/cm^2), and 790 F/g (0.51 F/cm^2; 0.65 mg/cm^2), respectively. It is seen that SCs based on PAni/graphene in references [55], and [56] exhibit higher mass-specific capacitance (and lower area-specific capacitance) than S4 and S5. For instance, Meng et al. [55] fabricated a porous graphene/PAni composite film for electrodes of flexible SCs with excellent performance. To construct a flexible film of PAni/graphene in such a design, a very thin film was fabricated with a mass-loading of active materials around 3.75 mg/cm^2 that resulted in a smaller area-specific capacitance but higher mass-specific capacitance compared to the current

work. However, such a device does not necessarily show the same mass-specific capacitance when the mass-loading of electrodes increases, e.g. from 3.75 to 16 mg/cm^2. In addition, enlarging the film thickness (or area density of the film) in such designs might not be possible due to brittle nature of PAni/graphene or design limitations. Likewise, the limited mass-loading of active materials in the flexible film based on graphene/PAni in reference [56] could restrict its applicability for high-capacitance requirements. A low mass-loading of electrodes could similarly restrict high energy and power requirements for most practical applications in wearable electronics. Thus, an advantage of the current design is the ultrahigh area-specific capacitance enabled by a large mass-loading of electrodes owing to the flexible nature of cellulose as the backbone of the composite film.

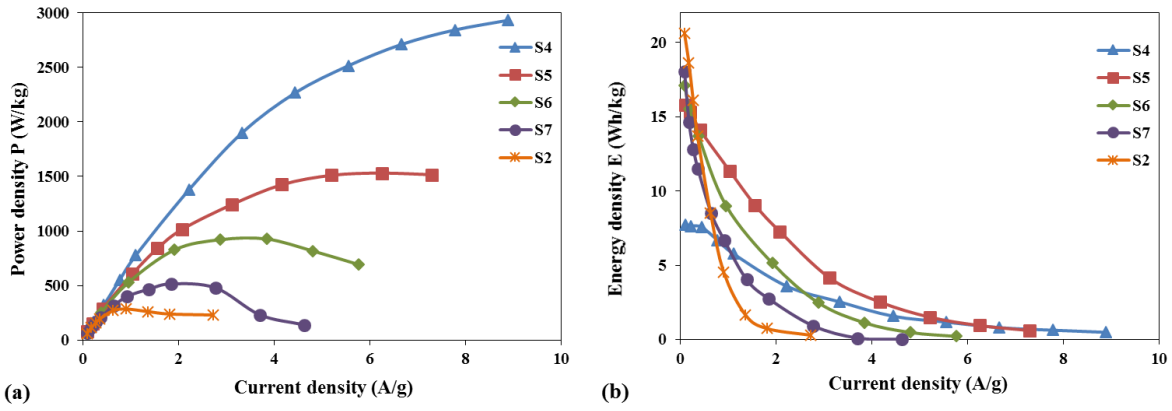

Figure 4.11. (a) Power density versus current density, (b) energy density versus current density, for five weight ratios of ExG/aniline.

Ragone plots in Figure 4.9b imply that power density is increased with an increase in the ExG amount for any value of the current density (also see Figure 4.11a), revealing the vital role of ExG in the composite. Thus, S4 exhibits a maximum power density of 2933.33 W/kg, which is 1.92 and 10.32 times higher than the highest power density of S5 and S2, respectively. Although there is not a clear trend in energy density curves of different samples, S5 shows the highest energy density for almost the whole range of the current

density (Figure 4.11b). For example, at a discharge current of 100 mA, the power densities of S4, S5, S6, S7 and S2 are 1377.80, 1016.40, 827.50, 514.74, and 238.18 W/kg, respectively; and their corresponding energy densities are 3.60, 7.27, 5.15, 2.74, and 0.74 Wh/kg. It is seen that S2 demonstrates a high energy density in a very low current density, which drops rapidly with increasing the current density (Figure 4.11b). In spite of showing a high capacitance, S2 exhibits a poor rate capability, highest resistance, and lowest power density due to the absence of ExG in its composition. S4, with the highest amount of ExG, exhibits the lowest resistance and highest power density, but the lowest capacitance. Overall, it is implied from Figure 4.9a-d that S5 demonstrates the best performance in terms of rate capability, resistance, power density and energy density among samples with less ExG, i.e. S2, S6, and S7. In one hand, decreasing the ratio of ExG/aniline less than that of S5 results in inferior performance in power density, energy density, and rate capability. On the other hand, with an increase in the ratio of ExG/aniline more than that of S5, the power density is increased and the energy density is decreased. Consequently, the weight ratio of ExG/aniline can be selected more than that of S5 (0.65) to attain a higher power density, with a sacrifice in the energy density, for applications requiring high power density. In other words, the optimum preparation weight ratio of ExG/aniline can be between 0.65 to 0.76 depending on an acquired power and energy density.

To study the cycling performance of S2, S5, and S6, 2000 cycles of GCD are run at 0.05 A and the variations of the percentage of power density and energy density versus cycle number are illustrated in Figure 4.12a and b, respectively. Although the cycling stability of capacitance is usually used as a measurement of the cycling performance of SCs, we exploit

a more practical criterion, i.e. the investigation of cycling performance of power and energy densities.

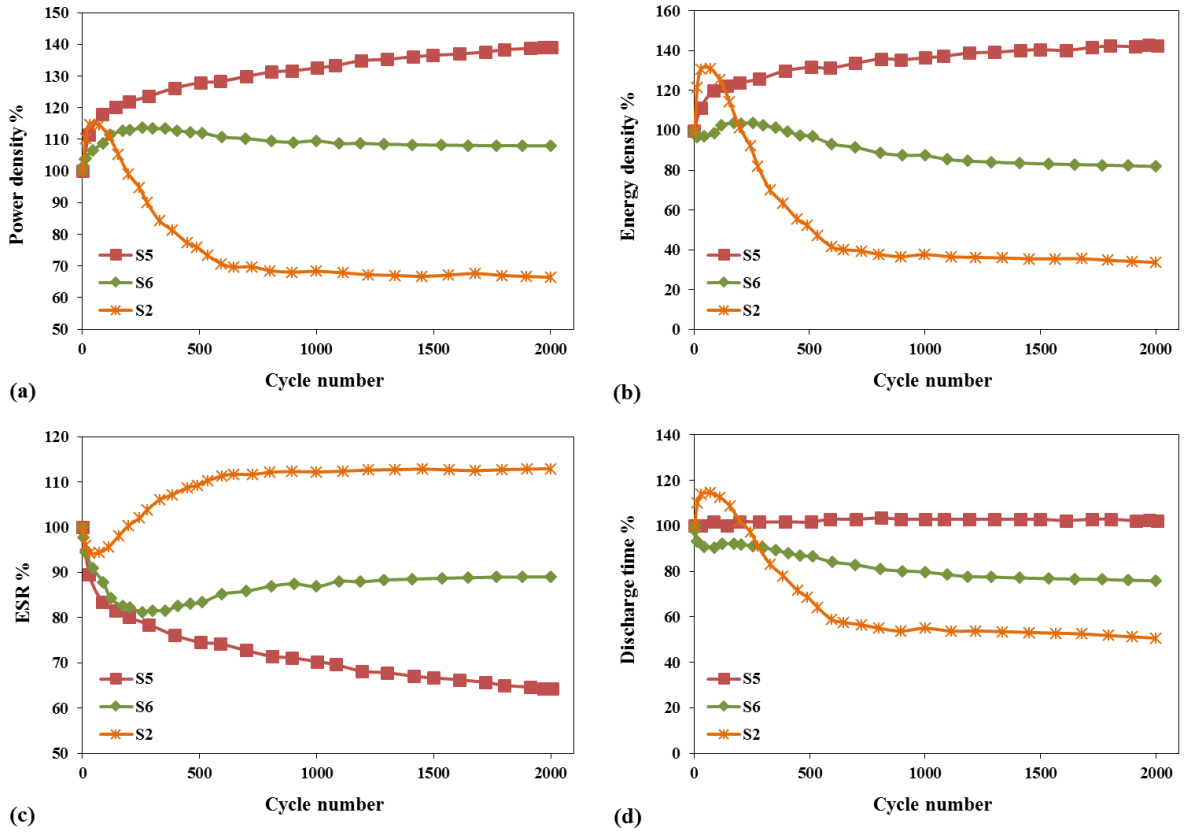

Figure 4.12. Cycling performance of three samples for 2000 cycles of GCD at 0.05 A; (a) power density versus cycle, (b) energy density versus cycle, (c) ESR versus cycle, (d) discharge time versus cycle.

As expected, S5 exhibits an exceptional cycling behavior compared with S2 and S6. Both power and energy densities of S5 increase during first 80 cycles with a sharp slope and then with a small slope afterwards. Such a finding could be explained by the unchanged discharge time (Figure 4.12c) and the decrease in ESR (Figure 4.12d) during the cycling. It is practically important that the discharge time for S5 remains constant for the whole 2000 cycles of GCD. The sharp rise in the power and energy densities during the first 80 cycles of GCD for all three samples could be attributed to the regulation of ion transport to the active sites as well as regulation of redox reactions. Before the initiation of GCD cycling

test, the ions in the aqueous electrolyte are in equilibrium. Once the cycling test starts, it takes some time for the ions to penetrate to the active sites. One can see that the cycling behavior of S6 is better than S2 and worse than S5 highlighting the positive effect of ExG which could be attributed to the combination of PAni and ExG. Power and energy densities of S2 first increase sharply up to 70 cycles and then diminish up to 650 cycles, after which they become unchanged. The relatively poor cycling performance of S2 indicates the importance of an addition of ExG in the composite. Contrary to the continuous degradation of pure PAni with cycling, the decay of power and energy densities of S2 stops after 650 cycles. This can be explained by the contribution of cellulose in improving the cycle life of PAni-coated cellulose composites, possibly since the volume expansion of PAni nanofibers during repetitive doping and de-doping is cushioned by cellulose scaffold. Overall, cycling behavior improves with increasing ExG confirming the above discussion that the optimum weight ratio of ExG/aniline is a value not less than 0.65.

As highlighted in the introduction, PAni provides a source of high pseudocapacitance, while ExG is expected to ensure a good rate capability, cycling stability and high power density at a large current in addition to double-layer charge storage. Figure 4.12 imply that improving the cycling stability, rate capability, power density, and conductivity of the composite film is associated with increasing ExG/aniline weight ratio.

The remarkable electrochemical properties of the designed electrode are found to be mainly owing to an effective combination of PAni with ExG and silver in a cushiony cellulose matrix. The high flexibility and high mass-loading of the composite electrode is attributed to the utilization of the cellulose scaffold that binds the composite elements together. In addition to the porosity of the composite structure, the cellulose fibers in the

composite electrode largely increase the absorption of aqueous electrolyte by the film in an assembled SC leading to superior electrochemical performance.

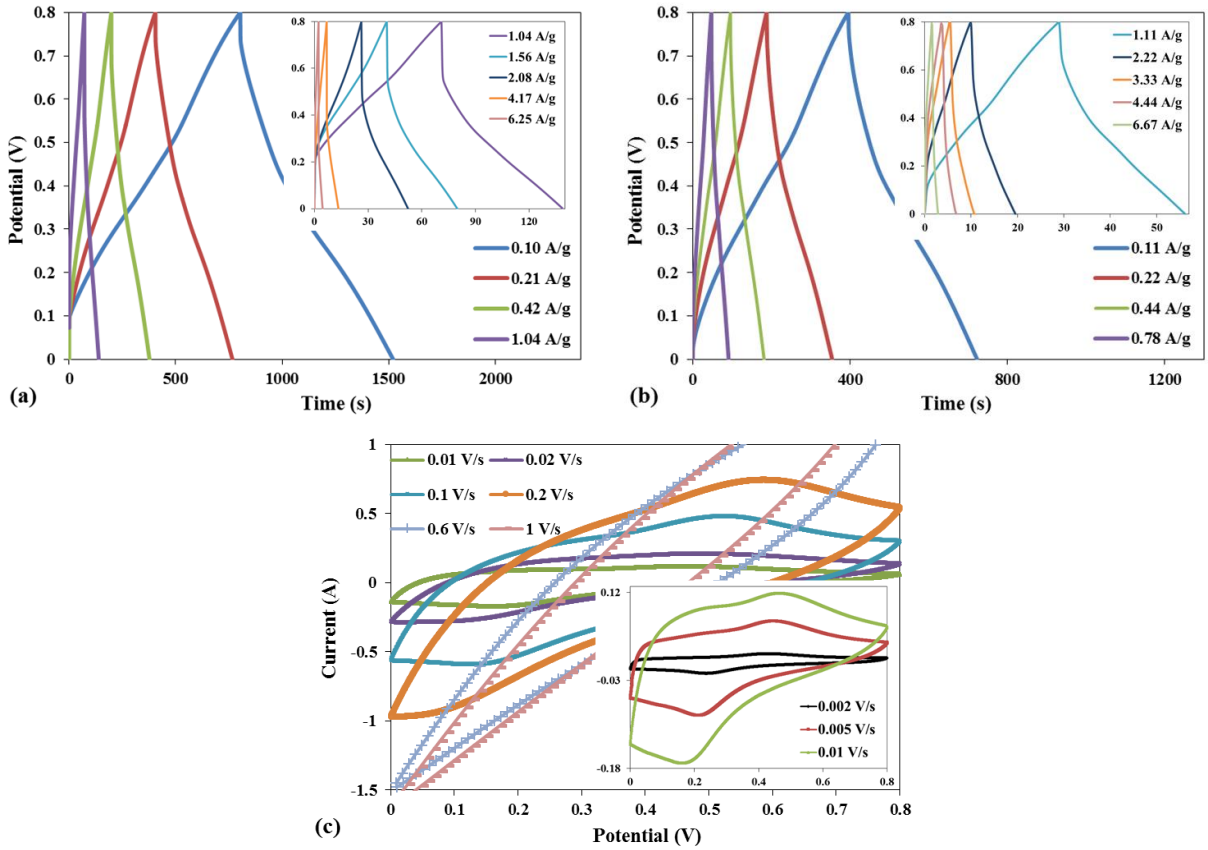

Figure 4.13. (a) GCD curves of S5 for different current densities, (b) GCD curves of S4 for different current densities, (c) CV curves of S5 for different scan rates.

The GCD curves for different current densities and CV curves for different scan rates are plotted in Figure 4.13a and c, respectively, to further illustrate the electrochemical behavior of the SC fabricated from S5. In addition, the GCD curves of the SC fabricated from S4 is provided in Figure 4.13b for comparison. It is seen from Figure 4.13a that the discharge curves deviate from a straight line due to the presence of PAni and experience a larger potential drop for a higher current density, as expected. The reduction and oxidation peaks of PAni are readily observed in the CV curves. The oxidation peak for 2 mV/s happens at 0.42 V and it moves to the right with increasing the scan rate. The reduction

peak for 2 mV/s happens at 0.24 V and it moves to the left with increasing the scan rate. It is worth mentioning that no reduction and oxidation peak is observed when the device is charge/discharges with a high scan rate, e.g. 1 V/s, since there is limited time for redox reactions to happen in PAni.

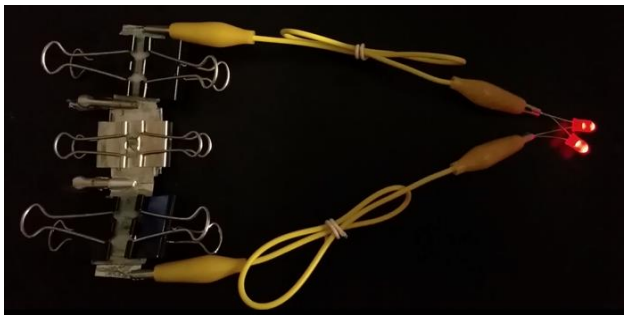

Figure 4.14. Photograph of two red LEDs lit by three fabricated SCs in series.

To show the practical feasibility of the work, the photograph of two red LEDs lit up by three charged SCs in series is provided in Figure 4.14 (also see video #1). It can be seen in the video#1 that the two LEDs glittered very brightly the moment they were connected to the SCs, showing the fast discharge and high power density of the SCs in contrast to batteries [47].

4.5 Conclusion

In summary, a low-cost high-performance SC has been developed based on a flexible film of PAni, cellulose, ExG and AgNPs. Through an optimization process for selecting each component quantity in the composite electrode material, a SC with outstanding electrochemical performances is achieved. Adjusting the ratio of ExG/aniline in the composite is crucial in attaining an enhanced capacitance, high conductivity, rate capability and cycling stability of the SC. Furthermore, tuning the ratio of $AgNO_3$/aniline is vital in enhancing the conductivity of the composite electrode. The findings show that the optimum

weight ratio of $AgNO_3$/aniline and ExG/aniline in the composite are estimated to be 0.18 and 0.65, respectively. The ratio of ExG/aniline can be selected higher than 0.65 to acquire a desired power density for applications requiring high power rather than energy density. The ultrahigh areal capacitance, excellent cycling behaviour, enhanced rate capability as well as simple preparation process of the flexible composite electrode make it greatly surpass the current commercial SCs while having potential application in wearable electronics.

In the next chapter, another approach to design a flexible PAni-based electrode will be introduced. The main focus will be improving the cycling stability of PAni-based electrodes by using a cushiony support for PAni nanostructure.

Chapter 5:

Polyaniline Nanoflowers Grown on Vibration-Isolator-Mimetic Polyurethane Nanofibers for Flexible Supercapacitors with Prolonged Cycle Life

5.1 Abstract

The brittle nature and poor cycling stability of polyaniline hinder its practical applications as a freestanding electrode for supercapacitors. It is expected that the stress induced by repeated volume change of polyaniline during cycling is alleviated using polyurethane nanofibers as polyaniline support mimicking mechanical vibration isolators. A flexible electrode for supercapacitors with remarkable cycling stability is developed by using CNT-reinforced electrospun polyurethane as a cushiony support for deposition of polyaniline. The *in situ* polymerization of aniline is controlled such that flower-like polyaniline is grown on individual polyurethane nanofibers resulting in a porous membrane with high surface area and adjustable mass-loading of polyaniline by repeating the coating process. In contrast to the continuous degradation of pure polyaniline electrodeposited on carbon cloth, the current design exhibits an excellent capacitance retention of 93% after 10000 cycles of charge-discharge. Moreover, after an initial increase of ~13% and ~18% in power density and energy density during the transient phase of cycling, very slight variations in parameters are observed, which could be attributed to the regulation of ion diffusion to the active sites of electrode materials. The cushiony effect of polyurethane and the strong affinity between

grown polyaniline and polyurethane nanofibers as well as buffer spaces between nanofibers, which accommodate the volume expansion of polyaniline nanoflowers, all lead to the structural stability of polyaniline during cycling. The facile strategy to attain a stable and flexible polymer electrode could open up new opportunities for flexible and wearable pseudocapacitors.

5.2 Introduction

The market demand for personal electronics as well as wearable electronics has promoted the development of flexible and lightweight SCs with high capacitive performance. As vital components of a flexible SC, electrodes play an important role in the overall performance of the device. Therefore, electrode materials are required to have sufficient mechanical robustness intrinsically or with an assist of another component. One approach to construct a freestanding electrode is using a flexible support for active materials based on conductive carbon materials or nonconductive polymer supports and textiles. For example, much effort has been dedicated to develop electrodes by coating active materials on natural or synthetic nonconductive fibers as supports owing to their excellent flexibility, low-cost and large-scale production [11, 98-101].

Polyaniline (PAni) is a popular pseudocapacitive conductive polymer for electrodes of SCs owing to its low cost, ease of synthesis, environmental stability, controllable electrical conductivity, high specific capacitance, and high doping level [13, 102-103]. However, pure PAni is a brittle material and it is impossible to produce a PAni film mechanically robust enough to be freestanding. Choosing a suitable freestanding and nonconductive support, such as polyurethane (PU), for PAni could be an effective approach to address this drawback. PU

is an inexpensive, resilient, flexible and durable polymer that has an extremely wide range of applications such as building and construction, appliances, bedding, packaging, coatings, textiles, and automotive manufacturing. Flexible films produced by blending PU and PAni [104] are not suitable for SC applications due to the low conductivity and no porosity of such films. Likewise, PU foams and textiles still suffer from low porosity and specific surface area which makes them unfit as a substrate for PAni coating. Electrospinning is an efficient and simple technique for the fabrication of flexible polymer nanofibers with characteristics of having high specific surface area and being lightweight and flexible [105-107]. For instance, graphite nano-platelet were coated on electrospun PU nanofibers to fabricate flexible and conductive composite films [108]. In another work, reduced graphene oxide (RGO) and silver nanoparticle were coated on electrospun PU nanofibers to produce flexible composites with enhanced electrical conductivity [109]. Thus, it would be feasible to develop electrodes of SC by coating active materials on electrospun PU. In a number of studies [110-112], polymer nanofibrous films were reinforced by CNT fillers oriented along the axes of the nanofibers through electrospinning a CNT-polymer mixture. During the electrospinning process, CNTs orient along the streamlines of the electrospinning solution due to elongation of the fluid jet; resulting in a tube-in-fiber structure with CNTs aligned in the polymer nanofibers. For instance, Sen et al. [112] incorporated CNTs into PU to enhance the mechanical properties of the electrospun composite nanofibers. They indicated that CNT-reinforced PU membranes show a larger tensile strength compared to the pure PU membrane, which is attributed to the efficient load transfer to the CNTs along the axis of an individual fiber in the composite. It is implied that the orientation of CNTs along the axis of an individual PU nanofiber

increases the longitudinal stiffness of the nanofiber while barely affecting its radial stiffness (or the cushiony effect of an individual PU fiber along the transverse directions).

Another drawback of PAni is its poor cycling stability in aqueous electrolytes resulted from repeated volumetric swelling and shrinking caused by insertion/de-insertion of counterions during the charge-discharge cycles [26]. The repeated volume change of PAni leads to structural instability and undesirable changes to the morphology of PAni, thereby reducing the capacitive performance over cycling. The poor cycle life of PAni hinders its practical application as a pseudocapacitor although it exhibits substantially larger capacitance than electrical double-layer SCs. A popular method to improve the cycling stability of PAni is developing composite electrode materials by depositing PAni on carbonous nanomaterials [12-13, 94, 113]. For example, Zhang et al. [46] electrodeposited PAni on vertically aligned CNTs as a composite electrode of SC with 95% capacity retention after 5000 charge-discharge cycles at a current of 10 mA in 1 M H_2SO_4 electrolyte. A fabricated composite of PAni and graphene nanoribbons had a stable cycling performance with 90% capacitance retention after 4200 charge-discharge cycles at a current density of 1 A/g [58]. A 3D-RGO/PAni composite film was fabricated with 88% capacitance retention after 5000 charge-discharge cycles at a current density of 5 A/g [55]. The good cycling life of such composite electrode materials is likely attributed to the good adhesion of PAni to surface of carbonous nanostructures through the interactions including π-π stacking, electrostatic interactions, and hydrogen bonding [114], which is only effective for extremely low mass-loading of PAni. In another approach, the cycling stability of PAni and polypyrrole (PPy) electrodes was enhanced by hydrothermal deposition of a thin carbonaceous shell onto their surface as a protective layer [115]. The carbonaceous shell-coated PAni and PPy electrodes

exhibited 95% and 85% capacitance retention after 10000 cycles at a scan rate of 100 mV/s in 1 M H_2SO_4 electrolyte. In another interesting approach, Pan et al. [69] developed phytic acid-crosslinked PAni hydrogels with porous 3D nanostructures that showed ~83% capacitance retention after 10000 cycle at a current density of 5 A/g. The good cycling performance PAni hydrogel coated on a carbon cloth was explained by phytic acid crosslinking of PAni that can accommodate volume change of PAni during cycling. Since each phytic acid molecule is able to dope several PAni chains, an interconnected microstructures of PAni is formed. However, such an interaction between phytic acid and PAni chain is not strong enough, and consequently would readily be disbanded in aqueous acidic electrolytes during electrochemical tests. Due to this limitation, the conductive hydrogel is mechanically weak making it difficult to construct a freestanding film without the usage of a substrate. In addition, to attain an acceptable cycling stability in an aqueous electrolyte, a minute mass-loading of the PAni hydrogel on the carbon paper cloth should be used to keep an effective adhesion to the substrate. Song et al. [116] improved the cycling stability of PPy by electrochemically depositing PPy on a partial-exfoliated graphite (PExG) substrate. They claimed that growing PPy on a substrate/current collector with a mechanically flexible nature such as reduced RGO, CNTs, and PExG accommodate large volume change of PPy during charge-discharge, and thus suppress structural pulverization of PPy [116]. However, it is evident that such substrates with a large elastic modulus are not able to mitigate this nano-level stress induced by volume change of PPy. A simple analogy is that one would employ a cushiony material for packaging rather than a rigid or stiff material to prevent a possible damage in case of a drop or an impact. An ideal cushion requires a low stiffness as well as an energy dissipation mean (damping). The key point here

is that the flexibility or resilience in nano scale should be distinguished from the flexibility of a film in macro level. For instance, a carbon fiber paper is flexible but not in nano scale due to a large elastic modulus of carbon fiber, i.e. 200-500 GPa. On the other hand, PU with a low and an adjustable elastic modulus (typically from 3 to 2000 MPa) and the ability to dissipate energy (viscosity) could be a great candidate among polymers as a cushiony substrate. According to the evidences perceived from the study [116], the enhanced cycling stability is likely owing to strong adhesion between a very thin layer of deposited PPy and the PExG substrate. Therefore, in addition to a firm connection between the conducting polymer and the substrate, selection of a cushiony substrate is vital to accommodate stress induced by repeated volume changes, and thus attain a better cycling stability.

According to the above discussions, it is vital to develop a strategy to improve the cycling stability of PAni. Here, with an analogy with mechanical vibration isolators, we hypothesize that using electrospun CNT-reinforced PU nanofibrous membrane as a cushiony support for deposition of flower-like PAni would greatly improve the cycling stability of PAni as a binder-free electrode for flexible SCs. The current strategy improves the cycling performance of PAni through combination of three following features. Similar to a vibration isolator, the low elastic modulus (analogous to a spring with a low stiffness) combined with the inherent damping effect of an individual PU nanofiber hinders the stress induced by repeated volume changes of PAni grown on it, and thus prevents the structural breakdown and undesirable changes to the morphology of PAni. Moreover, buffer spaces between electrospun PU nanofibers accommodate the volume expansion of PAni grown on individual PU nanofibers. Lastly, the strong affinity between grown PAni nanoflowers and PU nanofibers impedes PAni detachment, resulting in an enhanced structural stability.

Notably, inexpensive and environmental friendly PU nanofibers are more durable and chemically stable compared to cellulose-based textiles in acidic electrolytes owing to the hydrophobic nature of PU. Above-mentioned features along with the large-scale productibility of electrospun PU make it a fit candidate as a flexible support for the deposition of PAni as well as other redox-active conducting polymers and metal oxides. Utilization of the electrospun PU/CNT mat ensures high porosity and surface area of the resulting nanostructure after PAni coating and prevents formation of bulk PAni. Besides, the high flexibility of the membrane is maintained after decoration of the flower-like PAni nanostructure on the surface of nanofibers. The simple preparation process of this binder-free and flexible electrode includes electrospinning a solution of PU/CNT followed by multiple PAni coating by a controlled *in situ* polymerization of aniline.

5.3 Experimental Methods

5.3.1 Preparation of PU/CNT Nanofiber

80 mg of CNTs (MWCNTs, length: 10-30microm, 90% purity, conductivity>100 s/cm; Boyu Gaoke New Material Technology Co., Ltd) is dispersed in 10 mL dimethylformamide (DMF) using a probe sonicator (SK92-IIN, NingBo Scientz Biotechnology Co., Ltd.) at 300 W for 10 min (5s on and 1s off in an ice bath), followed by sonicating in an ultrasonic cleaner (VWR International, LLC.) at 100 W for 30 min. Thermoplastic PU elastomer is used in this study (SK Chemicals SKYTHANE® S180A; Shore hardness 84 (ASTM D224 type A), resilience 48 (ASTM D2632, vertical rebound), ultimate tensile strength 34.3 MPa (ASTM D412), elongation at break 700% (ASTM D412), and 100% modulus 5.1 MPa (ASTM D412)). Then 1 g of PU (100 mg/mL) is dissolved in the DMF/CNT dispersion

under magnetic stirring at the ambient temperature for 12 hours to obtain a homogeneous solution. The DMF/CNT/PU dispersion is directly used in the electrospinning process to make the PU/CNT nanofibrous membrane. Briefly, 10 mL of the solution is loaded into a syringe fitted to a syringe pump (PHD2000 Harvard apparatus, Instech Laboratories, Inc.). The positive lead of a high voltage DC power supply (High Voltage Research, GAMMA) is connected to the syringe needle and the ground connection is attached to a stainless-steel mesh (10 cm×10 cm) placed 12 cm from the needle tip for collecting fibers. The discharge rate of the syringe pump is set to 3 mL/h, and a voltage of 17 kV is applied once the first drop appears at the needle tip. The thickness of the electrospun membrane is between 100 to 150 nm.

5.3.2 Preparation of PU/CNT/PAni Film

PU/CNT mat is immersed for 2 hours in a solution of 0.15 mL aniline (≥99.5%, Sigma-Aldrich) dissolved in 70 mL of 0.5 M sulfuric acid (98%, Anachemia) that contains 5 mL ethanol (Sigma-Aldrich) to enhance the wettability of the membrane. Then, another solution containing 0.125 g of ammonium persulfate (APS, ≥98.0%, Sigma-Aldrich) in 10 mL of deionized water is added to the former solution at room temperature. Both solutions are kept in 4 ºC before mixing. After reaction for 2 hours, the PAni-coated PU/CNT membrane is removed and washed with deionized water, followed by drying between two plastic sheets at the ambient temperature. Likewise, subsequent coatings are carried out to increase the mass-loading of PAni. The weight of the PAni coated on the membrane after each coating is calculated by the difference in the dried weight of samples before and after a coating

process. The mass-loading of PAni for the films with two and three coats of PAni are around 17.8 wt% (0.95 mg/cm^2) and 25.8 wt% (1.52 mg/cm^2), respectively.

5.3.3 Characterization

The surface morphology of films is observed using a scanning electron microscope (SEM; JEOL JSM-5900LV, SEMTech Solution, USA), a scanning auger microprobe (JEOL JAMP-9500F, SEMTech Solution, USA), and a high resolution SEM (Nova NanoSEM 450, FEI, USA). A sample of PU/CNT membrane is gold coated before performing SEM. Fourier transformed infrared (FTIR) spectra are studied using Thermo Nicolet iS10 FTIR Spectrometer.

5.3.4 Electrochemical Measurements

To carry out the electrochemical tests as assembled SCs, two identical PU/CNT/PAni strips are assembled in a symmetric SC [28]. Two rectangular electrodes are directly cut from the PU/CNT/PAni films (2 cm×1.5 cm) and are soaked in 1 M sulfuric acid for 5 hours. Two stainless-steel foils are used as the current collectors and a strip of filter paper (Whatman, grade 5) wetted with 1 M sulfuric acid is used as the separator. Then, the two electrodes, separated by the filter paper and sandwiched between the current collectors, are assembled into a layered structure and sealed with a parafilm to prevent water evaporation.

The electrochemical experiments of assembled SCs are conducted using an electrochemical workstation (CS350, CorrTest Instruments Inc., China). The GCD tests are run from 0 to 0.8 V at a constant current ranging from 5 to 125 mA. The EIS measurements are carried out over a frequency range from 10^5 to 0.01 Hz at an AC amplitude of 10 mV

and zero DC amplitude. The CV tests are recoded from 0 to 0.8 V at a constant scan rate ranging from 0.001 to 0.4 V/s.

The capacitance of an assembled SC device is calculated from the discharge slope of GCD curve after an initial potential drop based on $C = I\Delta t/(\Delta V - V_{IR})$, where I is the discharge current, Δt is the time for a full discharge, ΔV represents the potential window or the potential change after a full discharge, and V_{IR} is the potential drop at the initial discharge stage. The energy density (E) and power density (P) for an assembled device are estimated by $E = 0.5C(\Delta V - V_{IR})^2 = 0.5I(\Delta V - V_{IR})\Delta t$ and $P = E/\Delta t$, respectively. The ESR of a SC device is calculated by $ESR = V_{IR}/I$. Specific capacitance, energy density, and power density per mass are determined by dividing C, E, and P by m, where m is the total mass of PAni on both electrodes. Areal specific capacitance, energy density, and power density are calculated by dividing C, E, and P by A, where A is the geometric area of the SC device (3 cm^2 herein). Current density is also defined as I/m or I/A. The mass specific capacitance for only one electrode of a SC device is determined by dividing $2C$ by the mass of PAni on one electrode. The three-electrode system experiments are conducted in 1 M sulfuric acid using a stainless steel foil as the counter electrode and the saturated calomel electrode (SCE) as the reference electrode. A PU/CNT/PAni film with three coats of PAni is used as the working electrode (2cm×1.5cm). The mass-specific capacitance for a three-electrode system is calculated from the discharge slope of GCD curve and is given by $I\Delta t/m'(\Delta V - V_{IR})$, where m' is the mass of PAni coated on the working electrode.

5.3.5 Characterization of Mechanical Properties

To investigate the mechanical properties of nanofibrous membranes, tensile tests are conducted at room temperature with a material testing machine (LS5, AMETEK, Inc., USA) with a 250 N load cell. Membranes (9 mm wide) are fixed by the grips and subjected to an extension rate of 1 mm/min using a gauge length of 20 mm.

To examine the nano-mechanical properties of the PU and PU/CNT membranes, quasi-static nanoindentation experiments are carried out at room temperature using a calibrated nano-mechanical testing machine (Ti 750M UBI, Hysitron, Inc., USA) with a Berkovich indenter tip. The samples are mounted onto the substrate using a double-sided adhesive tape and totally 8 points are tested for each specimen. The maximum load is set to 20 μN with a loading rate of 4 μN/s. After loading to 20 μN, the load is held constant for 2 s to account for creep effects before unloading the indenter.

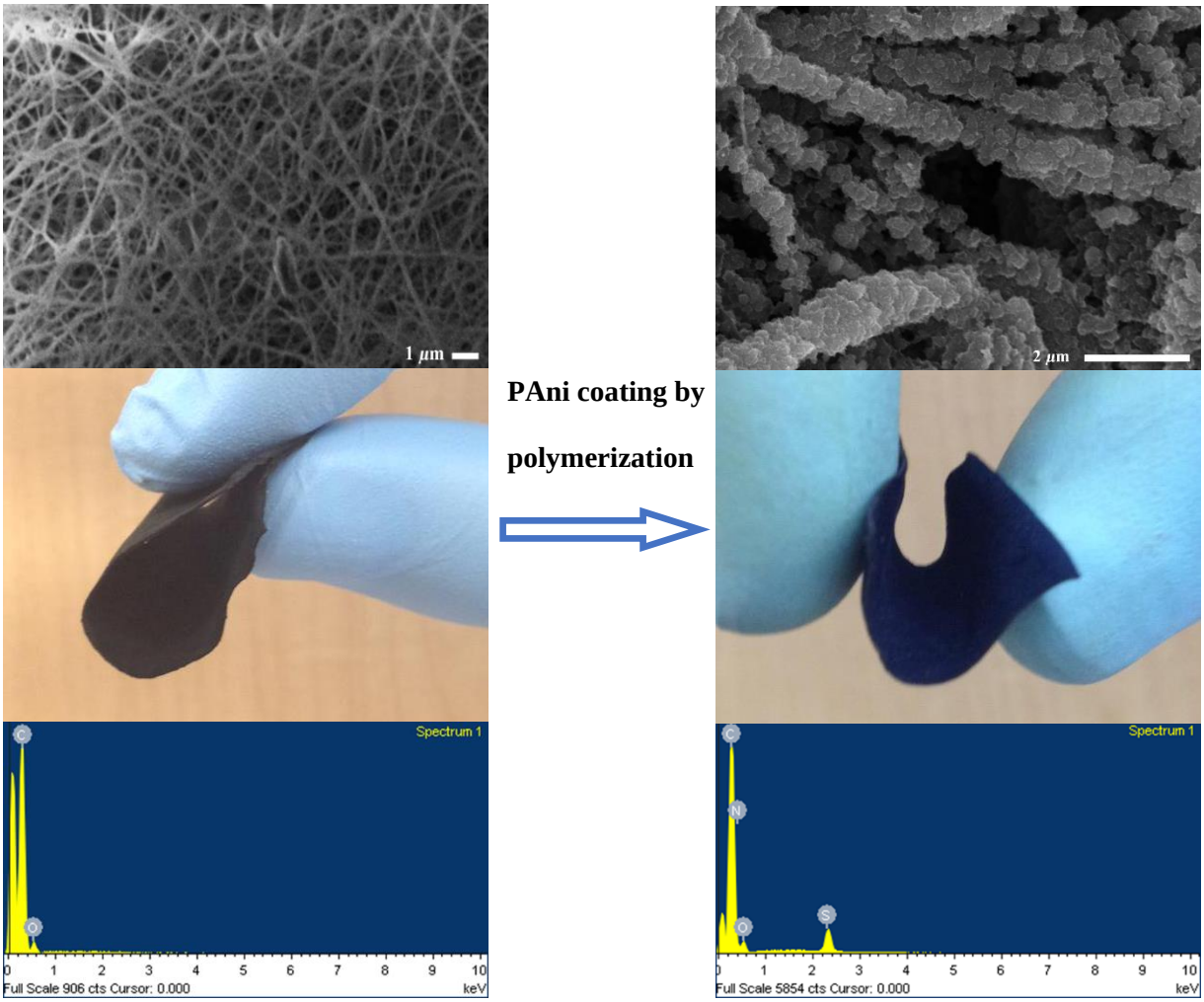

(a) PU/CNT **(b) PU/CNT/PAni**

Figure 5.1. SEM images, photographs and EDS spectra of (a) PU/CNT and (b) PU/CNT/PAni with three coats of PAni.

5.4 Results and Discussion

SEM images, photographs and EDS spectra of PU/CNT and PU/CNT/PAni with three coats of PAni are shown in Figure 5.1a and b, respectively. The dark color of PU/CNT nanofibrous mat demonstrates the successful incorporation of CNT into the PU matrix. In addition, the protruded parts of those CNTs that are not embedded within PU nanofibers, noticed with

bright colors and mean diameter of 50 nm, can be observed in SEM images of gold-coated PU/CNT membrane (Figure 5.2).

It is also seen that PAni is successfully coated on PU/CNT nanofibers while maintaining its high flexibility. The highly flexible PU backbone facilitates the flexibility of the membrane making it suitable for wearable electronic applications. According to the EDS spectrums of gold-coated PU/CNT and PU/CNT/PAni, the PAni-coated film shows the peaks of elements N, O, and S in addition to the peaks of elements C and O, which confirms the existence of PAni. By analyzing several SEM images of PU/CNT films, the average diameter of PU/CNT nanofibers is found to be approximately 135 nm and ranging from 60 nm to 290 nm (Figure 5.3). The fiber diameter, specific surface area, and porosity parameters depend on electrospinning parameters as well as the concentration of PU solution [117]. Therefore, the electrospinning parameters can be optimized to achieve higher surface area and porosity, and thus enhancing the capacitive performance of the PAni-coated film.

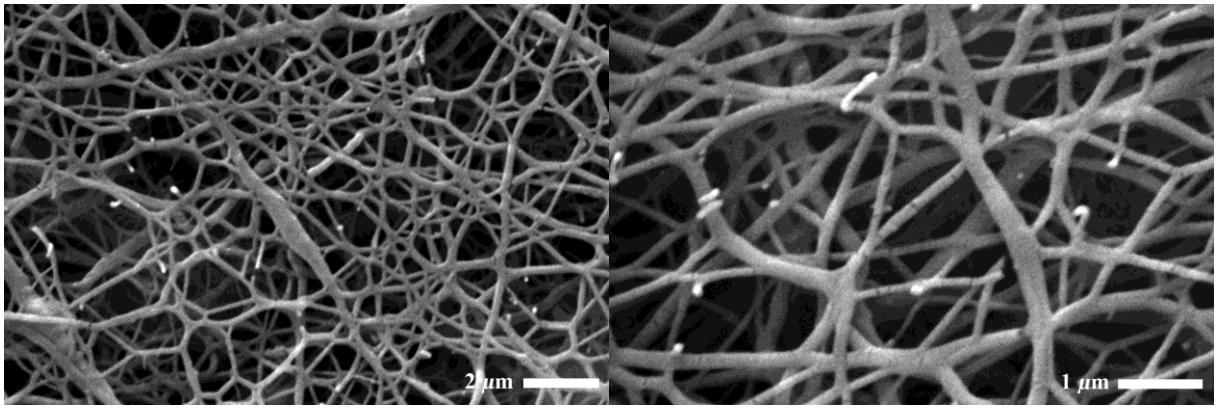

Figure 5.2. SEM images of gold coated PU/CNT film.

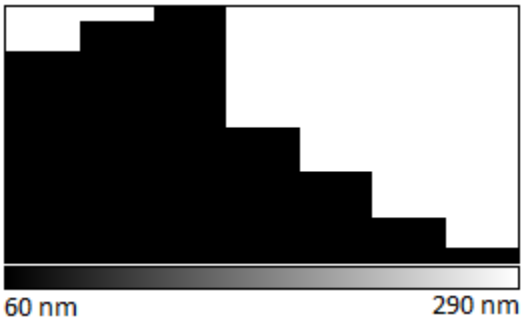

Figure 5.3. Diameter distribution of PU/CNT nanofibers obtained from analysing SEM images.

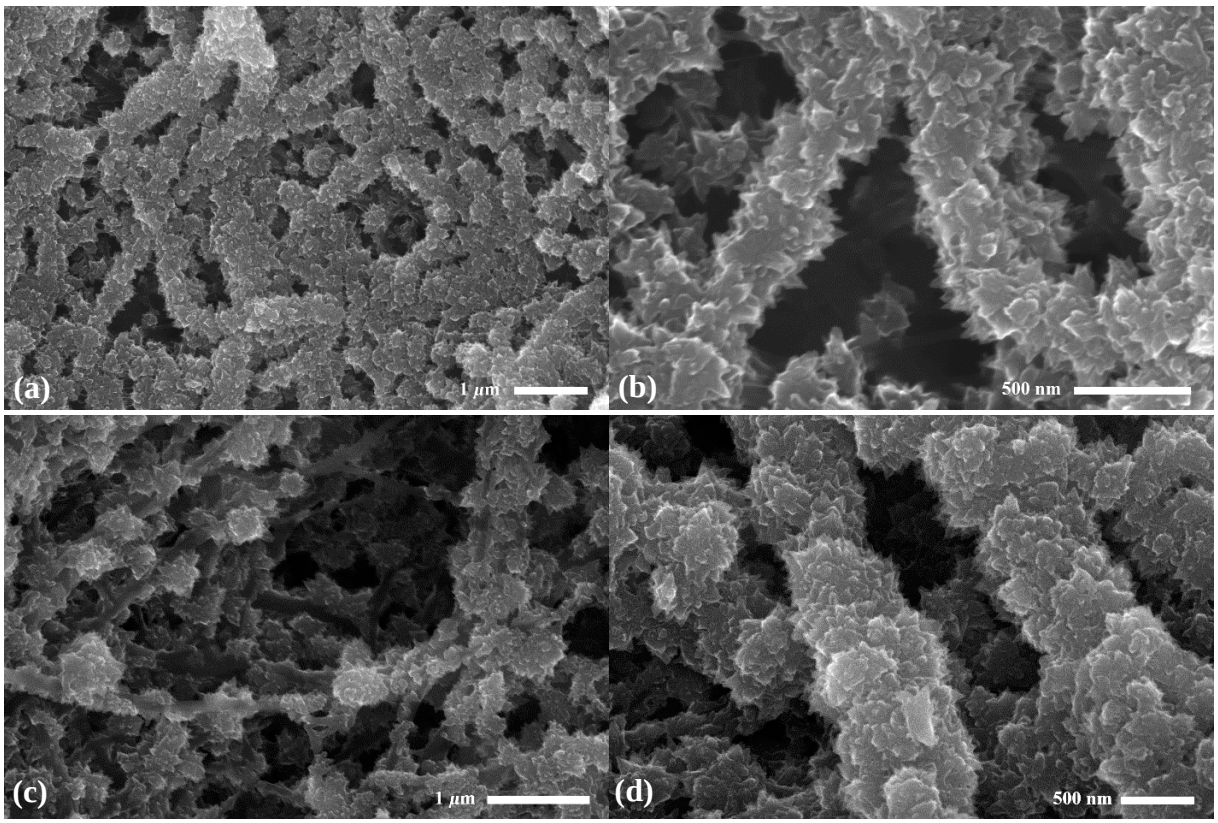

Figure 5.4. SEM images of PU/CNT/PAni films, (a-c) with two coats of PAni and (d) with three coats of PAni.

SEM images of PU/CNT/PAni in Figure 5.4 confirm the effective growth of flower-like PAni nanostructures on the nanofibers as well as high porosity of the membranes. SEM image of the film with two coats of PAni in Figure 5.4c, taken from a less-coated spot in the film, shows that the decoration of flower-like PAni on nanofibers is similar to the growth of leaves on a branch. The mechanism of decoration of flower-like PAni on nanofibers can

be ascribed as follows. Upon immersing the PU/CNT nanofibrous mat in the diluted aqueous solution of aniline, aniline monomers absorb on several tiny spots of individual nanofibers through hydrogen bonding between carbonyl groups of PU and aniline. PU is soluble in aniline so that PU nanofibers are stained readily by aniline monomers on several spots. Upon the initiation of the *in situ* polymerization of aniline, PAni chains nucleate from those spots on the surface of PU nanofibers, and consequently grow into a 3D flower-shaped nanostructure. The SEM image of PU/CNT film coated with PAni for a limited reaction time (20 min instead of 2 hours) clearly shows PAni nucleated from various spots of each nanofiber (Figure 5.5). Therefore, PAni nanoflowers are firmly attached on the PU outer surface owing to the initial penetration of PAni into the PU matrix. Such flower-shaped structure of PAni could provide large porosity and highly accessible surface areas that are necessary for high performance electrode materials. SEM images of the film with three coats of PAni in Figure 5.1b and Figure 5.4d show similar morphology to those of two coats of PAni. The morphology and the amount of PAni deposition depend on many factors such as the concentrations of aniline monomer and oxidizer, the duration of the *in situ* polymerization process, and the solution temperature. In order to avoid agglomeration of PAni or formation of bulk PAni on the PU membrane, subsequent coatings are carried out rather than performing one coating process with a higher concentration of aniline. Hence, a fine morphology of PAni can be obtained by using a low concentration of aniline for the *in situ* polymerization process. To prepare films with a higher mass-loading of PAni, the coating process is repeated.

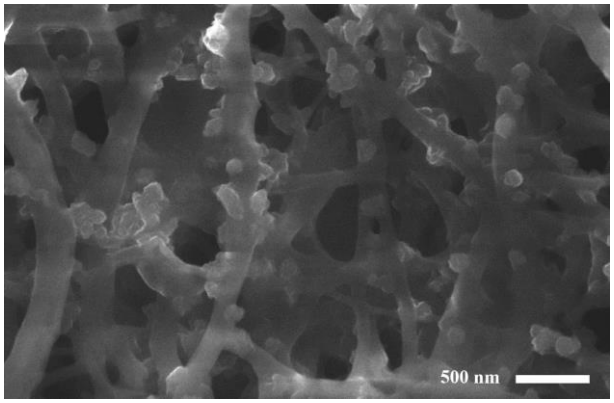

Figure 5.5. SEM image of PU/CNT film coated with PAni after a limited reaction time (20 min), which shows PAni nucleated from various spots of each nanofiber.

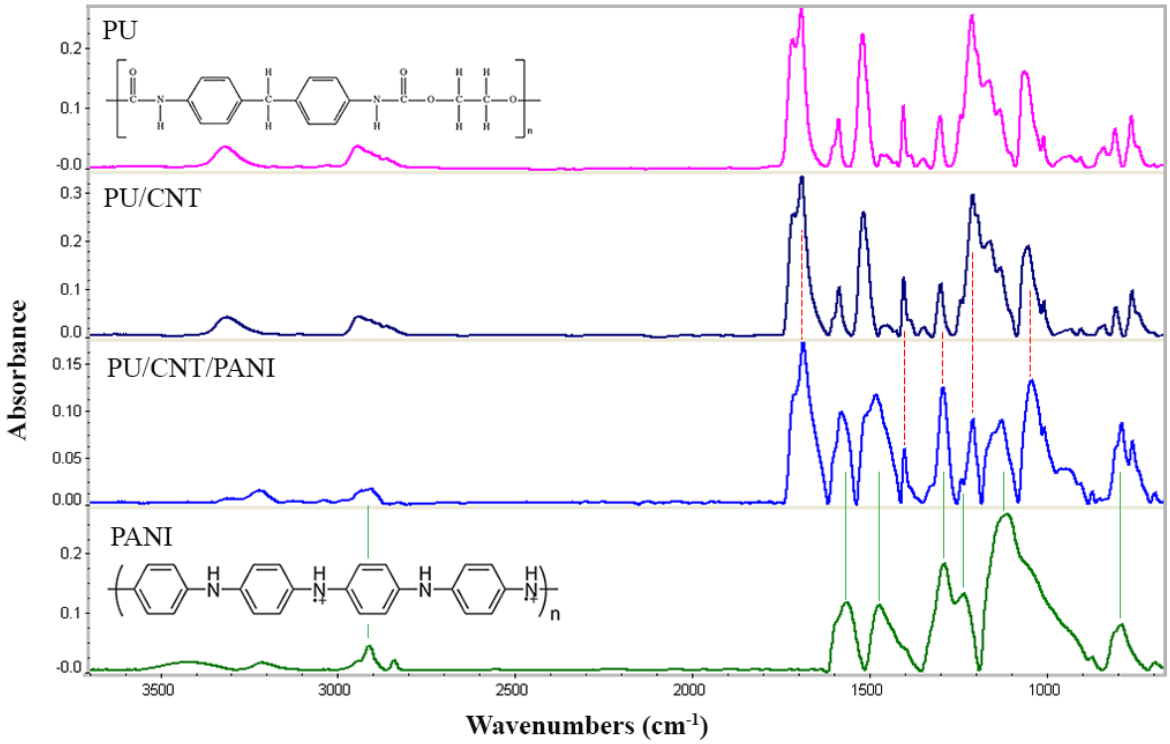

Figure 5.6. FTIR spectra of PU, PU/CNT, PU/CNT/PAni and PAni.

Figure 5.6 shows the FTIR spectra of PU, PU/CNT, PU/CNT/PAni and PAni. The FTIR spectrum of pristine PU fibers gives typical peaks of PU [118-119] at 1074 and 1220 cm^{-1} (C-O-C), 1529 and 1596 cm^{-1} (aromatic C=C), 1701 cm^{-1} (hydrogen-bonded C=O [120-121]), 1727 cm^{-1} (non-bonded C=O [120-121]), 2957 cm^{-1} (CH_2), and 3329 cm^{-1} (N-H), all of which are due to stretching vibrations. The PU and PU/CNT nanofibers show the same FTIR spectrum.

The FTIR spectrum of pure PAni displays typical peaks of PAni [28, 53, 97, 118] at 798 cm^{-1} (aromatic C-H out-of-plane bending), 1123 cm^{-1} (aromatic C-H in-plane bending), 1243 and 1298 cm^{-1} (aromatic amine C-N stretching), 1485 cm^{-1} (benzenoid ring C=C stretching), 1566 cm^{-1} (quinoid ring C=C stretching), and 3437 cm^{-1} (N-H stretching).

The FTIR spectrum of PU/CNT/PAni film shows all the expected characteristic groups of pure PAni, confirming that PAni has been successfully deposited on PU nanofibers. In addition, the FTIR spectrum of PU/CNT/PAni film retains the main absorption peaks of PU, i.e. the peaks correlated with C-O-C and C=O. According to the PU/CNT/PAni spectrum, the shift of N-H stretching peak from those of PU (3329 cm^{-1}) and PAni (3437 cm^{-1}) to a lower wavenumber (3233 cm^{-1}) can be ascribed to the strong incorporation of PAni into PU as well as the formation of hydrogen bonds between carbonyl groups of PU and N-H groups of PAni. The results indicate that PAni is decorated onto the surface of PU membrane through the hydrogen bonding between PAni and PU fibers.

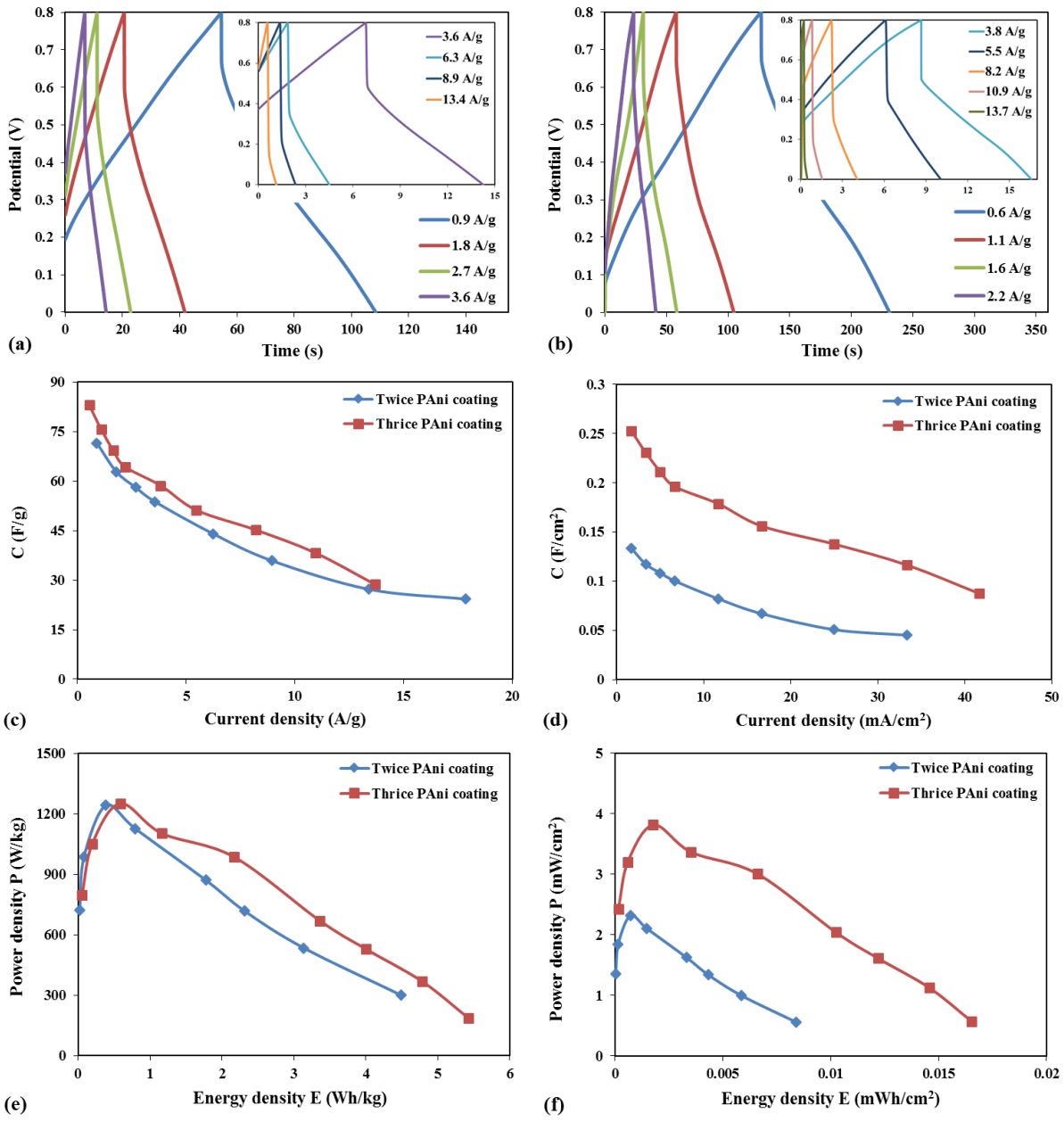

Figure 5.7. The GCD curves of assembled SCs based on PU/CNT/PAni, (a) with two coats of PAni and (b) with three coats of PAni; (c) Mass-specific capacitance versus current density, (d) areal-specific capacitance versus areal current density, (e) power density versus energy density and (f) areal power density versus energy density, for films with two or three coats of PAni.

The electrochemical performance of SCs, assembled in a symmetric two-electrode system, from PU/CNT/PAni films is examined by GCD tests. The two-electrode system used herein is more practical [63, 122-123] because of the fact that only two-electrode cells allow a good estimation of the whole device performance. The GCD curves of assembled SCs on the basis

of films with two and three coats of PAni are plotted at different current densities in Figure 5.7a and b, respectively. The potential drop at the initial discharge stage of a SC (whole device) is mainly attributed to the resistance of both electrodes, both connection resistances, and electrolyte resistance. Therefore, the potential drop of the whole device is larger than that of a single electrode and thus caution should be exercised in comparing different studies. It is seen that the discharge curves with two coats of PAni experience a larger potential drop compared to those with three coats of PAni. Moreover, the potential drops obtained from GCD curves of PAni herein are comparable with those observed in studies [51, 124] with the same test conditions (tests ran from 0 to 0.8V in two-electrode systems in 1 M sulfuric acid). It should be noted that the conductivity of the film after the first PAni coating is inadequate for a SC electrode.

Figure 5.7c and d illustrate the comparison of the mass- and areal-specific capacitances, calculated from GCD tests, between the films with two and three coats of PAni. The corresponding Ragone plots (power density versus energy density at different currents) are provided in Figure 5.7e and f. According to Figure 5.7c and d, the films with two and three coats of PAni shows similar gravimetric performance at a similar current density. However, the film with three coats of PAni exhibits superior areal-specific capacitance, areal energy and power densities owing to higher amount of PAni grafted on PU nanofibers. Generally, at a same current, the film with three coats of PAni shows better electrochemical performance. For instance, the specific capacitances of films with two and three coats of PAni, estimated at a discharge current of 50 mA, are 35.91 F/g (0.07 F/cm^2) and 51.20 F/g (0.16 F/cm^2), respectively. Moreover, at the same discharge current of 50 mA, the power densities of films with two and three coats of PAni are 1243.26 W/kg (2.32 mW/cm^2) and 1104.32 W/kg (3.37 W/cm^2), respectively, and their corresponding energy densities are 0.39

Wh/kg (0.7 μWh/cm^2) and 1.16 Wh/kg (3.5 μWh/cm^2). Therefore, selecting the number of PAni coating depends on the requirement of areal energy and power density.

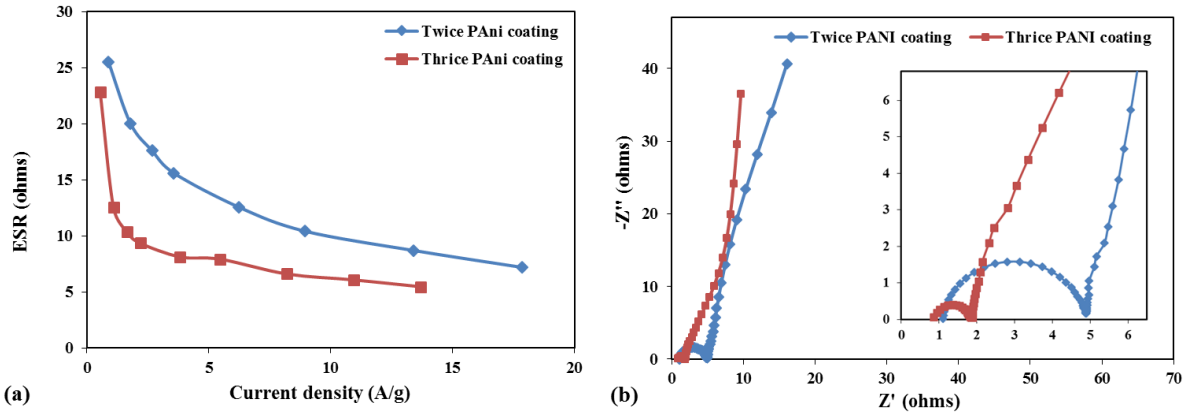

Figure 5.8. (a) ESR versus areal current density obtained from GCD curves of films with two or three coats of PAni, (b) Nyquist plots of SCs based on PU/CNT/PAni for films with two or three coats of PAni.

To further study resistive behavior of the SCs, ESRs are calculated from potential drops of GCD curves for films with two and three coats of PAni and are plotted versus areal current density in Figure 5.8a. In addition, Figure 5.8b depicts Nyquist plots obtained from EIS tests of SCs based on films with two and three coats of PAni. According to Nyquist plots, the equivalent resistance of the assembled SC from the film with three coats of PAni (1.9 ohms) is smaller than the one with two coats of PAni (4.9 ohms). Similarly, the charge-transfer resistances (diameter of semicircles) are found to be 1.1 ohms and 3.7 ohms, respectively. These equivalent resistances are comparable with the resistances of PAni-based SCs in previous studies [28, 125] with a similar test condition (EIS tests in two-electrode systems with 1 M sulfuric acid). Both GCD and EIS tests show that the film with two coats of PAni is more resistive compared to three coats of PAni, thus implying that the sample with three coats of PAni shows better capacitive performance. Although both samples have similar morphology, more PAni nanoflowers are grown on the sample with three coats of PAni leading to a more dense PAni nanostructure in a same area. Hence, the film with three coats of PAni shows lower charge-

transfer resistance as well smaller contact resistance. ESR calculated from GCD curves herein are larger than the equivalent resistances estimated from EIS tests, which is consistent with the notion in the literature [62, 126] that the resistance estimated from EIS test is often much smaller than the one derived from GCD test.

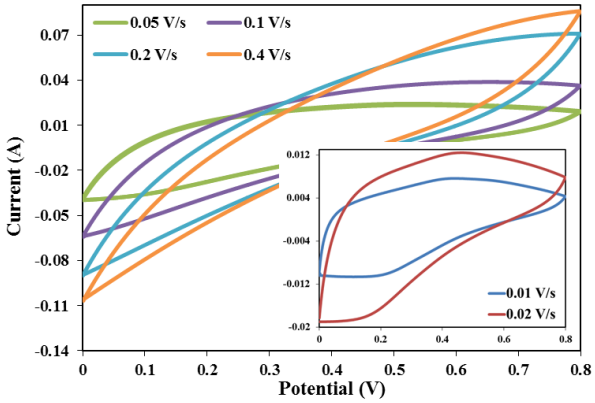

Figure 5.9. CV curves of the SC based on PU/CNT/PAni with three coats of PAni.

To exhibit the voltammetric behavior of the device, cyclic voltammetry (CV) curves of the SC based on the film with three coats of PAni for different scan rates are plotted in Figure 5.9. Since CV tests are conducted in an assembled two-electrode system, the redox peaks are not pronounced in contrast to a three-electrode system [11, 63].

As mentioned earlier, a two-electrode system accounts for the performance of the whole device. To observe the electrochemical performance of a single electrode, we also carried out the three-electrode system tests for PU/CNT/PAni with three coats of PAni (Figure 5.10). It is seen from Figure 5.10b that the mass-specific capacitance of a single electrode obtained from the three-electrode system is larger than those of the two-electrode system, consistent with the literature.[123] According to CV curves in Figure 5.10c, the reduction and oxidation peaks of PAni are more pronounced compared to those in the CV curves of the assembled SC. Moreover, no redox peak is observed in CV curves with a higher scan rate, e.g. 0.4 V/s, because there is limited time for redox reactions to happen in PAni. According to the

Nyquist plot in Figure 5.10d, the equivalent resistance and the charge-transfer resistance are found to be 1.1 ohms and 0.4 ohms, respectively. This equivalent resistance of a single electrode is expectedly smaller than the resistance of the assembled SC (1.9 ohms). In addition, a more straight line in the mid frequency region of the Nyquist plot for the three-electrode system shows a better capacitive performance compared to that of the two-electrode system in Figure 5.8b.

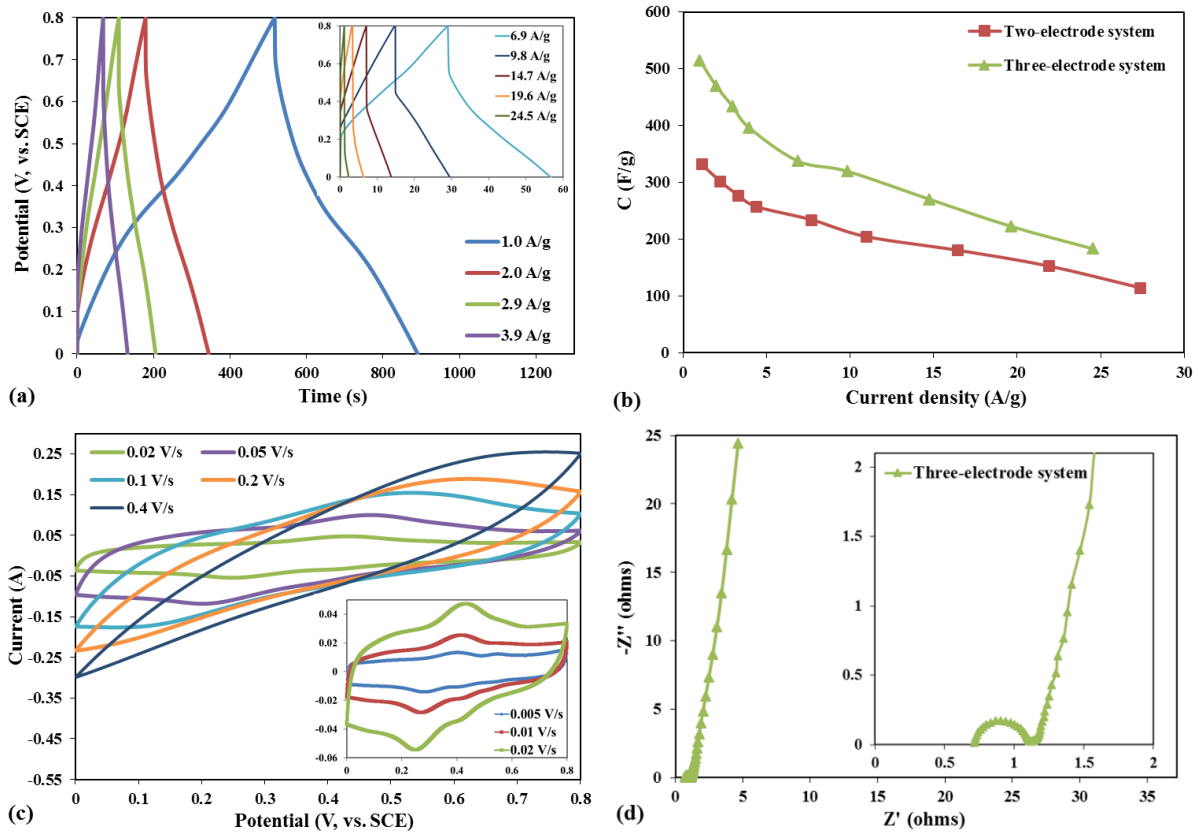

Figure 5.10. The electrochemical capacitance performance of PU/CNT/PAni with three coats of PAni in a three-electrode system. (a) The GCD curves within the potential window 0 to 0.8 V vs. SCE for different current densities. (b) Mass-specific capacitance of a single electrode obtained from GCD curves; the specific capacitance obtained from the two-electrode system is added for comparison (specific capacitance is multiplied by 4 and current density is multiplied by 2 in Figure 5.7c). (c) CV curves within the potential window 0 to 0.8 V vs. SCE at different scan rates; (d) Nyquist plot obtained from the EIS test.

The cycling tests of the fabricated device from PU/CNT/PAni film with three coats of PAni are carried out over 10000 cycles of GCD at 50 mA and the variations of the

percentage of capacitance, power density, energy density, ESR, and discharge time versus cycle number are plotted in Figure 5.11a and b. Although the cycling stability of capacitance is commonly used as a measure of the cycling performance of SCs, we also investigate the cycling performance of power and energy densities because of their high practical significance. The percentage of ESR (which is proportional to potential drop) and discharge time are also given to help understand the cycling behavior. After 10000 cycles of GCD, the percentages of capacitance, power density, energy density, ESR, and discharge time are 93%, 113%, 118%, 86%, and 105%, respectively, relative to the first cycle. Hence, capacitance is slightly decreased while power and energy densities are increased after 10000 cycles. This is explained by the decrease in the potential drop (14% decrease in the ESR), which is in favor of power and energy densities but is unfavorable to the capacitance; and a slight increase (5%) in the discharge time, which is in favor of energy density and capacitance. It is seen from Figure 5.11 that the cycling behavior of the as-fabricated device has two phases—a transient state up to around 500^{th} cycle and a stable state afterward. The initial sharp changes in the percentage of above-mentioned parameters during the transient stage could be attributed to the regulation of ion transport to the active sites of electrode materials and regulation of redox reactions of PAni. After the initiation of GCD cycling test, it takes some time for the ions in the aqueous electrolyte to penetrate into the active sites from an equilibrium state [28]. After the transient phase, very slight variations in parameters during the cycling are observed, which is practically important. It should be noted that the duration of the transient phase depends on the sample and/or type of electrochemical tests conducted on the device beforehand. For instance, CV tests with different scan rates were carried out on this device before the cycling GCD tests. Hence, it takes several cycles

before the active materials adapt to the new experimental condition, particularly those PAni chains that are not in an immediate vicinity of the surface.

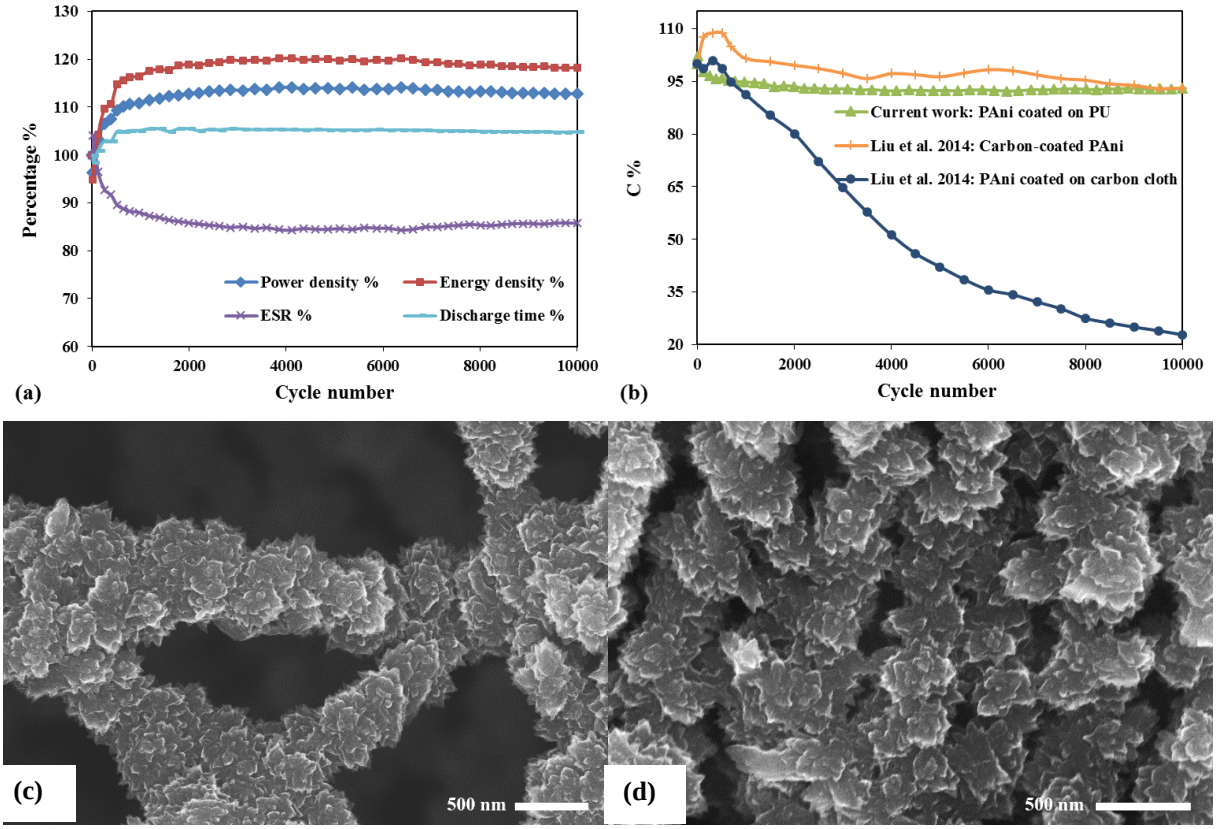

Figure 5.11. Cycling performance of the assembled SC for 10000 cycles of GCD at 50 mA, (a) percentages of power density, energy density, ESR, and discharge time versus cycle, (b) percentage of capacitance versus cycle compared with data from [115]; SEM images of (c) working electrode and (d) counter electrode following 10000 cycles.

SEM images of the working electrode and counter electrode of the fabricated device after 10000 cycles of GCD (Figure 5.11c and d) reveal the unchanged structure of flower-like PAni, and thereby confirming the exceptional cycling stability of the SC.

The excellent capacitance retention of 93% in this study (Figure 5.11b) is comparable with 95% capacitance retention in reference [115] in which a 5 nm protective layer of carbon was hydrothermally deposited onto the surface of PAni nanowires electrodeposited on carbon cloth. Interestingly, an electrode based on bare PAni nanowires electrodeposited on

carbon cloth [115] showed a large capacitance drop after 10000 cycles with 23% capacitance retention (Figure 5.11b). Therefore, it is unlikely that application of a substrate with a large elastic modulus, such as carbon fibers and steel mesh, for deposition of PAni could alleviate the PAni degradation over cycling. The repeated volume change of PAni leads to an initiation of micro cracks and its detachment from the rigid substrate due to the structural instability of the connection. On the contrary, the promising cycling performance and long-term stability of the current device are owing to the utilization of PU-based substrate that cushions the repeated volume change of brittle PAni caused by the insertion/de-insertion of counterions during charge-discharge cycles. PU shows viscoelastic properties, i.e. elasticity and viscosity (energy dissipation or damping effect). The viscoelastic behavior can be described by an elastic spring and a viscous damper (dashpot) connected in parallel (Kelvin-Voigt model) as shown in Figure 5.12. The constitutive equation of this model is expressed by $\sigma(t) = E\varepsilon(t) + \eta\dot{\varepsilon}(t)$, where σ is the stress, ε is the strain, E is the elastic modulus, and η is the viscosity of the material. Meanwhile, a vibration isolator generally consists of a damper connected in parallel to a spring with low stiffness provided that we use the isolator for a cushioning application. Hence, as a viscoelastic substrate for PAni in a core-shell nanostructure, an individual PU nanofiber acts as a vibration isolator owing to its damping and small elastic modulus (low stiffness), mitigating the repeated stress induced by volume expansion or contraction of PAni nanoflowers during cycling (Figure 5.12). Furthermore, buffer spaces between electrospun PU nanofibers accommodate the volume expansion of flower-like PAni grown on the surface of individual PU nanofibers, thus leading to an enhanced cycling stability of PAni. The buffer spaces also provide accessible space for the electrolyte to infiltrate active sites, resulting in the improvement of rate

performance of PAni. It should be noted that the strong incorporation of PAni onto PU nanofibers also contributes to the remarkable cycling stability through enhancing the structural stability.

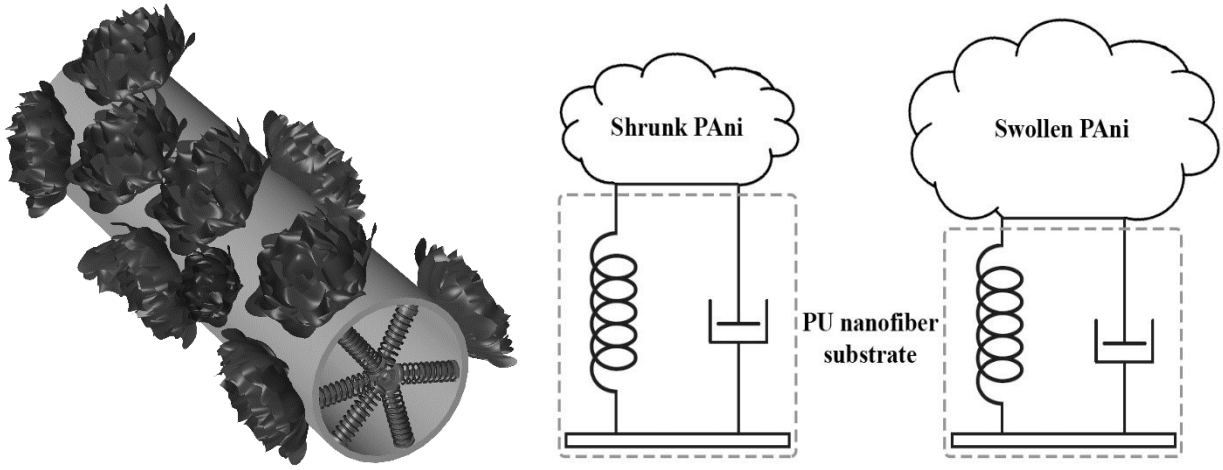

Figure 5.12. A 3D schematic of a viscoelastic nanofiber coated with PAni nanoflowers (left), and schematic of a PAni nanoflower grown on a cushiony PU nanofiber, mitigating the repeated stress induced by volumetric shrinking or swelling of PAni during cycling.

To further investigate the mechanical properties of the PU-based nanofibrous films, a series of tensile tests are carried out. Stress-strain curves of PU, PU/CNT, and PU/CNT/PAni nanofibrous membranes are provided in Figure 5.13. The corresponding mechanical properties of each membrane obtained from the stress-strain curves are also presented in Table 5.1. It is seen that the PU/CNT membrane exhibits larger tensile modulus (207% increase) and ultimate tensile strength (42% increase) than the pristine PU membrane, consistent with the literature [110-112]. This enhancement in the mechanical properties of is attributed to the efficient load transfer to the CNTs oriented along the axis of each nanofiber in the composite. In addition, PU/CNT membrane experiences a smaller elongation-at-break compared to the PU sheet, as expected. PU/CNT/PAni membrane shows a slightly larger tensile modulus and tensile strength than the PU/CNT membrane,

but it possesses a smaller elongation-at-break. This could be explained by the brittle and inelastic nature of PAni (the elastic modulus of emeraldine salt is about 0.9 ± 0.2 GPa [127]).

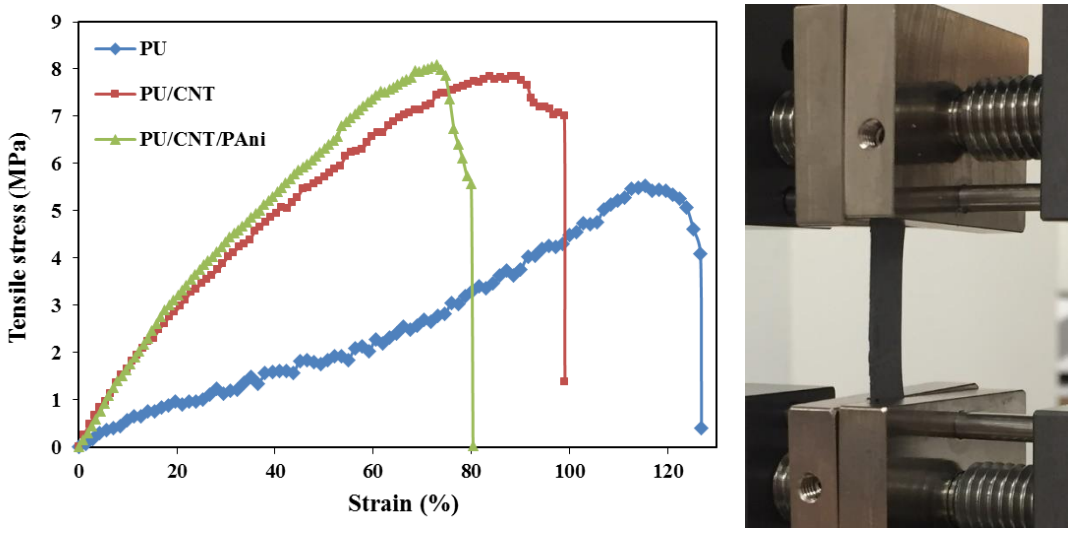

Figure 5.13. (a) Stress-strain curves of PU, PU/CNT, and PU/CNT/PAni nanofibrous sheets. (b) A photograph of PU/CNT membrane under the tensile test.

Table 5.1. Mechanical properties of PU, PU/CNT, and PU/CNT/PAni (with three coats of PAni) nanofibrous sheets obtained from stress-strain curves in Figure 5.13.

Sample	Tensile modulus (MPa)	Tensile strength (MPa)	Elongation at break (%)
PU	5.0	5.5	126.9
PU/CNT	15.3	7.9	99.1
PU/CNT/PAni	16.4	8.3	80.3

To explore the effect of CNTs on the elastic modulus and hardness (which are correlated to the stiffness) of PU nanofibers along the transverse direction, a series of nanoindentation tests are performed on the PU and PU/CNT membranes (Figure 5.14). Interestingly, the average elastic modulus of the PU/CNT membrane along the transverse direction is only 5% more than that of PU membrane, suggesting the negligible reinforcing effect of CNTs on the transvers direction. Similarly, PU and PU/CNT membranes show the same mean

hardness (0.2 MPa). The results of tensile and nanoindentation tests imply that the orientation of CNTs along the axis of an individual PU nanofiber increases the longitudinal strength of the nanofiber while barely affecting its radial stiffness (or the cushiony effect of an individual PU fiber along the transverse directions). Therefore, the radial stiffness of individual PU/CNT nanofibers is comparable to the PU stiffness, justifying the analogy to a vibration isolator or cushiony support for PAni. In addition, the horizontal line at 20 μN in the load-displacement curves (Figure 5.14a) is the indication of the creep behavior of PU and PU/CNT membranes, confirming the viscoelastic properties of PU and PU/CNT.

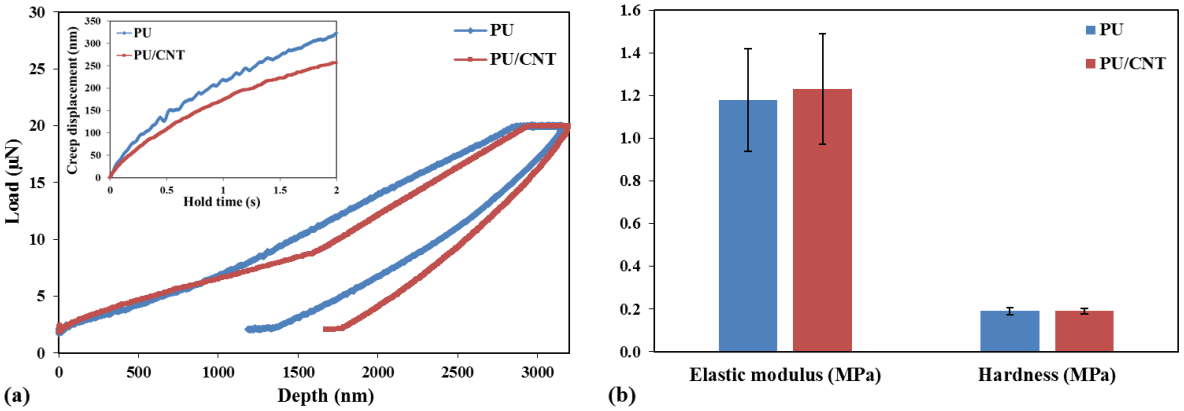

Figure 5.14. Load-displacement curves of nanoindentation tests for PU and PU/CNT nanofibrous membranes (one curve out eight curves is shown for each membrane as an example). The inset is the creep curve at a constant load 20 μN for 2 s. (b) A comparison of the average elastic modulus and hardness for PU and PU/CNT membranes calculated from the load-displacement curves of eight points for each membrane; the standard deviation is shown as error bars. It should be noted that the calculated mean compressive modulus of PU membrane (1.2 MPa) is smaller than the bulk PU modulus possibly due to the buffer spaces between the layers of nanofibers.

5.5 Conclusion

In summary, a flexible electrode for SCs with excellent cycling stability has been developed by coating flower-like PAni on CNT-reinforced PU nanofibers prepared by electrospinning technique. Scalable electrospinning production of PU nanofibers as well as the low cost,

chemical resistance and flexible nature of PU membrane make it a great polymer as a support for deposition of PAni as well as other redox active conducting polymers and metal oxides. The *in situ* polymerization of aniline is controlled such that a flower-shaped nanostructure of PAni is grown on individual PU nanofibers creating a membrane with high porosity and surface area. The results show that the assembled SC from the film with three coats of PAni exhibits superior areal-specific capacitance, energy and power densities compared to the film with two coats of PAni. Furthermore, a fabricated SC from a PU/CNT/PAni film shows an outstanding cycling performance during 10000 cycles of charge-discharge. The long-term stability of the SC is mainly attributed to the usage of the PU substrate that cushions the stress induced by the successive volume change of PAni during charge-discharge cycles. The adjustable mass loading and facile fabrication process of PU/CNT/PAni flexible electrode as well as its prolonged cycle life make it a great candidate to be used for flexible and wearable pseudocapacitive SCs.

In the next chapter, a similar approach of fabricating a flexible PAni-based electrode will be introduced. The main focus will be improving the cycling stability of PAni-based electrodes by using a cross-linked nanofibrous PVA as a cushiony support for PAni nanostructure. The nanofibrous PVA is more beneficial than PU as a substrate for growing PAni since PVA is more resistant to degradation in an acidic environment than PU in case of water evaporation from a SC cell. In the next chapter, a unique acid-base shape memory phenomenon will be introduced for the PAni-coated PVA film.

Chapter 6:

Extraordinary Cycling Stability of Supercapacitors Based on Polyaniline Grown on Crosslinked Nanofibrous Films with Chemical Shape Memory

6.1 Abstract

To address the poor cycle life of polyaniline (PAni), a novel flexible electrode is developed by growing a 3D PAni nanostructure on graphene-coated polyvinyl alcohol (PVA) nanofibers. Chemical stability, wettability, large surface area, and scalable electrospinning production of nanofibrous crosslinked PVA make it an excellent choice as a cushiony support for growing PAni. Exfoliated graphite (ExG) is employed as an inexpensive source of graphene to enhance the capacitive performance of PAni. The assembled supercapacitor from the flexible PVA/ExG/PAni film maintains its capacitive performance for 84k cycles of charge-discharge at 35 mA demonstrating an unprecedented cycling stability. The prolonged cycle life herein is attributed to the cushiony effect of nanofibrous PVA that alleviates the stress induced by repeated volume change of PAni during charge-discharge cycles. The strong embedment of PAni onto PVA nanofibers and ExG together with the buffer spaces between PVA nanofibers lead to additional structural stability of PAni and thus enhanced cycling stability. In addition to SC application, the PAni-coated PVA film exhibits a rapid shape memory phenomenon on the basis of expansion and contraction of PAni upon doping in an acid and dedoping in a base. The simple strategy to attain a flexible

composite electrode with a long cycle life and a unique acid-base shape memory phenomenon could offer new opportunities for flexible supercapacitor as well as chemo-mechanical actuation devices.

6.2 Introduction

PAni is a promising conducting polymer for electrodes of SCs owing to its low cost, facile synthesis, environmental stability, controllable electrical conductivity, and pseudocapacitance higher than specific capacitance in electrical double-layer SCs [1, 13, 102-103]. However, PAni suffers from poor cycle life in aqueous electrolytes rooted in the repeated volumetric swelling and shrinking as a result of insertion/de-insertion of counterions during the charge-discharge cycles [26]. The successive volume change of PAni causes structural instability and undesirable changes to the morphology of PAni, and thus the degradation of capacitive performance over cycling. For instance, PAni could form a compact structure preventing effective insertion/de-insertion of counterions to deeper PAni chains by blocking some of the ion channels. This mechanical instability could also lead to structural pulverization of PAni, and thereby fast capacitance decline of PAni.

One way to improve the conductivity and cycling stability of PAni is developing composite electrode materials by growing PAni on carbonous nanomaterials [12, 94, 113], such as CNTs [46] and graphene [55, 58]. The enhancement of cycle life of PAni/carbon composites could be explained by the good affinity of PAni to surface of carbonous materials through the interactions including π-π stacking, electrostatic interactions, and hydrogen bonding, and thereby is effective for extremely low mass-loading of PAni [27]. Another technique to stabilize PAni could be depositing a thin protective layer on PAni nanostructures. For

example, a 95% capacitance retention after 10k cycles at a scan rate of 100 mV/s in 1 M H_2SO_4 electrolyte was achieved by hydrothermal deposition of a 5 nm protective layer of carbon onto the surface of PAni nanowires [115]. Xia et al. [128] reported capacitance retention of 88% after 10k cycles at current density of 20 A/g for PAni nanofibers by growing a 2 nm protective layer of RuO_2 by atomic layer deposition. This approach, however, is cumbersome, costly, and requires an extremely low mass-loading of PAni.

Another strategy to enhance cycling stability is growing PAni on a cushiony support to mitigate the stress induced by repeated volume change of PAni during cycling [27]. In our recent work [27], flower-like PAni was grown on CNT-reinforced electrospun polyurethane (PU) as a flexible electrode for SCs with remarkable cycling stability. Three ways through which a cushiony nanofibrous support contributes to enhancing the cycle life of PAni were discussed in [27] as follows. Similar to a vibration isolator, the low stiffness combined with the damping effect of individual PU nanofibers cushions the stress induced by volumetric swelling and shrinking of PAni during cycling, resulting in improved structural stability. Furthermore, buffer spaces between PU nanofibers accommodate extra space for volume expansions of PAni grown on PU nanofibers. Lastly, the strong embedment of PAni into PU nanofibers enhances further structural stability of PAni. It should be noted that growing PAni on a material with a large elastic modulus, such as carbon fibers, graphene, CNTs, and metal substrates, is unlikely to alleviate the stress caused by volume change of PAni. On the other hand, a cushiony support with a small elastic modulus (low stiffness) and an energy dissipation mean (damping), such as PU or a hydrogel, could play the stress isolation role [27]. Hence, it is expected that integrating PAni into a hydrogel structure could enhance PAni stability in a similar manner. Hao et al. [129] used *in situ* polymerization to integrate

PAni into pre-organized α-cyclodextrin-containing polyacrylamide hybrid hydrogels with stretchability and homogeneous and interconnected macro-pores. They anticipated that well integration of PAni into structure of the hybrid hydrogel along with the flexible nature of the polymer networks could buffer the volume changes during cycling processes, and thus a capacitance retention of 92% after 35k cycle of charge-discharge in the range of 0 to 0.8 V at a current density of 8 A/g was achieved. However, the large water content and low surface area of the hybrid hydrogel diminish the overall capacitance, and thus limit its application as a high-performance SC electrode. Wang et al. [130] fabricated an integrated flexible SC by embedding PAni in chemically crosslinked polyvinyl alcohol (PVA) hydrogel by *in situ* polymerization. However, the low surface area of the hydrogel and the relatively large thickness of the PVA film (2 mm) lead to an inferior mass- and volumetric-specific capacitances, a major hurdle for its application as a SC electrode. The stress caused by the large volume expansion due to the insertion/de-insertion of positive ions in the rechargeable batteries could be accommodated by integrating cushiony materials in a similar manner. For example, coating sulfur particles with poly(ethylene glycol) can play this buffering role in a rechargeable lithium-sulfur battery cathode [131]. Gao et al. [132] applied cross-linked chitosan to suppress adverse mechanical effects from the volume change of antimony anode upon sodiation/de-sodiation in sodium-ion batteries.

Here, a flexible electrode for SC with an unprecedented cycling stability is developed by growing PAni on graphene-coated cross-linked PVA nanofibers. The nanofibrous PVA contributes to the stability of PAni as a cushiony support in a similar manner to our recent work [27]. PVA is a hydrophilic, nontoxic, biocompatible, and biodegradable polymer with chemical and mechanical

stability [133]. PVA is resistant to degradation in an acidic environment but PU could degrade in high concentration acidic electrolyte in case of water evaporation from a SC cell.

In addition, the wettability of PVA nanofibers leads to a more effective PAni coating during an *in situ* polymerization. Moreover, the wettability of nanofibrous PVA makes it an ionically conductive matrix which enables a more effective access of aqueous electrolyte ions to the active sites of the electrode. In other words, electrolyte ions are accessible through both inner and outer sides of active materials coated on individual PVA nanofibers. Therefore, the nanofibrous PVA outmatches hydrophobic nanofibers as flexible support for growing PAni. In a typical preparation process, the nanofibrous PVA mat is prepared by electrospinning followed by glutaraldehyde vapor cross-linking to make it water insoluble. To achieve enhanced capacitive performance, exfoliated graphite (ExG) is decorated onto the PVA nanofibrous mat before the *in situ* growing of PAni. As an inexpensive source of graphene, ExG is prepared by an electrochemical exfoliation of graphite followed by a post-exfoliation [28]. To prepare a hierarchical PVA/ExG/PAni nanostructure, PAni is coated on PVA nanofibers as well as ExG by an *in situ* polymerization. The assembled SC from the flexible PVA/ExG/PAni film maintains its performance for 84k cycles of GCD at 35 mA showing a remarkable cycling stability. Furthermore, the PAni-coated PVA film shows a unique and rapid acid-base shape memory phenomenon on the basis of expansion and contraction of PAni upon doping and dedoping.

6.3 Experimental Methods

6.3.1 Preparation of PVA Nanofibers

100 mg/mL PVA (Mw: 205,000 aladdin) solution is prepared by dissolving PVA powder in deionized water at 90 °C with magnetic stirring for 6 hours. When the aqueous PVA solution is cooled down to room temperature, it is directly used in the electrospinning process to make the PVA nanofibrous membrane. Briefly, 10 mL of the PVA solution is loaded into a syringe installed on a syringe pump (PHD2000 Harvard apparatus, Instech Laboratories, Inc.). The positive lead of a high voltage DC power supply (High Voltage Research, GAMMA) is connected to the syringe needle (18 gauge) and the ground connection is attached to an aluminum foil (10 cm×10 cm) as the collector. The distance between the needle tip and the collector is set to be 12 cm. The infusion rate of the syringe is set to 0.8 mL/h, and a voltage of 20 kV is applied once the first drop appears at the needle tip. Fibers thus formed were then cured at room temperature for 24 hours.

6.3.2 Cross-linking of Electrospun PVA

Since PVA is highly soluble in water, a post crosslinking of the nanofibrous mat is carried out to improve the water resistance property of the electrospun mat before any applications. The crosslinking procedure is carried out by subsequent exposure of the electrospun mat to first HCl (37%, Sigma-Aldrich) and then glutaraldehyde (25%, Alfa-Aesar) vapors (for 3 hours each) in a sealed container for a total duration of 12 hours.

6.3.3 Preparation of the ExG

ExG is synthesized by an electrochemical exfoliation of graphite followed by a post-exfoliation in a microwave as reported in 4.3.1. Briefly, two graphite rods (6.3 mm in diameter) are positioned 1 cm apart in a 0.1 M aqueous solution of sodium sulfate. A positive voltage (12 V) is applied between the electrodes (rods) to perform the electrochemical exfoliation in the anode. After sonicating the dispersion at a low power for 30 min, it is kept for 10 min for the precipitation of un-exfoliated and large-sized graphite particles (micro-sized graphite). Then, the top part (50%) of the dispersion is collected and washed with deionized water by vacuum filtration through a Whatman filter paper (grade 5 with pore size of 2.5 μm). The post-exfoliation is carried out by irradiating the dried product in a microwave under the power of 700 W for 20 to 50 seconds depending on the quantity of partial-exfoliated graphite. The microwave irradiation is accompanied by a visible volume expansion of the ExG powder, fuming, and lightening due to detachment of graphene layers in each graphite particle [28].

6.3.4 Preparation of PVA/ExG mat

A 10 mg/mL ExG dispersion is sonicated in a bath-sonicator (VWR International, LLC.) at 100 W for 30 min. Then, a piece of PVA nanofibrous mat is dipped into the ExG dispersion, soaked for 20 min at room temperature, and dried in a vacuum oven at 30 ºC for 6 h. This dipping/drying process is repeated to attain the required mass-loading of ExG. The weight of ExG coated on the PVA nanofiber is calculated by the weight difference before and after coating.

6.3.5 Preparation of PVA/PAni and PVA/ExG/PAni films

PVA and PVA/ExG nanofibrous mats are coated with PAni by a controlled *in situ* polymerization of aniline similar to our previous work [28]. In a typical procedure, the nanofibrous mat is soaked for 3 h in a solution of 0.32 mL aniline (≥99.5%, Sigma-Aldrich) dissolved in 70 mL of 1 M Sulfuric acid (H_2SO_4, 98%, Anachemia). Afterwards, another solution containing 266.7 mg of ammonium persulfate (APS, ≥98.0%, Sigma-Aldrich) in 10 mL of deionized water is added to the former solution at room temperature. Both solutions are kept in 4 ºC before mixing. After reaction for 2 hours, the PAni-coated mat is removed and washed with deionized water, followed by drying between two plastic sheets at the ambient temperature. Likewise, subsequent coatings are carried out to increase the mass-loading of PAni. The weight of the PAni coated on the membrane after each coating is calculated by the difference in the dried weight of samples before and after a coating process. Similar to our previous study [27], we carried out three coats of PAni on PVA and PVA/ExG mats to attain required mass-loading of PAni.

To prepare a PVA/PAni mat with an asymmetric coating of the two sides, the PVA mat is placed carefully on the surface of the reaction solution after mixing solutions containing aniline and APS. Hence, more PAni is grown on the side of the mat facing the solution than the other side.

6.3.6 Characterization

To carry out the electrochemical tests, two identical strips of PVA/PAni or PVA/ExG/PAni are assembled in a symmetric SC. Two rectangular electrodes are directly cut from PVA/PAni or PVA/ExG/PAni film (2 cm×1.5 cm) and are soaked in 1 M sulfuric acid for

5 hours. Two stainless-steel foils are used as the current collectors and a strip of filter paper (Whatman, grade 5) wetted with 1 M sulfuric acid is used as the separator. Then, the two electrodes, separated by the filter paper and sandwiched between the current collectors, are assembled into a layered structure and sealed with a parafilm to prevent water evaporation. The mass-loading of active materials on PVA mat for PVA/PAni and PVA/ExG/PAni films (three coats of PAni in both cases) are around 1.13 mg/cm^2 and 1.46 mg/cm^2, respectively. The galvanostatic charge-discharge (GCD) tests are run from 0 to 0.8 V at a constant current ranging from 5 to 75 mA. The electrochemical impedance spectroscopy (EIS) measurements are carried out over a frequency range from 10^5 to 0.01 Hz at an AC amplitude of 10 mV and zero DC amplitude. The cyclic voltammetry (CV) tests are recoded from -0.8 to 0.8 V at a constant scan rate ranging from 10 to 100 mV/s.

6.4 Results and Discussion

SEM images of PVA/PAni films with three coats of PAni in Figure 6.1 confirm the effective growth of porous PAni nanostructures on the PVA nanofibers as well as the high surface area of the electrospun film. The mechanism of PAni decoration on nanofibers is explained as follows. Upon immersing the PVA nanofibrous mat in the diluted aqueous solution of aniline, aniline monomers solved in water penetrate into individual nanofibers due to the wettability of PVA nanofibers. Upon the addition of APS solution and the initiation of the *in situ* polymerization of aniline, PAni chains nucleate from every spot on nanofibers, and consequently grow into a 3D PAni nanostructure. SEM images of PVA film coated with a limited PAni after a shorter reaction time (20 min instead of 3 h) show the homogenous nucleation of PAni from the nanofibers covering every spot on a nanofiber (Figure 6.2). Thus,

PAni nanostructures are firmly rooted into PVA nanofibers leading to enhanced structural stability of PAni, and thereby prolong cycle life. Moreover, the combination of the high surface area of the electrospun PVA and the porosity of grown PAni nanostructures leads to enormously accessible surface area of PAni, which is an essential asset for a high performance electrode material. Another asset of this design is the water absorption capability or (wettability) of PVA that assist more effective access of the aqueous electrolyte to the active sites. To prevent the formation of bulk PAni on the PVA nanofibers, a low concentration of aniline is utilized for the *in situ* coating process, resulting in a fine morphology of PAni nanostructure [27]. To yield a film with a higher mass-loading of PAni, subsequent coating processes are conducted.

PAni is often combined with carbonous materials in order to achieve enhanced capacitive performance through improving the conductivity and mechanical stability of PAni [134]. In such a composite, PAni provides a large pseudocapacitance and a carbonaceous material contributes to a good cycling stability, rate capability, and a high power density at a large current. Generally graphene has much better cycling stability than PAni because the energy storage mechanism of graphene involves physical movement of ions rather than chemical changes to graphene. The charge storage mechanism of PAni involves reversible redox reactions which cause successive volumetric swelling and shrinking of PAni during charge-discharge cycling. The repeated volume change leads to structural instability and undesirable changes to the morphology of PAni. Incorporation of ExG (as the source of graphene) into PVA/PAni composite enhances the cycling stability in two ways: graphene, as a portion of active materials, improves the overall stability; and the good affinity between graphene and those PAni chains grown on graphene sheets enhances the stability.

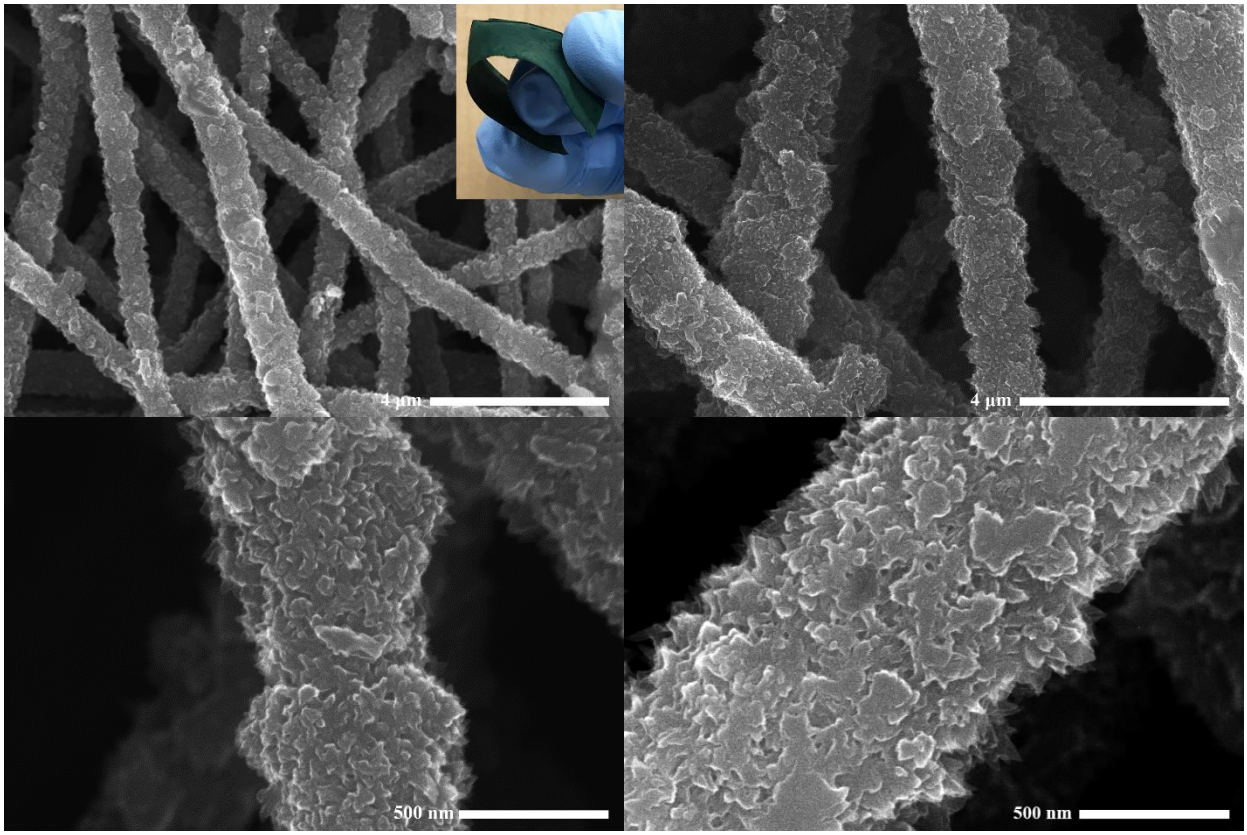

Figure 6.1. SEM images of PVA/PAni films with three coats of PAni; inset is the photograph of the flexible PVA/PAni film.

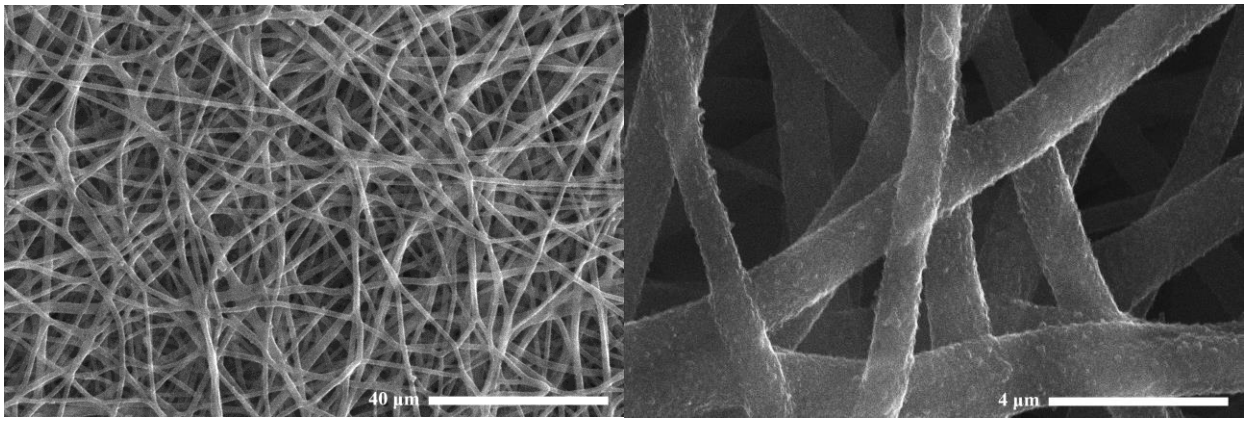

Figure 6.2. SEM images of PVA film coated with PAni after a limited reaction time (20 min), which show the homogenous nucleation of PAni on the nanofibers.

Therefore, we prepare PVA/ExG/PAni in addition to PVA/PAni. Briefly, the PVA nanofibrous mat is coated with a highly conductive ExG before growing PAni on it to prepare a hierarchical PVA/ExG/PAni nanostructure. Figure 6.3 shows the SEM images of a PVA/ExG film along with the photograph of the flexible film elucidating its flexibility. SEM images in Figure 6.4 show the morphology of the PVA/ExG/PAni mat after three coats of PAni, and thus confirming the effective decoration of PAni on the PVA/ExG film. It is seen that ExG (graphene) is a secondary nucleation site for the growth of PAni in addition to PVA nanofibers. PAni grows on the surface of ExG in form of short nanowires. Therefore, two forms of PAni can be observed from SEM images; i.e. short PAni nanowires grown on graphene layers of ExG and porous PAni nanostructure rooted in PVA nanofibers, both of which contribute to highly porous and hierarchical PVA/ExG/PAni nanostructure. The inset in Figure 6.4 is the photograph of the flexible PVA/ExG/PAni film cut into a rectangular electrode to be assembled into a SC. The highly flexible PVA nanofibrous mat facilitates the flexibility of the hierarchical PVA/ExG/PAni film making it a great candidate for wearable SCs.

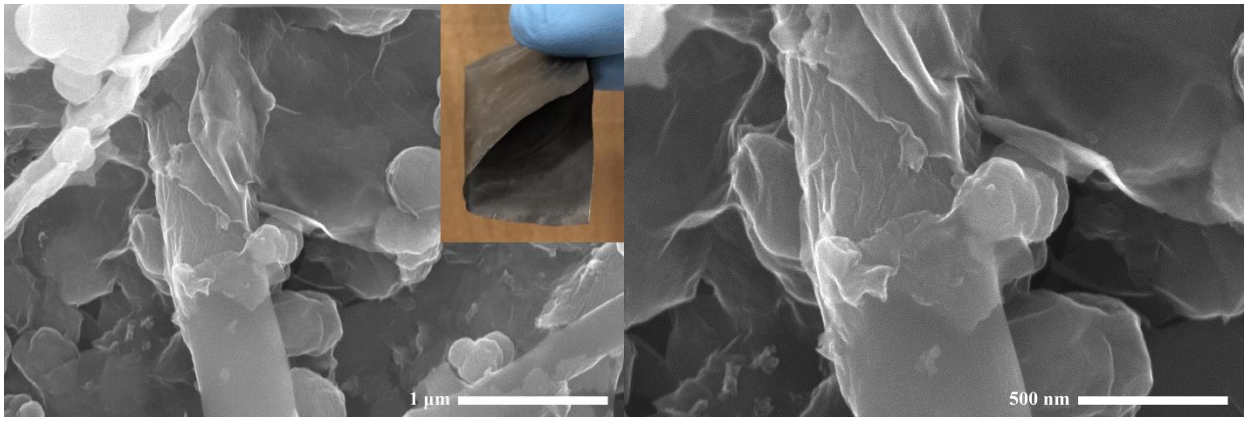

Figure 6.3. SEM images of a PVA/ExG film; inset is the photograph of the flexible film.

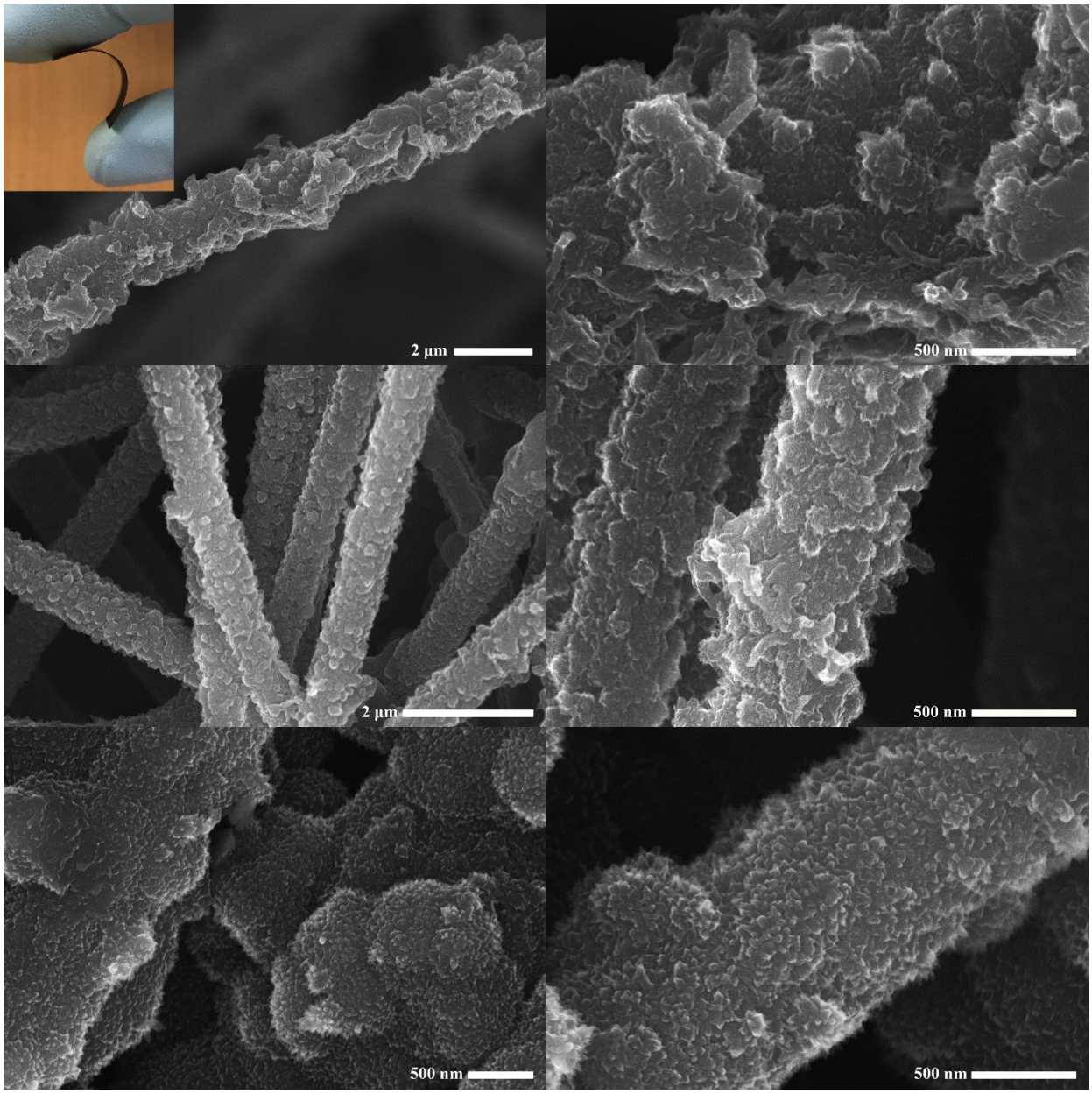

Figure 6.4. SEM images of PVA/ExG/PAni film (three coats of PAni); inset is the photograph of the flexible film.

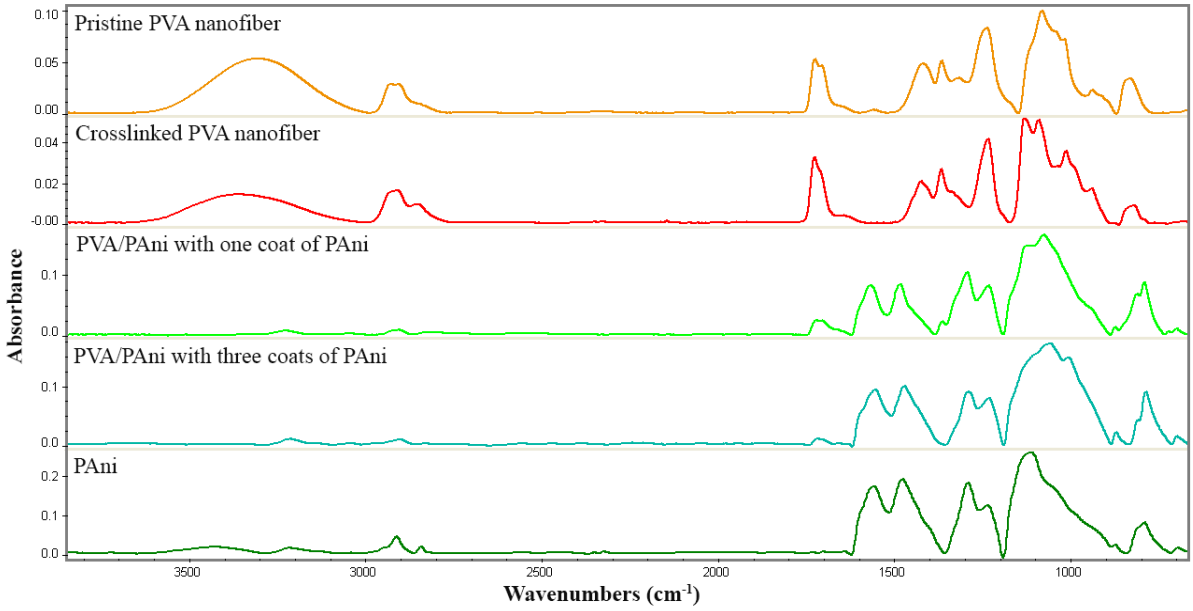

Figure 6.5. FTIR spectra of pristine PVA nanofiber, crosslinked PVA nanofiber, PVA/PAni with one coat of PAni, PVA/PAni with three coats of PAni, and PAni.

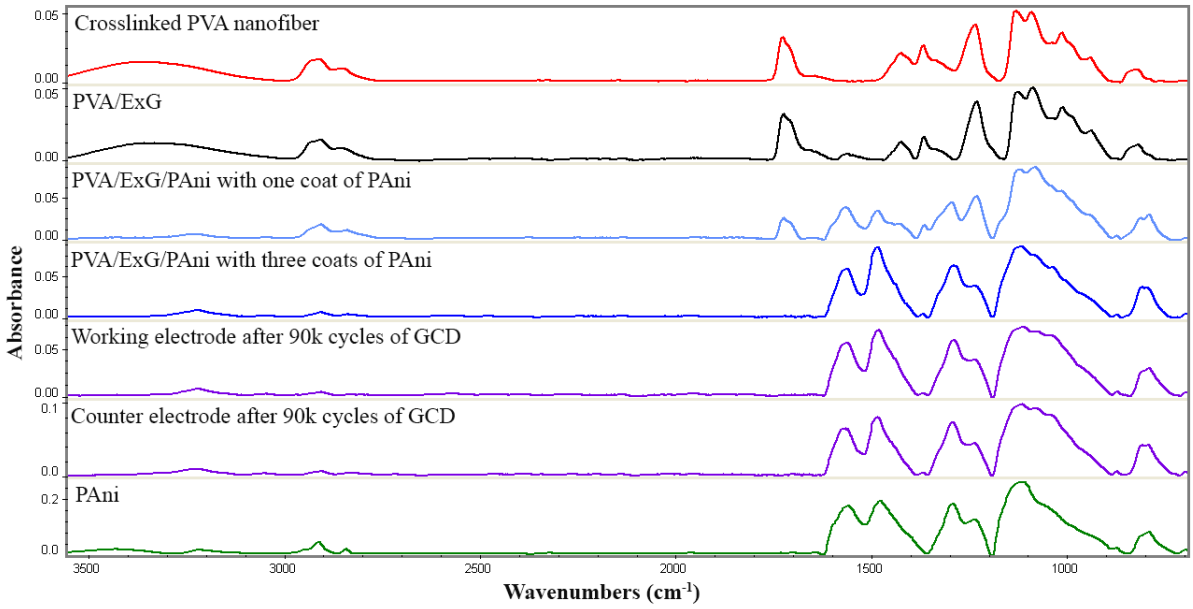

Figure 6.6. FTIR spectra of crosslinked PVA nanofiber, PVA/ExG, PVA/ExG/PAni with one coat of PAni, PVA/ExG/PAni with three coats of PAni, PVA/ExG/PAni (working electrode after 90k cycles of GCD), PVA/ExG/PAni (counter electrode after 90k cycles of GCD), and PAni.

FTIR spectra of various samples are provided in Figure 6.5 and Figure 6.6 to assist further discussion of the as-prepared composite films. The first FTIR spectrum in Figure 6.5 reveals the typical peaks associated with PVA [135-136] at 3000-3600 cm^{-1} (broad -OH stretching), 2800-300

cm^{-1} (C-H alkyl stretching), 1733 cm^{-1} (C=O stretching of residual acetate CH_3CO_2-), 1300-1500 cm^{-1} (C-H bending) and 1090 cm^{-1} (C-O stretching). The second spectrum in Figure 6.5 is associated with PVA crosslinked by glutaraldehyde vapor. By crosslinking the PVA, the -OH stretching peak at 3000-3600 cm^{-1} is decreased when compared to pure PVA because of the decrease in the number of -OH groups due to the formation of acetal bridge [133, 135]. It is also observe that the new peak at 2860 cm^{-1} refers to the stretching vibration of O=C-H from the aldehyde. The peak at 1734 cm^{-1} (C=O stretching) in spectrum of crosslinked PVA could also be due to the unreacted end of the aldehyde [133, 135]. In addition, the 1090 cm^{-1} (C-O stretching) in PVA is replaced by broader absorption peaks 1000-1140 cm^{-1} (C-O-C stretching of acetal group) formed by the crosslinking of PVA with glutaraldehyde. Therefore, it is evident that PVA nanofibers are chemically crosslinked by glutaraldehyde. Moreover, a crosslinked PVA mats is soaked in water for several days to ensure the successful crosslinking procedure.

The spectrum of pure PAni gives typical peaks of PAni in the emeraldine salt state [27-28]. The FTIR spectra of PVA/PAni with one or three coats of PAni show all the expected characteristic peaks of PAni, confirming that PAni has been successfully coated on PVA nanofibers. In addition, the spectra of PVA/PAni films show traces of two absorption peaks of crosslinked PVA, i.e. C=O stretching and C-O-C stretching of acetal group. It is also seen that the peak at 1730 cm^{-1} (C=O stretching) in the spectrum of PVA/PAni with one coat of PAni is stronger than the one with three coats of PAni due to less coating of PAni on PVA. Interestingly, the peak at 3000-3600 cm^{-1} (-OH stretching) in the spectrum of crosslinked PVA and the peak at 3437 cm^{-1} (N-H stretching) in the PAni spectrum are absent in the spectra of PVA/PAni films. This can be attributed to the formation of hydrogen bonds between hydroxyl groups of PVA and N-H groups of PAni. Hence, PAni is decorated onto PVA nanofibers through the hydrogen bonding between PAni and PVA nanofibers.

Although most of infrared radiation, are absorbed by ExG in the FTIR spectra of films with coated with ExG, major peaks can still be observed after baseline correction of each spectrum. The spectrum of PVA/ExG film in Figure 6.6 gives all characteristic peaks of crosslinked PVA nanofiber. In addition, the peak at 1574 cm^{-1} is attributed to aromatic C=C stretching bond of graphene. Similar to PVA/PAni, the spectra of PVA/ExG/PAni with one or three coats of PAni also confirm the successful decoration of PAni on PVA/ExG films.

The electrochemical performance of SCs assembled from PVA/PAni and PVA/ExG/PAni (with three coats of PAni) is evaluated by GCD tests in a symmetric two-electrode system. Firstly, the capacitive performance of SCs fabricated from PVA/PAni film and PVA/ExG/PAni film are evaluated and compared (Figure 6.7). Afterward, an extensive study is carried out on the cycling performance of the PVA/ExG/PAni based SC. It should be noted that the conductivity of the films after the first PAni coating is inadequate for a SC electrode. In our previous study [27], we investigated the effect of PAni mass loading by comparing the capacitive performance of two or three coats of PAni on PU nanofibers. Herein, only three coats of PAni on PVA and PVA/ExG mats are carried out to attain required mass-loading of PAni, and therefore no result is presented for two coats of PAni. The main objective herein is to study the cycling performance of PVA/ExG/PAni film.

The GCD curves of assembled SCs from films of PVA/PAni and PVA/ExG/PAni are plotted for different currents in Figure 6.7a and b, respectively. It is observed that the discharge curves for PVA/PAni experience a larger potential drop compared to those of PVA/ExG/PAni. The specific capacitances, power densities, and energy densities for PVA/PAni and PVA/ExG/PAni are calculated from GCD curves using the formulae in section 6.3.6. According to Figure 6.7c and d, SCs based on the PVA/ExG/PAni device exhibits a slightly larger areal-specific

capacitance but a smaller mass-specific capacitance due to a larger mass-loading of active materials (i.e. it is coated with ExG in addition to PAni). For example, the specific capacitances of PVA/PAni and PVA/ExG/PAni, estimated at a discharge current of 35 mA, are 72.13 F/g (0.16 F/cm^2) and 58.55 F/g (0.17 F/cm^2), respectively. Moreover, the SC based on PVA/ExG/PAni shows a better rate capability than PVA/PAni since it can operate in a larger current (i.e. 100 mA). Carbonous materials generally show a better rate capability than PAni, and thus addition of ExG improves the overall rate capability of the composite film. Figure 6.7e indicates that the SC based on PVA/ExG/PAni shows a lower ESR (better conductivity) than PVA/PAni owing to the addition of ExG. The Ragone plots (power density versus energy density at different currents) in Figure 6.7f indicate that PVA/ExG/PAni SC clearly outperform PVA/PAni SC in terms of power and energy density. For instance, at the discharge current of 35 mA, the power densities of PVA/PAni and PVA/ExG/PAni are 745.58 W/kg (1.69 mW/cm^2) and 688.9 W/kg (2.02 W/cm^2), respectively, and their corresponding energy densities are 0.84 Wh/kg (1.9 μWh/cm^2) and 0.98 Wh/kg (2.9 μWh/cm^2). Generally, at a same current, the PVA/ExG/PAni SC exhibits superior areal-specific capacitance, conductivity, and areal energy and power densities. The superb electrochemical performance of the PVA/ExG/PAni film could be attributed to the combination of PAni with graphene (ExG) as highlighted in the literature.

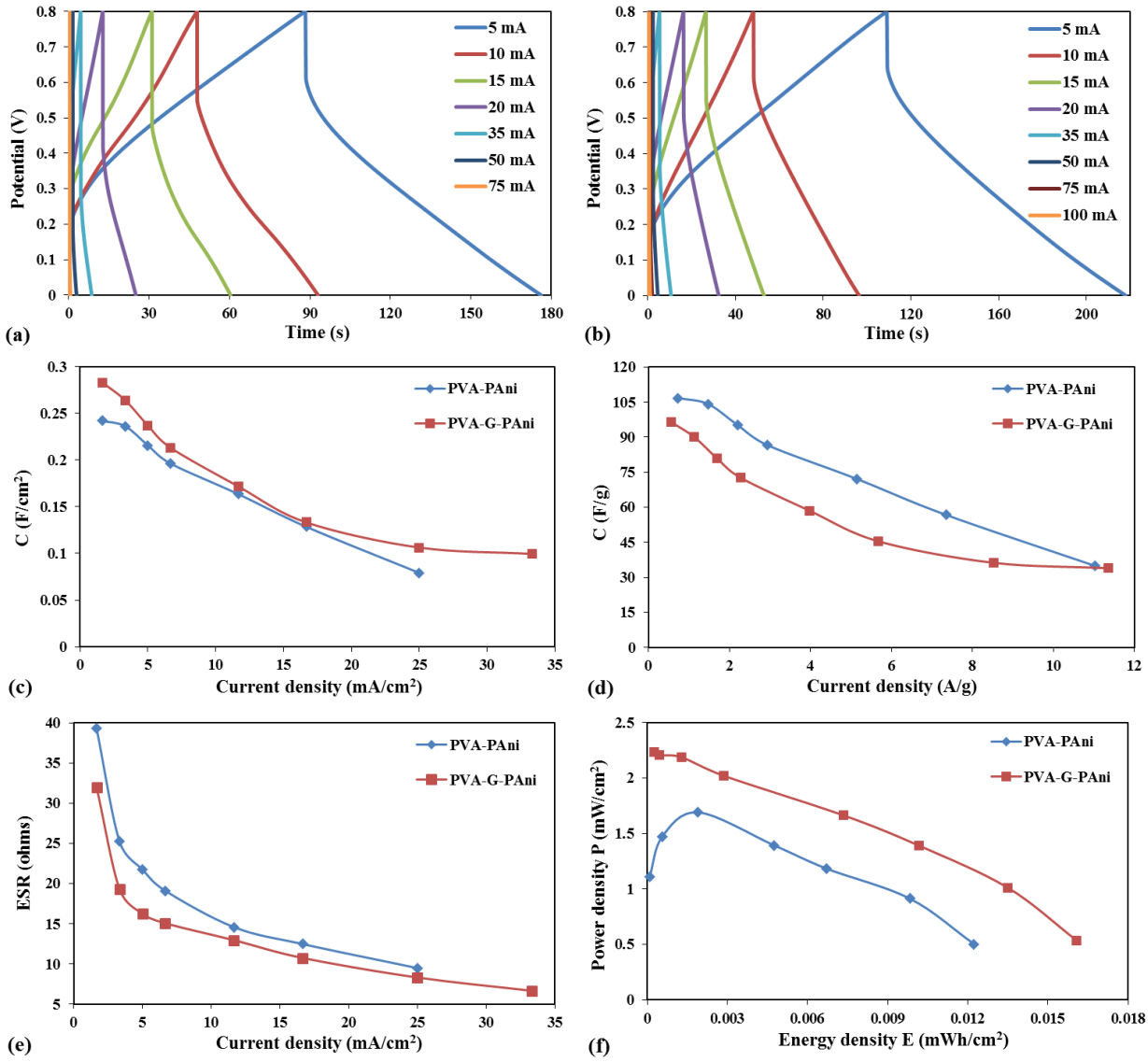

Figure 6.7. The GCD curves of assembled SCs from films of (a) PVA/PAni, and (b) PVA/ExG/PAni; (c) Areal-specific capacitance versus areal current density, (d) mass-specific capacitance versus current density, (e) ESR versus areal current density (f) areal power density versus energy density, for PVA/PAni and PVA/ExG/PAni (three coats of PAni).

To investigate the cycling performance of the assembled SC from PVA/ExG/PAni film (three coats of PAni), 90k cycles of GCD at 35 mA are carried out (a series of 15 consequent 6k cycles with approximately 4h rest period between each 6k cycling test). During the four-hour gap, a series of GCD, EIS, and CV tests are carried out on the SC to evaluate the capacitive performance after each 6k cycling test. The areal-specific capacitance, areal energy

density, and areal power density, obtained from GCD tests at different currents (10, 20, 35, 50 mA), tested after each 6k cycles, are illustrated in Figure 6.8 (a-c), respectively. We investigate the cyclic performance of capacitance, power density, and energy density as a measure of the cyclic performance of SCs, as argued in section 5.4. Significantly, it is seen that all the capacitance, energy density, and power density are steady up to 84k cycles of GCD for all the currents (10-50 mA). This shows that the fabricated SC can operate up to 84k cycles of charge and discharge. In addition, EIS tests presented in the form of Nyquist plots and GCD curves tested at 10 mA and 35 mA, tested after each 6k cycling test, are shown in Figure 6.8 (d-f), respectively. The GCD curves and Nyquist plots also confirm the unprecedented cycling stability of the fabricated SC up to 84k cycles. Figure 6.8d and e indicate that the performance of the SC declines dramatically during the 15^{th} 6k cycling test (note: GCD: a larger potential drop and smaller discharge time are indications of inferior performance; EIS: a larger dimeter of the semicircle and more oblique low-frequency line are indications of inferior performance). It can also be observed from Figure 6.8d that the equivalent resistance of first 6k cycling test is larger than subsequent 6k cycling tests (except 15^{th} one). This could be explained by the fact that it takes some time for the ions in the aqueous electrolyte to penetrate deep into the active sites after the initial assembly of the SC. Furthermore, the SC based on PVA/ExG/PAni exhibits a lower charge transfer resistance than PVA/PAni according to EIS tests.

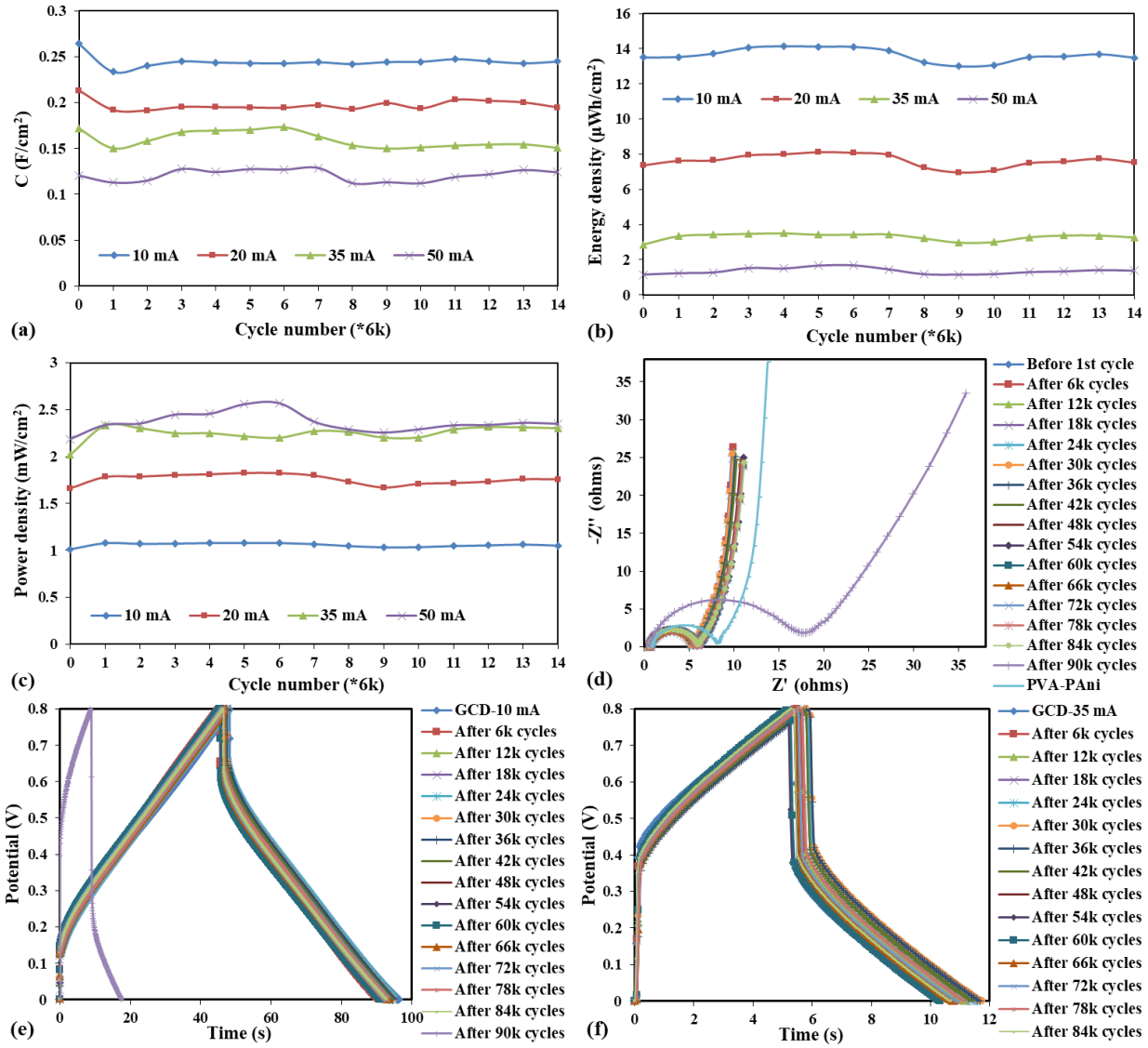

Figure 6.8. Performance of the assembled PVA/ExG/PAni SC tested after each 6k cycling test of GCD at 35 mA (totally 90k cycles); (a) areal-specific capacitance versus cycles, (b) areal energy density versus cycles, and (c) areal power density versus cycles, obtained from GCD tests at different currents (10, 20, 35, 50 mA); (d) Nyquist plots obtained from EIS tests after each 6k cycling test (along with Nyquist plots for the PVA/PAni SC); (e) GCD curves tested at 10 mA after each 6k cycling test; (f) GCD curves tested at 35 mA after each 6k cycling test.

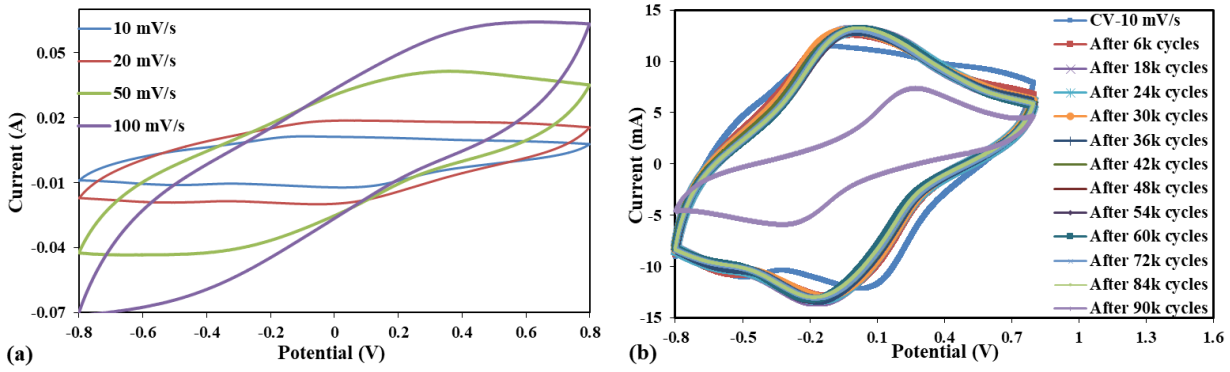

Figure 6.9. (a) CV curves of the SC based on PVA/ExG/PAni; (b) CV curves tested at 10 mV/s after each 6k cycling test.

Figure 6.9a exhibits CV curves of the fabricated SC based on PVA/ExG/PAni recoded from -0.8 to 0.8 V for different scan rates, and Figure 6.9b provides the CV curves of the fabricated SC tested at 10 mV/s after each 6k cycling test. The reduction and oxidation peaks of PAni are not pronounced because CV measurements are carried out in an assembled two-electrode system [11, 63]. Consistent with the results above, the unchanged shapes of CV curves after each 6k cycling test confirm the cycling stability of the device up to 84k cycles. The shape of the 15th CV curve in Figure 6.9b clearly indicates that the capacitive performance of the SC has declined after the 15th 6k cycling test, consistent with the GCD and EIS tests (15th ones). Moreover, the shape of the CV curve for the freshly assembled SC is slightly different from all other CV curves obtained following 6k cycling tests, indicating that the electrolyte is not fully penetrated into the active sites after the initial assembly of the SC.

To further elucidate the behavior of the assembled PVA/ExG/PAni SC, the calculated capacitive parameters from GCD curves for the whole 90k cycles at 35 mA are provided. The areal-specific capacitance, areal energy density, areal power density, ESR, and discharge time, obtained from 90k cycles of GCD at 35 mA, are illustrated in Figure 6.10 (a-e), respectively. Since the potential drop and the discharge time are two characteristics of the GCD curves affecting the capacitance, power, and energy of a SC, we also present the results for the ESR (which is the

reflection of the potential drop) and the discharge time to further help understand the cycling behavior. It is seen that the cycling behavior of the as-fabricated SC during each 6k cycling test has two phases—a transient state up to around 1000th cycle and a steady state afterward. The fact that the fabricated SC can be operated up to 84k cycles without any pronounced decline in the performance (capacitance, energy density, and power density) implies an outstanding cycling stability of the SC. The rapid decline in the all capacitive parameters during the 15^{th} 6k cycling test is clearly observed in Figure 6.10. The sharp decay of capacitive performance during the 15^{th} 6k cycling test might be attributed to water evaporation from the assembled SC and/or counterion drain effect (less and less anions can penetrate into PAni matrix due to the irreversible insertion/de-insertion of counterions after repeated charge/discharge cycling [116]). The mechanism of rapid capacitance depletion will remain for a future investigation with a more controlled experimental setup. According to Figure 6.10, the steady-state values of the capacitance for each 6k cycling test remain unchanged (0.15 F/cm^2) during the whole 84k cycles. The steady-state values of the energy density and power density for each 6k cycling test are around 3.0-3.7 $\mu Wh/cm^2$ and 2.2-2.4 mW/cm^2, respectively. Overall, the capacitive performance improves very gradually from the first 6k cycling test up to 7^{th} one; then there is a gradual decline up to 10^{th} 6k cycling test, from which there is a slight improvement in the capacitive performance. It is note that an improvement in the capacitive performance is reflected in a decrease in the ESR and/or an increase in the discharge time.

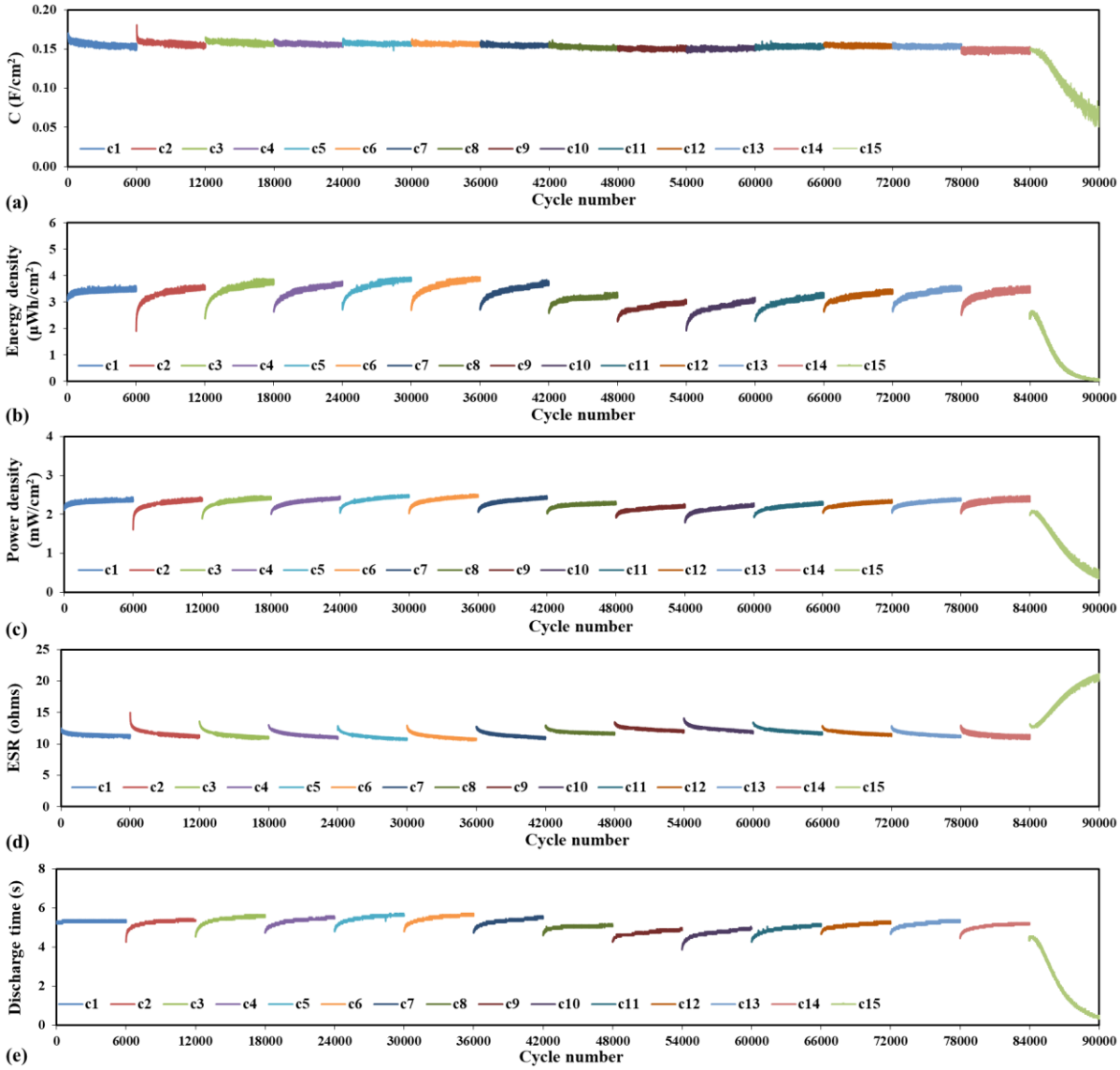

Figure 6.10. Performance of the assembled PVA/ExG/PAni SC for 90k cycles of GCD at 35 mA; (a) Areal-specific capacitance, (b) areal energy density, (c) areal power density, (d) ESR, and (e) discharge time, versus cycle number.

According to Figure 6.10d and e, the initial sharp changes in the ESR and the discharge time during the transient stage indicates the performance recovery, which is attributed to the regulation of ion transport to active sites as well as regulation of redox reactions of PAni. Upon the initiation of charge-discharge cycles, it takes some time for electrolyte ions to effectively diffuse into the active sites from their initial equilibrium state [27-28]. It should be noted that the duration of the transient phase (or the performance recovery stage) depends on factors such as

experimental conditions, the sample type, and type of electrochemical tests conducted on the device right before the initiation of cycling test. Some tests might be detrimental to PAni, such as performing a test with a large potential window since it enforces PAni to experience various oxidation states. After each 6k cycling test and before the next set of cycling test (during the four-hour rest period), we carried out EIS, GCD tests (0-0.8 V), and CV tests (-0.8-0.8 V), respectively. By performing another GCD test at 35 mA after CV tests (Figure 6.11), the adverse effect of CV tests with a larger potential window (-0.8-0.8 V) is observed (the late GCD curve shows a larger potential drop and a smaller discharge time). The voltage difference between the positive and negative electrodes changes from -0.8 to 0.8 V, implying that each electrode experiences 1.6 V potential change. Hence, it takes several cycles before the active materials recover from the adverse effect of a large potential change in electrodes and adapt to the new experimental condition, particularly those PAni chains that are not in an immediate vicinity of the electrode surface.

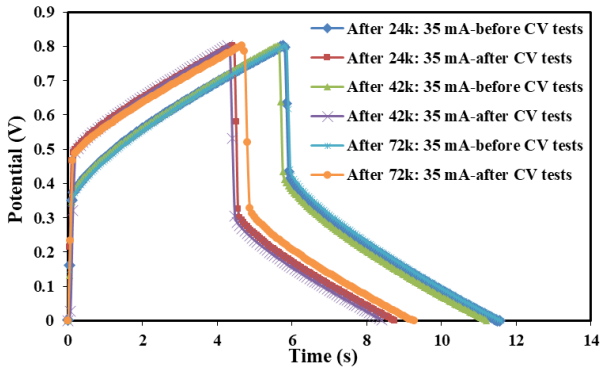

Figure 6.11. Comparison of GCD curves tested at 35 mA before and after CV tests, performed on the SC during the rest time after the 4th, 7th, and 12th 6k cycling tests.

To illustrate the detailed capacitive behavior of the assembled PVA/ExG/PAni SC for each one of 6k cycling test of GCD at 35 mA, percentages of power density, energy density, capacitance, ESR, and discharge time versus cycle number are displayed in Figure 6.12a-o. According to Figure 6.12, all 14 sets of 6k cycling tests show an improvement in the capacitive

performance over the course of 6k cycles in the form of a decrease in the ESR (potential drop) and/or an increase in the discharge time. These changes are sharp during the transient stage up to around 1000th cycle and steady afterward consistent with the explanation above. A decrease in the potential drop is unfavorable to the capacitance, while an increase in the discharge time is in favor of capacitance according to the formula $C = I\Delta t/(\Delta V - V_{IR})$. Therefore, there is negligible change in capacitance during 6k cycles for all 14 sets of cycling tests, as seen in Figure 6.12a-n. The energy density is increased for all 14 sets of cycling tests since a decrease in the potential drop and an increase in the discharge time are both in favor of the energy density on the basis of the formula $E = 0.5I(\Delta V - V_{IR})\Delta t$. In addition, the power density is increased for all 14 sets of cycling tests since a decrease in the potential drop is in favor of the power density. Overall, the detailed behaviors of all 14 sets of cycling tests indicate the performance recovery during the transient phase followed by very slight variations in capacitive parameters. However, capacitance, energy density, and power density diminish during the 15^{th} 6k cycling test in the form of a decrease in the discharge time and an increase in the ESR (potential drop).

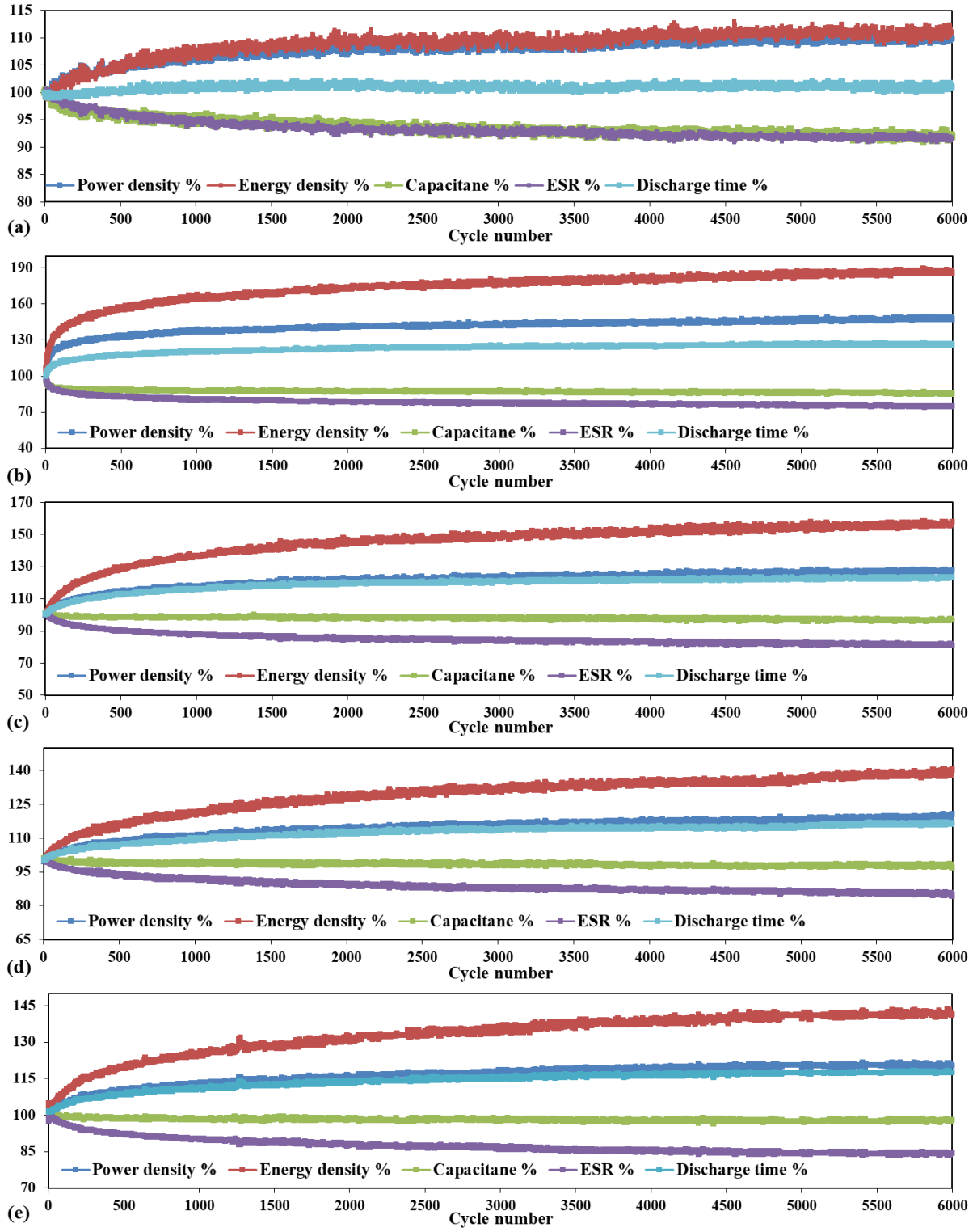
(a)
Power density %
Energy density %
Capacitane %
ESR %
Discharge time %
Cycle number
(b)
Power density %
Energy density %
Capacitane %
ESR %
Discharge time %
Cycle number
(c)
Power density %
Energy density %
Capacitane %
ESR %
Discharge time %
Cycle number
(d)
Power density %
Energy density %
Capacitane %
ESR %
Discharge time %
Cycle number
(e)
Power density %
Energy density %
Capacitane %
ESR %
Discharge time %
Cycle number

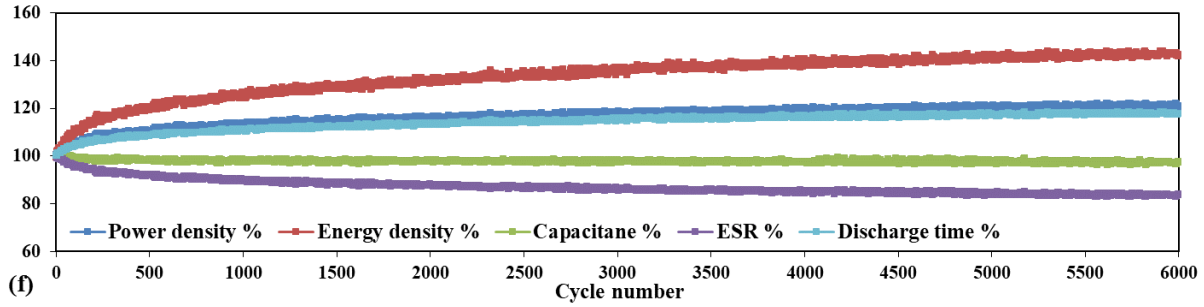
160
140
120
100
80
60
Power density %
Energy density %
Capacitane %
ESR %
Discharge time %
0
500
1000
1500
2000
2500
3000
3500
4000
4500
5000
5500
6000
Cycle number

(f)

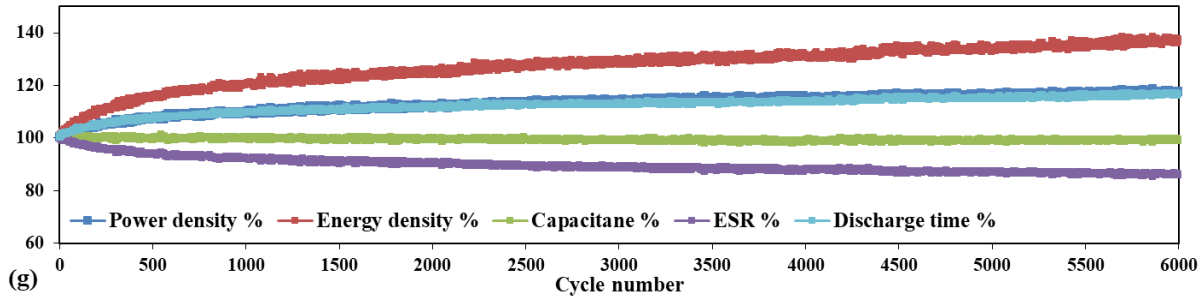
140
120
100
80
60
Power density %
Energy density %
Capacitane %
ESR %
Discharge time %
0
500
1000
1500
2000
2500
3000
3500
4000
4500
5000
5500
6000
Cycle number

(g)

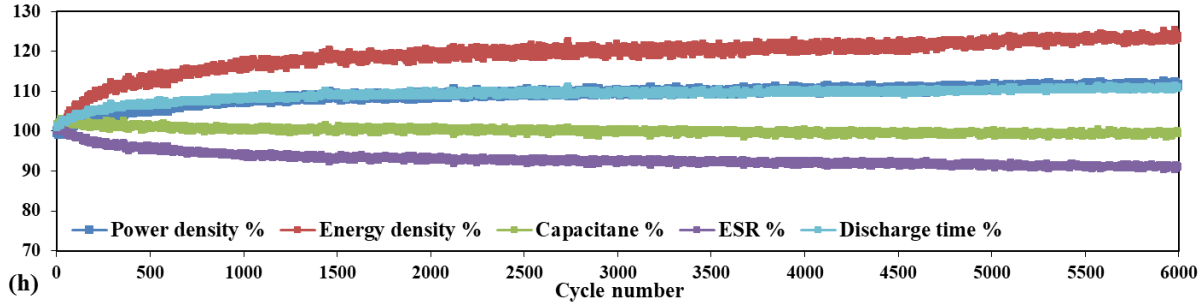
130
120
110
100
90
80
70
Power density %
Energy density %
Capacitane %
ESR %
Discharge time %
0
500
1000
1500
2000
2500
3000
3500
4000
4500
5000
5500
6000
Cycle number

(h)

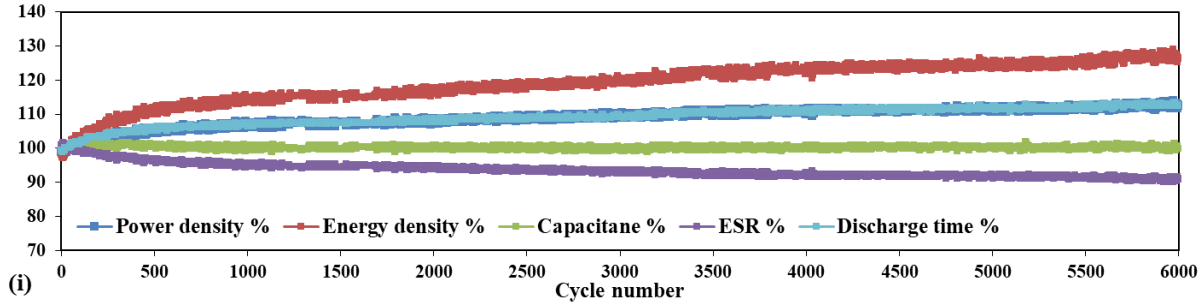
140
130
120
110
100
90
80
70
Power density %
Energy density %
Capacitane %
ESR %
Discharge time %
0
500
1000
1500
2000
2500
3000
3500
4000
4500
5000
5500
6000
Cycle number

(i)

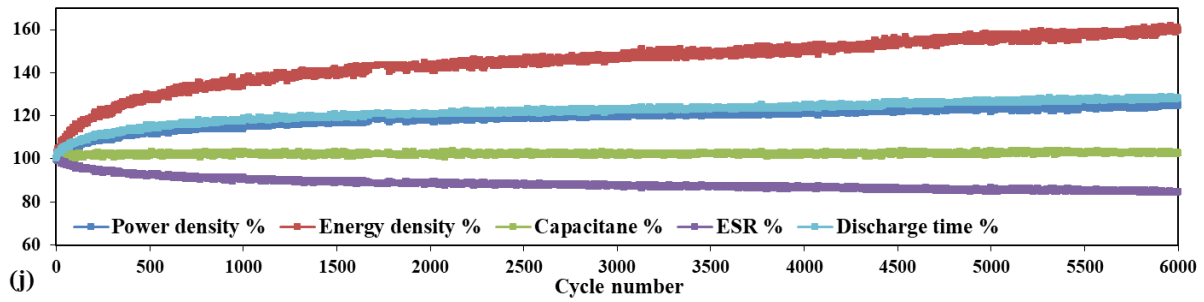
160
140
120
100
80
60
Power density %
Energy density %
Capacitane %
ESR %
Discharge time %
0
500
1000
1500
2000
2500
3000
3500
4000
4500
5000
5500
6000
Cycle number

(j)

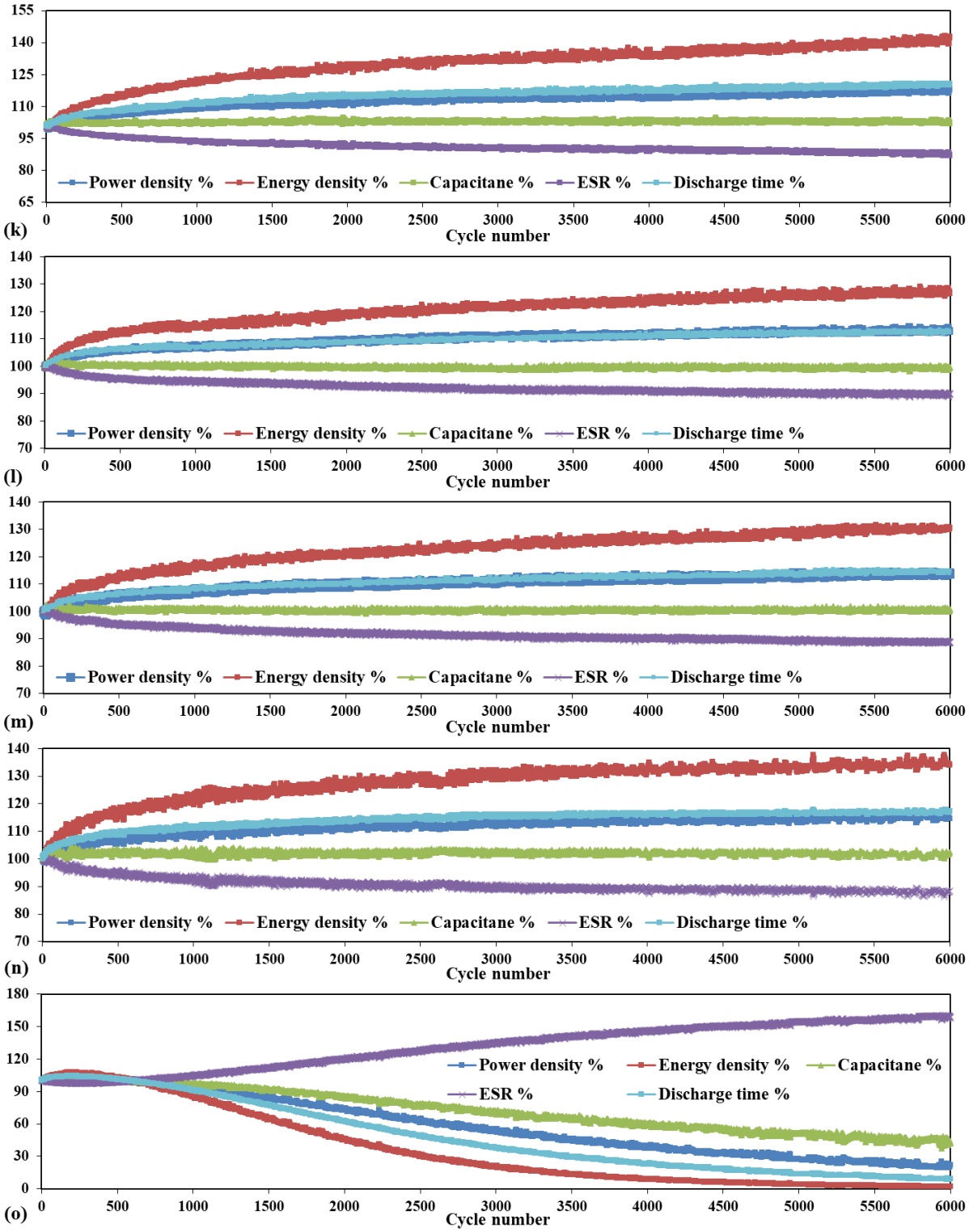

Figure 6.12. Percentages of power density, energy density, capacitance, ESR, and discharge time versus cycle for the assembled PVA/ExG/PAni SC for each 6k cycling test of GCD at 35 mA; (a-o) corresponds to first 6k cycling test to 15th one, respectively.

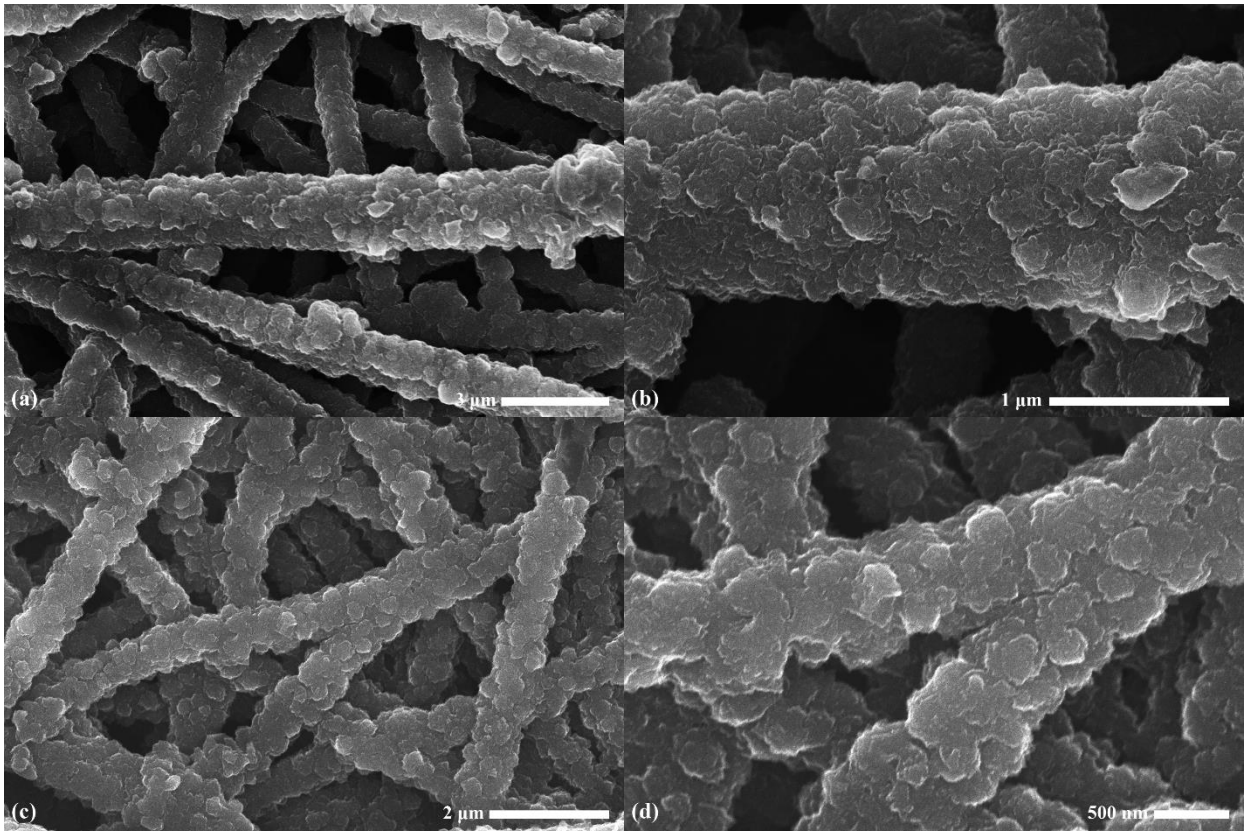

Figure 6.13. SEM images of (a-b) working electrode and (c-d) counter electrode following 90k cycles of GCD at 35 mA.

After the 15th cycling test, the SC was disassembled and the morphology of the electrodes were observed using SEM. According to the morphologies of the working electrode and counter electrode after the cycling test (Figure 6.13), the surface of individual nanofibers are less porous, and thereby confirming the capacitive depletion after the 15th cycling test due to less effective electrolyte penetration. Despite the alternation in nanostructure of the electrodes, the active materials are still well embedded on individual PVA nanofibers. Additionally, the FTIR spectra of the working electrode and counter electrode after 90k cycles of GCD (Figure 6.6) are similar to spectrum of PVA/ExG/PAni film and show all the expected characteristic peaks of PAni. Therefore, the results from the SEM images together with the FTIR spectra imply that the capacitive depletion after the cycling test may be linked to undesirable changes to the morphology of PAni coated on PVA/ExG film.

Interestingly, electrode films after disassembly of SCs show a very rapid acid-base shape memory phenomenon. To illustrate this shape memory behavior that is on basis of difference in pH of the medium, a ribbon is cut from the working electrode of a disassembled SC. The ribbon curls up immediately when it is placed from 1 M H_2SO_4 to 1 M NaOH, and it recovers its original shape upon returning to 1 M H_2SO_4 (Figure 6.14 and video #2). The ribbon goes back to its distinctive shape in the acid or base medium regardless of number of times the process is repeated. In addition, the ribbon retains its original shape (from the acid or base) when it is placed in water. The mechanism is on the basis of the reversible transition between the emeraldine salt form of PAni and the emeraldine base form upon de-protonation (dedoping) in basic solution or protonation (doping) in acidic solution. Upon p-doping the emeraldine base to emeraldine salt by exposing PAni to an acid, PAni chains expand due to the incorporation of counteranions among protonated PAni chains as well as their charge repulsion. Exposing the film to a base solution deprotonates the emeraldine salt and subsequently released counteranions causing PAni to return to its non-swollen form. Herein, there is a nanostructured asymmetry between two surfaces of the electrode films after a long cycling test. In other words, after hundred thousands of charge-discharge cycles, the nanostructure morphology in the side of electrode facing the current collector will be different from the morphology of the side in contact with the separator since the electrolyte is more accessible to the separator side in the assembled SC. Therefore, two sides of the ribbon behave differently when exposed to an acid or base due to their nanostructured asymmetry, causing the ribbon to bending toward one side. This chemical-based actuation is, hence, on the basis of acid expansion and base contraction of PAni together with a nanostructured asymmetry of PAni-based films.

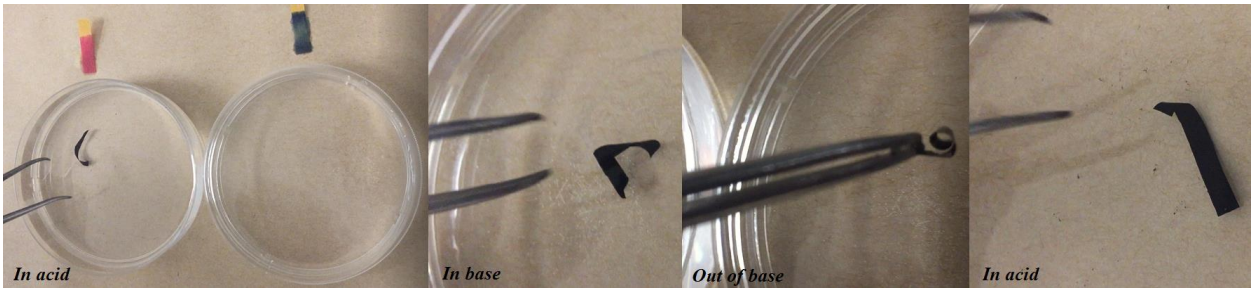

Figure 6.14. The shape memory phenomenon observed for the PVA/ExG/PAni film based on difference in pH of the medium. Due to the nanostructured asymmetry of each side of the ribbon, its curvature changes and it curls up when it is placed from 1 M H_2SO_4 to 1 M NaOH; and it recovers its original shape upon returning to 1 M H_2SO_4 (See video #2).

Inspired by this phenomenon, we construct a PAni-coated PVA film with more coating on one side (asymmetric coating) to further demonstrate acid-base shape memory phenomenon. After performing the *in situ* polymerization of aniline in the presence of PVA mat and H_2SO_4, the green-color and asymmetrically-coated film is scrolled toward the less coated side due to volume expansion of PAni on the side with more coating. When the scrolled film is displaced from 1 M H_2SO_4 to 1 M NaOH, it instantly unrolls and the color changes from green to blue/purple (emeraldine base), and it recovers its original shape and color upon returning to 1 M H_2SO_4 (Figure 6.15a and b, and video #3). Upon exposing to acid/base, the side of the PVA/PAni film with more coating expands/contracts to a greater extent owing to larger amount of PAni, leading to a rapid self-rolling/unrolling. Furthermore, if 1 M NaOH is replaced with a 2M NaOH solution, the film curvature changes even more than that of 1 M NaOH and the film bends toward the more coated side (Figure 6.15c and d, and video #4). The acid-base shape memory behavior of the as-prepared film introduced herein could be utilized in designing chemo-mechanical actuation devices.

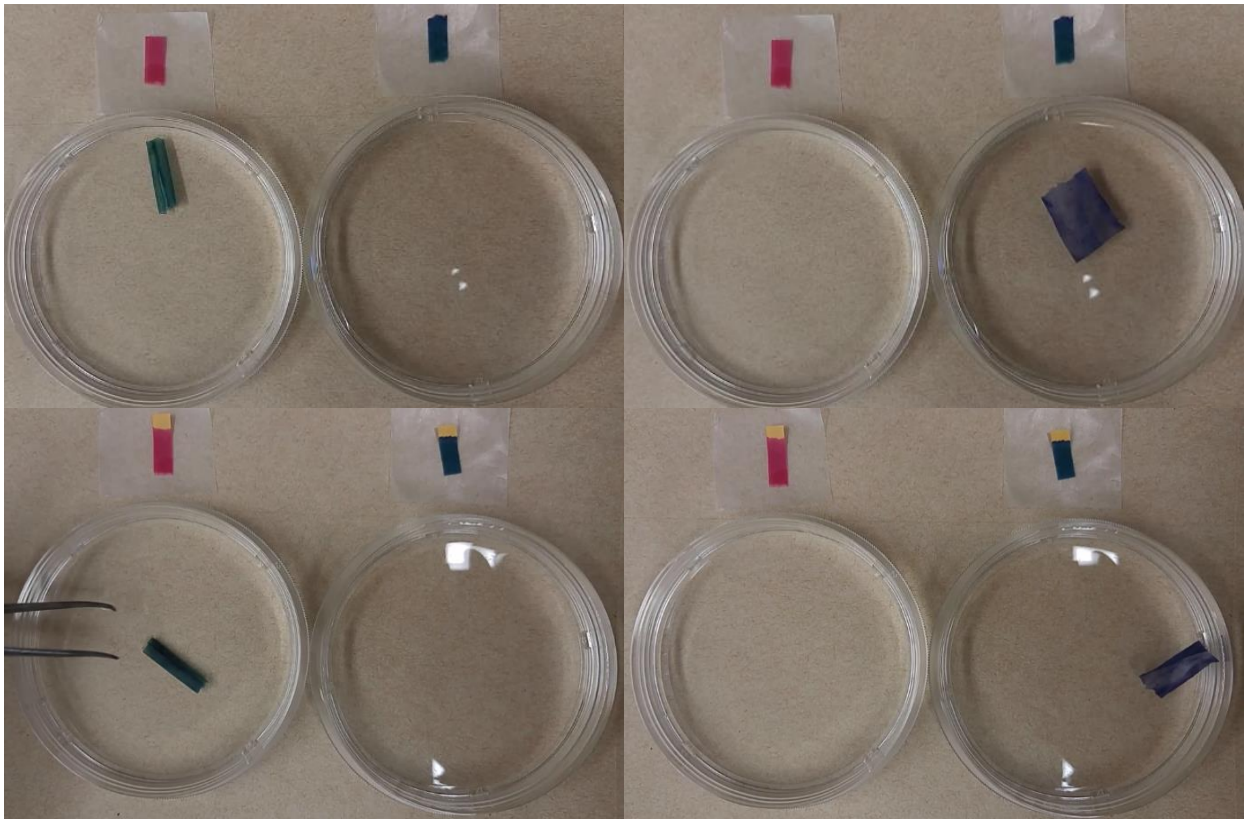

Figure 6.15. The shape memory phenomenon observed for the asymmetrically coated PVA/PAni film based on difference in pH of the medium. (a-b) When the film is displaced from 1 M H_2SO_4 to 1 M NaOH, its curl opens and the color changes from green to blue/purple, and it recovers its original shape upon returning to 1 M H_2SO_4 (See video #3). (c-d) When the film is displaced from 1 M H_2SO_4 to 2M NaOH, its curvature changes even more than that of 1 M NaOH, and it recovers its original shape upon returning to 1 M H_2SO_4 (See video #4).

6.5 Conclusion

In short, a flexible film has been constructed by growing PAni on graphene-coated crosslinked PVA nanofibers to be used as an electrode for SCs with a remarkable cycle life. Scalable electrospinning process of PVA nanofibers together with its wettability, ionic conductance, low cost, chemical stability and flexible nature make it a unique substrate for growing PAni and other redox active conducting polymers. The resulting PVA/PAni and PVA/ExG/PAni films have large surface area and porosity, which are crucial for a high performance electrode material. The results indicate that the assembled SC from PVA/ExG/PAni film shows superior areal-specific

capacitance, areal energy and power densities, and rate capability compared to PVA/PAni film. Moreover, a fabricated SC from the PVA/ExG/PAni film retains its performance for 84k cycles of charge-discharge at 35 mA exhibiting an outstanding cycling performance. The usage of nanofibrous PVA as a cushiony substrate for growing PAni contributes to the long cycle life of the as-prepared SC in three ways. As a soft material, PVA alleviates the stress caused by repeated volume change of PAni during cycling, leading to enhanced structural stability. Moreover, buffer spaces between PVA nanofibers accommodate extra space for volume expansion of PAni. Furthermore, the strong attachment of PAni onto PVA nanofibers offers additional structural stability to PAni. Incorporation of ExG into composite electrode enhances the cycling stability in two ways. As a portion of active materials, graphene enhances the overall stability of the composite electrode. The good affinity between graphene and those PAni chains grown on graphene sheets results in additional structural stability of PAni. In addition to SC application, the PAni-coated PVA film shows a unique acid-base shape memory phenomenon which could be utilized in chemo-mechanical actuation devices

Chapter 7:

Conclusions and Future Work

7.1 Research Summary

In this section, chapters 2-6 are summarized. To provide a generic overview of the research in each chapter, some properties of main SC devices fabricated in chapters 2-6 are presented in Table 7.1. In addition, Figure 7.1 summarizes the key capacitive parameters of main SC devices fabricated in chapters 2-6 to assist comparing capacitive performance of assembled SCs. However, the capacitive parameters of SCs in chapters 2-6 cannot be compared together as each one has a different class of design and electrode materials. The solid-state SC presented in chapter 2 suffers from low rate capability and smaller energy and power densities due to the limited mobility of ions in the gel electrolyte compared to aqueous electrolyte SCs. The electrodes introduced in chapters 3 and 4 can be categorized in a saime class of electrode and they possess a large mass-loading of active materials, and thus their capacitive performances are comparable. The electrodes designed in chapters 5 and 6 can be categorized in a same class of electrode with a small (but adjustable) mass-loading of active materials, and thus their performances are comparable. The summery of research accomplished in each chapter along with their contributions and main conclusions are discussed next.

Table 7.1. The summery of some properties of main SC devices fabricated in chapters 2-6.

Properties	**Chapter 2**	**Chapter 3**	**Chapter 4**	**Chapter 5**	**Chapter 6**
Electrode Materials	PAni, carbon particles, phytic acid	PAni, RGO, cellulose, AgNWs	PAni, ExG, cellulose, AgNPs	PU nanofibers, CNT, PAni	PVA nanofibers, ExG, PAni
Mass loading (mg/cm^2)	13.3	10.7	15-21	1.52	1.46
Electrolyte type	PVA/H_2SO_4 gel electrolyte	Aqueous electrolyte 1 M H_2SO_4	Aqueous electrolyte 1 M H_2SO_4	Aqueous electrolyte 1 M H_2SO_4	Aqueous electrolyte 1 M H_2SO_4
No of cycle tests	500	1500	2000	10,000	90,000

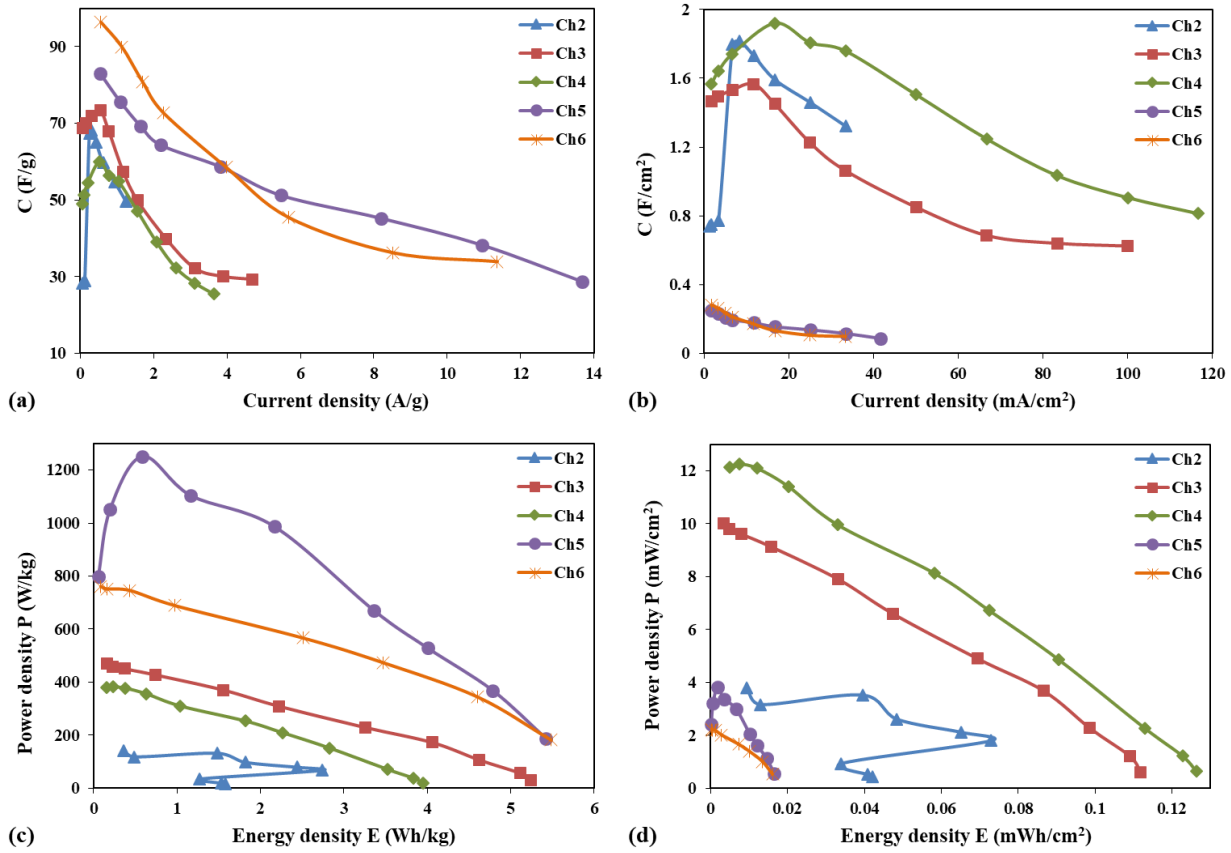

Figure 7.1. The summery of key capacitive parameters of main SC devices fabricated in chapters 2-6. The capacitances, energy and power densities are calculated for the whole SC device.

In Chapter 2, a low-cost PAni-based electrode for solid-state SCs with high energy density and good cycling stability is developed. The electrode is a freestanding composite film of PAni and acid-treated carbon particles using phytic acid as a crosslinker, and the gel electrolyte is composed of sulfuric acid and PVA. TCPs and phytic acid together contribute to obtaining a freestanding composite film that can be used in constructing a flexible solid-state SC. Phytic acid molecule is able to dope several PAni chains resulting in an interconnected nanostructure of PAni. However, such an interaction between phytic acid and PAni chain is still insufficient to prevent degradation of PAni in aqueous acidic electrolytes. Therefore, gel electrolytes is employed herein to address the stability issue of phytic acid-crosslinked PAni. To construct a SC with a high areal specific capacitance, it is required to design an electrode with a large mass-loading of active materials. In a commercial SC, very small quantity of active materials is usually coated on a current collector leading to a low areal specific capacitance. On the other hand, it is infeasible to construct a freestanding electrode from pristine PAni. In this work, however, the combination of TCPs with phytic acid-crosslinked PAni with porous 3D nanostructure makes it possible to construct a film with a large mass-loading of active materials (13.3 mg/cm^2). Hence, a maximum capacitance of 68.2 F/g (1.8 F/cm^2) at a current of 25 mA is achieved for the current SC device, which is larger than values reported for most solid-state SCs in literature. The effective infiltration of the gel electrolyte into the electrodes as well as large mass-loading of active materials also contribute to the high capacitance of the as-prepared SC. The developed thin, flexible, and environmental friendly SC has potential application in wearable energy storage devices.

Chapter 3 reports, for the first time, fabrication of a high-performance SC using a flexible cellulose-based composite film of PAni, RGO and AgNWs. Herein, another strategy is introduced to construct a flexible PAni-based electrode with an adjustable mass-loading of

active materials (10.7 mg/cm^2 herein). Cellulose fibers are utilized as the backbone binding composite materials together and ensure flexibility of the composite film. This strategy also provides a PAni-based composite electrode with a large surface area and porosity owing to the application of cellulose. A common problem with graphene-based composites is that when a graphene dispersion is filtered to make a film, graphene sheets stack onto each other tightly resulting in a film with a low porosity and surface area, which adversely affects the capacitive performance and rate capability. This limitation is addressed herein through usage of cellulose as the backbone of the composite by preventing graphene sheets to restack. Moreover, cellulose effectively absorbs aqueous electrolytes leading to enhanced capacitive performance. The main component of the composite electrode is PAni with a high pseudocapacitance. RGO provides active sites for the growth of PAni as well as excellent electron transfer path, resulting in an enhanced electrochemical performance. AgNWs improve the electrical conductivity and mechanical flexibility of the composite electrode. The as-prepared SC device shows a maximum capacitance of 73.4 F/g (1.6 F/cm^2) at a current of 35 mA. The flexibility, high capacitive behaviour, cycling stability and enhanced rate capability of the composite film make it a good candidate for flexible and wearable SCs.

In chapter 4, a simple and low-cost approach is reported to fabricate a high-performance SC on the basis of a flexible film of PAni, cellulose, ExG and AgNPs. This novel strategy allows designing PAni-based composite electrodes with a very high mass-loading of active materials (15-21 mg/cm^2 herein) as well as large surface area and porosity. In the previous Chapter, AgNWs precipitate in the dispersion due to their relatively heavy weight, resulting in a nonhomogeneous composite film. Herein, AgNPs are directly grown on PAni nanostructure

leading to enhanced conductivity of PAni-based electrodes. In addition, high-quality graphene requires a cumbersome and costly procedure, and thus exfoliated graphite is utilized instead of reduced graphene oxide because of its low cost and high conductivity. ExG is commonly prepared by an electrochemical exfoliation of graphite flakes in aqueous solutions of different inorganic salts [87]. However, the majority of the products on the basis of this method are graphitic particles rather than graphene. To enable mass-production of highly conductive ExG, the current work uses a similar procedure to obtain graphite particles followed by a post-exfoliation in a microwave. In the post-exfoliation process, microwave irradiation of graphite particles causes a further separation of graphene layers and thus large volume expansion of particles. The results demonstrates that the current method yields more conductive ExG compared to the conventional procedure. In this research, the quantity of components are investigated and adjusted to achieve composite electrodes with outstanding electrochemical performances. It is also demonstrated that incorporation of ExG and AgNPs greatly enhance the capacitive performance of the PAni-based composite. The findings show the ratio of ExG/aniline can be tuned to obtain required energy and power densities. For instance, the power density can be increased form 1531.3 W/kg to 3000 W/kg by increasing the weight ratio of ExG/aniline from 0.18 than 0.65, with a sacrifice in the energy density. The results show that an ultrahigh specific capacitance of 1.9 F/cm^2 (60.0 F/g) at a discharge rate of 50 mA for a SC device can be achieved. Overall, this electrode design achieved a combination of enhanced areal capacitance, rate capability and cycling stability for PAni-based SCs. The cycling performance of a SC is commonly investigated by calculating the capacity retention of SCs over a number of cycles. However, observing the capacity change is insufficient to fully evaluate the cycling performance of SCs and it may often mislead

the interpretations. Therefore, for the first time, the cycling performance of power and energy densities is also investigated to provide a more practical criterion.

Chapter 5 reports a new approach to construct a flexible electrode for SCs with an excellent cycling stability by coating flower-like PAni on CNT-reinforced PU nanofibers. This strategy addresses the poor cycle life of PAni and constructs a flexible PAni-based film by growing PAni on a cushiony support. Scalable electrospinning production of PU nanofibers as well as its low cost, chemical resistance and flexible nature make it a great polymer as a substrate for growing PAni as well as other redox active conducting polymers. The *in situ* polymerization of aniline is controlled such that flower-like PAni nanostructure is grown on individual PU nanofibers resulting in a porous film with a large surface area. In addition, mass-loading of PAni on the CNT-reinforced PU nanofibers can be tuned by repeating the coating process. The tests demonstrate that an assembled SC from a film with three coats of PAni exhibits superior areal-specific capacitance, energy and power densities compared to the film with two coats of PAni. The assembled SC from the PU/CNT/PAni film demonstrates a remarkable cycling performance for 10000 cycles of charge-discharge. The long cycle life of the SC is mainly attributed to the employment of the PU substrate that cushions the stress caused by the repeated volume change of PAni during cycling, similar to a mechanical vibration isolator. The strong affinity between grown PAni and PU nanofibers also offers further structural stability. Moreover, buffer spaces between nanofibers accommodate the volume expansion of PAni nanoflowers, and thus attribute to the structural stability of PAni during cycling. Thanks to the procedure introduced in chapter 4 for evaluating cycling behavior of a SC, interesting insights are revealed herein. The cycling test of the assembled SC shows that the cycling behavior has two phases, a transient state and a stable

phase afterward. During the transient phase, the device experiences a sharp changes in the behavior due to the regulation of ion transport to the active sites of electrode materials and regulation of redox reactions of PAni. During the steady-state phase, very slight variations in capacitive behavior is observed.

Finally chapter 6 presents development of a novel flexible electrode with an outstanding cycling stability by growing PAni on ExG-coated cross-linked PVA nanofibers. PVA is an excellent choice as a cushiony support for growing PAni owing to its scalable electrospinning production, chemical stability, wettability, large surface area, and flexible nature. The results demonstrate the assembled SC from PVA/ExG/PAni film exhibits superior areal-specific capacitance, areal energy and power densities, and rate capability compared to PVA/PAni film. The SC constructed from a flexible PVA/ExG/PAni film maintains its capacitive performance for 84k cycles of charge-discharge at 35 mA showing an unprecedented cycle life. The prolonged cycle life of the SC herein is attributed to the combination of three factors: (a) nanofibrous PVA alleviates the stress induced by repeated volume change of PAni during charge-discharge cycling resulting in an enhanced structural stability of PAni; (b) the strong attachment of PAni onto PVA nanofibers and ExG provides additional structural stability to PAni; and (c) buffer spaces between PVA nanofibers accommodate extra space required during volume expansion of PAni. It should be noted that ExG is employed as an inexpensive source of graphene to enhance the capacitive performance of PAni. As a portion of active materials, ExG improves the overall stability of the composite electrode. In addition, the strong affinity between graphene and those PAni nanowires coated on graphene sheets enhances the structural stability of PAni leading to improved cycling stability. In addition to being a novel flexible electrode for SC application, the

PVA/ExG/PAni film displays a rapid shape memory phenomenon on the basis of expansion and contraction of PAni upon doping in an acid and dedoping in a base. Inspired by this phenomenon, a PAni-coated PVA film with more coating on one side is constructed to further demonstrate the acid-base shape memory behavior. The green-color and asymmetrically-coated film is scrolled toward the less coated side due to volume expansion of PAni on the side with more coating. When the rolled film is placed into 1 M NaOH, it instantly unrolls and the color changes from green to blue/purple (emeraldine base), and it recovers its original shape and color upon returning to 1 M H_2SO_4. The unique shape memory behavior of the PVA/PAni film introduced herein could be utilized in designing chemo-mechanical actuation devices.

7.2 Recommendations for Future Work

The solid-state SC developed in chapter 2 employed a gel electrolyte to address the poor cycle life of PAni. The limitation of the gel electrolyte is its smaller ionic conductivity compared to aqueous electrolytes and thus a solid-state SC will have an inferior rate capability. Hence, designing a gel electrolyte with higher ionic conductivity or utilizing ionic liquids that are also compatible with PAni is a potential direction for future research. One advantage of a solid-state SC is the ability to be operated in a large potential window (e.g. 3 V). However, a PAni-based SC cannot be charged-discharged in a large potential window as there will be permanent damage to the PAni structure. Future research can explore ways to widen operating potential window for PAni-based electrodes. In chapter 3, a new strategy is introduced to incorporate PAni, cellulose, RGO, and AgNWs into a flexible composite electrode. Future research can optimize the relative quantity of PAni, RGO, and AgNWs to attain the best possible capacitive performance. Furthermore, AgNWs precipitate from the dispersion due to their relatively heavy weight, resulting in a nonhomogeneous

composite film. This limitation can be addressed in future by adjusting the preparation protocol of AgNWs to obtain AgNWs with smaller diameter, which could lead to a better dispersion.

A commercial tissue wiper is utilized as a cheap source of cellulose to prepare nano-cellulose in chapters 2 and 3. The resulting disintegrated cellulose contains microfibers, nanofibers, and nanosheets. Alternatively, high-quality cellulose nanofibers can be prepared from various cellulose sources such as hemp and other plants. Application of cellulose nanofibers in PAni-based composites may result in films with better mechanical properties. Moreover, transparent films can be constructed from cellulose nanofibers.

In chapters 5 and 6, electrospun polymer nanofibers are utilized as substrates for growing PAni to construct flexible electrodes. The capacitive performance of an electrode is highly related to its surface area and porosity. One possible future direction is adjusting the electrospinning process to attain polymer nanofibers with appropriate surface area and porosity to maximize the capacitive performance of the final composite electrode. The PU and PVA nanofibers introduced in chapters 5 and 6 as supports for growing PAni can also be employed for the deposition of other redox-active conducting polymers and metal oxides. The electrospun PVA film has also the potential application as a separator of a SC owing to its water wettability and excellent chemical stability.

Various approaches are explored to construct PAni-based flexible electrodes in chapters 3-6. Future research could be focused on developing wearable SCs using as-prepared flexible electrodes. Another direction could be investigating the operating temperature ranges for the as-prepared SCs introduced in chapters 3-6.

Another important performance factor for a SC performance, which is not investigated in this thesis, is the investigation of the self-discharge of a SC. A SC with a large self-discharge rate is of little practical application because of the fast loss of the stored charge.

PAni has several features that can be utilized in various kinds of sensors such as gas and chemical sensing. The PAni-based flexible films introduced in chapters 5 and 6 are light weight with high flexibility and durability suitable for wearable sensors. A wearable PAni-based sensor can be realized by utilizing Bluetooth Low Energy module to make a wireless sensor. Hence, the potential sensor application of these PAni-based flexible films are yet to be investigated in future. As shown in Figure 6.15, the PVA/PAni film changes its color from green to blue/purple when exposed to a basic medium. The film could be used inside a fish package to change color upon spoilage of the fish (exposing to ammonia).

Another possible research direction can be further study of the acid-base shape memory phenomenon introduced in chapter 6 and its utilization for chemo-mechanical actuation devices.

Bibliography

(1) Khosrozadeh, A.; Xing, M.; Wang, Q., A High-Capacitance Solid-State Supercapacitor Based on Free-Standing Film of Polyaniline and Carbon Particles. *Appl. Energy* 2015**,** *153* (0), 87-93.

(2) Aiping Yu, V. C., Jiujun Zhang *Electrochemical Supercapacitors for Energy Storage and Delivery: Fundamentals and Applications*. CRC Press: **2013**.

(3) Winter, M.; Brodd, R. J., What Are Batteries, Fuel Cells, and Supercapacitors? *Chem. Rev.* 2004**,** *104* (10), 4245-4270.

(4) Zhang, L. L.; Zhou, R.; Zhao, X. S., Graphene-Based Materials as Supercapacitor Electrodes. *J. Mater. Chem.* 2010**,** *20* (29), 5983-5992.

(5) Simon, P.; Gogotsi, Y., Materials for electrochemical capacitors. *Nat Mater* 2008**,** *7* (11), 845-854.

(6) Choudhary, N.; Li, C.; Moore, J.; Nagaiah, N.; Zhai, L.; Jung, Y.; Thomas, J., Asymmetric Supercapacitor Electrodes and Devices. *Advanced Materials* 2017**,** *29* (21), n/a-n/a.

(7) Simon, P.; Gogotsi, Y.; Dunn, B., Where Do Batteries End and Supercapacitors Begin? *Science* 2014**,** *343* (6176), 1210-1211.

(8) Zhong, C.; Deng, Y.; Hu, W.; Qiao, J.; Zhang, L.; Zhang, J., A review of electrolyte materials and compositions for electrochemical supercapacitors. *Chemical Society Reviews* 2015**,** *44* (21), 7484-7539.

(9) Conway, B. E.; Pell, W. G., Double-layer and pseudocapacitance types of electrochemical capacitors and their applications to the development of hybrid devices. *Journal of Solid State Electrochemistry* 2003**,** *7* (9), 637-644.

(10) Zhang, L. L.; Zhao, X. S., Carbon-Based Materials as Supercapacitor Electrodes. *Chem. Soc. Rev.* 2009**,** *38* (9), 2520-2531.

(11) Wang, K.; Zhao, P.; Zhou, X.; Wu, H.; Wei, Z., Flexible supercapacitors based on cloth-supported electrodes of conducting polymer nanowire array/SWCNT composites. *J. Mater. Chem.* 2011**,** *21* (41), 16373-16378.

(12) Wang, G.; Zhang, L.; Zhang, J., A review of electrode materials for electrochemical supercapacitors. *Chem. Soc. Rev.* 2012**,** *41* (2), 797-828.

(13) Snook, G. A.; Kao, P.; Best, A. S., Conducting-polymer-based supercapacitor devices and electrodes. *J. Power Sources* 2011**,** *196* (1), 1-12.

(14) Conway, B. E.; Birss, V.; Wojtowicz, J., The role and utilization of pseudocapacitance for energy storage by supercapacitors. *Journal of Power Sources* 1997**,** *66* (1), 1-14.

(15) Halper, M. S.; Ellenbogen, J. C. *Supercapacitors: A Brief Overview*; MITRE Nanosystems Group: **March 2006**.

(16) Supercapacitor. http://en.wikipedia.org/wiki/Supercapacitor.

(17) Feast, W. J.; Tsibouklis, J.; Pouwer, K. L.; Groenendaal, L.; Meijer, E. W., Synthesis, processing and material properties of conjugated polymers. *Polymer* 1996**,** *37* (22), 5017-5047.

(18) Ramya, R.; Sivasubramanian, R.; Sangaranarayanan, M. V., Conducting polymers-based electrochemical supercapacitors-Progress and prospects. *Electrochimica Acta* 2013**,** *101* (0), 109-129.

(19) Huang, J.; Kaner, R. B., Nanofiber Formation in the Chemical Polymerization of Aniline: A Mechanistic Study. *Angewandte Chemie International Edition* 2004**,** *43* (43), 5817-5821.

(20) Huang, J.; Virji, S.; Weiller, B. H.; Kaner, R. B., Polyaniline Nanofibers: Facile Synthesis and Chemical Sensors. *J. Am. Chem. Soc.* 2003**,** *125* (2), 314-315.

(21) Huang, J.; Kaner, R. B., A General Chemical Route to Polyaniline Nanofibers. *Journal of the American Chemical Society* 2004**,** *126* (3), 851-855.

(22) Gospodinova, N.; Terlemezyan, L., Conducting polymers prepared by oxidative polymerization: polyaniline. *Progress in Polymer Science* 1998**,** *23* (8), 1443-1484.

(23) Zhang, D.; Wang, Y., Synthesis and applications of one-dimensional nano-structured polyaniline: An overview. *Materials Science and Engineering: B* 2006**,** *134* (1), 9-19.

(24) Ćirić-Marjanović, G., Recent advances in polyaniline research: Polymerization mechanisms, structural aspects, properties and applications. *Synthetic Metals* 2013**,** *177*, 1-47.

(25) Sapurina, I. Y.; Shishov, M. A., Oxidative Polymerization of Aniline: Molecular Synthesis of Polyaniline and the Formation of Supramolecular Structures. In *New Polymers for Special Applications*, Gomes, A. D. S., Ed. InTech: Rijeka, **2012**, p Ch. 09.

(26) Park, J. H.; Park, O. O., Hybrid electrochemical capacitors based on polyaniline and activated carbon electrodes. *J. Power Sources* 2002**,** *111* (1), 185-190.

(27) Khosrozadeh, A.; Darabi, M. A.; Wang, Q.; Xing, M., Polyaniline nanoflowers grown on vibration-isolator-mimetic polyurethane nanofibers for flexible supercapacitors with prolonged cycle life. *Journal of Materials Chemistry A* 2017**,** *5* (17), 7933-7943.

(28) Khosrozadeh, A.; Darabi, M. A.; Xing, M.; Wang, Q., Flexible Electrode Design: Fabrication of Freestanding Polyaniline-Based Composite Films for High-Performance Supercapacitors. *ACS Appl. Mater. Interfaces* 2016**,** *8* (18), 11379-11389.

(29) Chen, K.; Song, S.; Liu, F.; Xue, D., Structural design of graphene for use in electrochemical energy storage devices. *Chemical Society Reviews* 2015**,** *44* (17), 6230-6257.

(30) Ji, L.; Meduri, P.; Agubra, V.; Xiao, X.; Alcoutlabi, M., Graphene-Based Nanocomposites for Energy Storage. *Advanced Energy Materials* 2016**,** *6* (16), n/a-n/a.

(31) Pei, S.; Cheng, H.-M., The reduction of graphene oxide. *Carbon* 2012**,** *50* (9), 3210-3228.

(32) Kovtyukhova, N. I.; Ollivier, P. J.; Martin, B. R.; Mallouk, T. E.; Chizhik, S. A.; Buzaneva, E. V.; Gorchinskiy, A. D., Layer-by-Layer Assembly of Ultrathin Composite Films from Micron-Sized Graphite Oxide Sheets and Polycations. *Chemistry of Materials* 1999**,** *11* (3), 771-778.

(33) Hummers, W. S.; Offeman, R. E., Preparation of Graphitic Oxide. *Journal of the American Chemical Society* 1958**,** *80* (6), 1339-1339.

(34) Hirata, M.; Gotou, T.; Horiuchi, S.; Fujiwara, M.; Ohba, M., Thin-film particles of graphite oxide 1:: High-yield synthesis and flexibility of the particles. *Carbon* 2004**,** *42* (14), 2929-2937.

(35) Wu, Z.-S.; Ren, W.; Gao, L.; Liu, B.; Jiang, C.; Cheng, H.-M., Synthesis of high-quality graphene with a pre-determined number of layers. *Carbon* 2009**,** *47* (2), 493-499.

(36) Zhao, J.; Pei, S.; Ren, W.; Gao, L.; Cheng, H.-M., Efficient Preparation of Large-Area Graphene Oxide Sheets for Transparent Conductive Films. *ACS Nano* 2010**,** *4* (9), 5245-5252.

(37) Marcano, D. C.; Kosynkin, D. V.; Berlin, J. M.; Sinitskii, A.; Sun, Z.; Slesarev, A.; Alemany, L. B.; Lu, W.; Tour, J. M., Improved Synthesis of Graphene Oxide. *ACS Nano* 2010**,** *4* (8), 4806-4814.

(38) Stankovich, S.; Dikin, D. A.; Piner, R. D.; Kohlhaas, K. A.; Kleinhammes, A.; Jia, Y.; Wu, Y.; Nguyen, S. T.; Ruoff, R. S., Synthesis of graphene-based nanosheets via chemical reduction of exfoliated graphite oxide. *Carbon* 2007**,** *45* (7), 1558-1565.

(39) Pei, S.; Zhao, J.; Du, J.; Ren, W.; Cheng, H.-M., Direct reduction of graphene oxide films into highly conductive and flexible graphene films by hydrohalic acids. *Carbon* 2010**,** *48* (15), 4466-4474.

(40) Fernández-Merino, M. J.; Guardia, L.; Paredes, J. I.; Villar-Rodil, S.; Solís-Fernández, P.; Martínez-Alonso, A.; Tascón, J. M. D., Vitamin C Is an Ideal Substitute for Hydrazine in the Reduction of Graphene Oxide Suspensions. *The Journal of Physical Chemistry C* 2010**,** *114* (14), 6426-6432.

(41) Gao, W.; Alemany, L. B.; Ci, L.; Ajayan, P. M., New insights into the structure and reduction of graphite oxide. *Nat Chem* 2009**,** *1* (5), 403-408.

(42) Jang, J.; Bae, J.; Choi, M.; Yoon, S.-H., Fabrication and Characterization of Polyaniline Coated Carbon Nanofiber for Supercapacitor. *Carbon* 2005**,** *43* (13), 2730-2736.

(43) Wang, Y. G.; Li, H. Q.; Xia, Y. Y., Ordered Whiskerlike Polyaniline Grown on the Surface of Mesoporous Carbon and Its Electrochemical Capacitance Performance. *Adv. Mater.* 2006**,** *18* (19), 2619-2623.

(44) Zhou, Y.-k.; He, B.-l.; Zhou, W.-j.; Huang, J.; Li, X.-h.; Wu, B.; Li, H.-l., Electrochemical capacitance of well-coated single-walled carbon nanotube with polyaniline composites. *Electrochimica Acta* 2004**,** *49* (2), 257-262.

(45) Frackowiak, E.; Khomenko, V.; Jurewicz, K.; Lota, K.; Béguin, F., Supercapacitors based on conducting polymers/nanotubes composites. *Journal of Power Sources* 2006**,** *153* (2), 413-418.

(46) Zhang, H.; Cao, G.; Wang, Z.; Yang, Y.; Shi, Z.; Gu, Z., Tube-covering-tube nanostructured polyaniline/carbon nanotube array composite electrode with high capacitance and superior rate performance as well as good cycling stability. *Electrochem. Commun.* 2008**,** *10* (7), 1056-1059.

(47) Meng, C.; Liu, C.; Chen, L.; Hu, C.; Fan, S., Highly Flexible and All-Solid-State Paperlike Polymer Supercapacitors. *Nano Lett.* 2010**,** *10* (10), 4025-4031.

(48) Zhang, J.; Kong, L.-B.; Wang, B.; Luo, Y.-C.; Kang, L., In-situ electrochemical polymerization of multi-walled carbon nanotube/polyaniline composite films for electrochemical supercapacitors. *Synthetic Metals* 2009**,** *159* (3â€“4), 260-266.

(49) Gao, Z.; Yang, W.; Wang, J.; Yan, H.; Yao, Y.; Ma, J.; Wang, B.; Zhang, M.; Liu, L., Electrochemical synthesis of layer-by-layer reduced graphene oxide sheets/polyaniline nanofibers composite and its electrochemical performance. *Electrochimica Acta* 2013**,** *91* (0), 185-194.

(50) Yan, J.; Wei, T.; Shao, B.; Fan, Z.; Qian, W.; Zhang, M.; Wei, F., Preparation of a Graphene Nanosheet/Polyaniline Composite with High Specific Capacitance. *Carbon* 2010**,** *48* (2), 487-493.

(51) Wu, Q.; Xu, Y.; Yao, Z.; Liu, A.; Shi, G., Supercapacitors Based on Flexible Graphene/Polyaniline Nanofiber Composite Films. *ACS Nano* 2010**,** *4* (4), 1963-1970.

(52) Wang, H.; Hao, Q.; Yang, X.; Lu, L.; Wang, X., A Nanostructured Graphene/Polyaniline Hybrid Material for Supercapacitors. *Nanoscale* 2010**,** *2* (10), 2164-2170.

(53) Xu, J.; Wang, K.; Zu, S.-Z.; Han, B.-H.; Wei, Z., Hierarchical Nanocomposites of Polyaniline Nanowire Arrays on Graphene Oxide Sheets with Synergistic Effect for Energy Storage. *ACS Nano* 2010**,** *4* (9), 5019-5026.

(54) Mao, L.; Zhang, K.; On Chan, H. S.; Wu, J., Surfactant-Stabilized Graphene/Polyaniline Nanofiber Composites for High Performance Supercapacitor Electrode. *J. Mater. Chem.* 2012**,** *22* (1), 80-85.

(55) Meng, Y.; Wang, K.; Zhang, Y.; Wei, Z., Hierarchical Porous Graphene/Polyaniline Composite Film with Superior Rate Performance for Flexible Supercapacitors. *Adv. Mater.* 2013**,** *25* (48), 6985-6990.

(56) Yu, P.; Zhao, X.; Huang, Z.; Li, Y.; Zhang, Q., Free-Standing Three-Dimensional Graphene and Polyaniline Nanowire Arrays Hybrid Foams for High-Performance Flexible and Lightweight Supercapacitors. *J. Mater. Chem. A* 2014**,** *2* (35), 14413-14420.

(57) Liu, X.; Shang, P.; Zhang, Y.; Wang, X.; Fan, Z.; Wang, B.; Zheng, Y., Three-Dimensional and Stable Polyaniline-Grafted Graphene Hybrid Materials for Supercapacitor Electrodes. *J. Mater. Chem. A* 2014**,** *2* (37), 15273-15278.

(58) Li, L.; Raji, A.-R. O.; Fei, H.; Yang, Y.; Samuel, E. L. G.; Tour, J. M., Nanocomposite of Polyaniline Nanorods Grown on Graphene Nanoribbons for Highly Capacitive Pseudocapacitors. *ACS Appl. Mater. Interfaces* 2013**,** *5* (14), 6622-6627.

(59) Yan, X.; Tai, Z.; Chen, J.; Xue, Q., Fabrication of carbon nanofiber-polyaniline composite flexible paper for supercapacitor. *Nanoscale* 2011**,** *3* (1), 212-216.

(60) Zhi, M.; Xiang, C.; Li, J.; Li, M.; Wu, N., Nanostructured carbon-metal oxide composite electrodes for supercapacitors: a review. *Nanoscale* 2013**,** *5* (1), 72-88.

(61) Li, D.; Muller, M. B.; Gilje, S.; Kaner, R. B.; Wallace, G. G., Processable aqueous dispersions of graphene nanosheets. *Nat Nano* 2008**,** *3* (2), 101-105.

(62) Zhang, S.; Pan, N., Supercapacitors Performance Evaluation. *Adv. Energy Mater.* 2015**,** *5* (6).

(63) Stoller, M. D.; Ruoff, R. S., Best practice methods for determining an electrode material's performance for ultracapacitors. *Energy Environ. Sci.* 2010**,** *3* (9), 1294-1301.

(64) Zhang, J.; Zhao, X. S., On the Configuration of Supercapacitors for Maximizing Electrochemical Performance. *ChemSusChem* 2012**,** *5* (5), 818-841.

(65) Khosrozadeh, A.; Darabi, M. A.; Xing, M.; Wang, Q., Flexible Cellulose-Based Films of Polyaniline–Graphene–Silver Nanowire for High-Performance Supercapacitors. *J. Nanotechnol. Eng. Med.* 2015**,** *6* (1), 011005-011005.

(66) Blighe, F. M.; Diamond, D.; Coleman, J. N.; Lahiff, E., Increased response/recovery lifetimes and reinforcement of polyaniline nanofiber films using carbon nanotubes. *Carbon* 2012**,** *50* (4), 1447-1454.

(67) Long, Y.; Chen, Z.; Zhang, X.; Zhang, J.; Liu, Z., Synthesis and electrical properties of carbon nanotube polyaniline composites. *Applied Physics Letters* 2004**,** *85* (10), 1796-1798.

(68) Wang, S.; Pei, B.; Zhao, X.; Dryfe, R. A. W., Highly porous graphene on carbon cloth as advanced electrodes for flexible all-solid-state supercapacitors. *Nano Energy* 2013**,** *2* (4), 530-536.

(69) Pan, L.; Yu, G.; Zhai, D.; Lee, H. R.; Zhao, W.; Liu, N.; Wang, H.; Tee, B. C. K.; Shi, Y.; Cui, Y.; Bao, Z., Hierarchical nanostructured conducting polymer hydrogel with high electrochemical activity. *Proc. Natl. Acad. Sci.* 2012**,** *109* (24), 9287-9292.

(70) Peng, J.; Gao, W.; Gupta, B. K.; Liu, Z.; Romero-Aburto, R.; Ge, L.; Song, L.; Alemany, L. B.; Zhan, X.; Gao, G.; Vithayathil, S. A.; Kaipparettu, B. A.; Marti, A. A.; Hayashi, T.; Zhu, J.-J.; Ajayan, P. M., Graphene Quantum Dots Derived from Carbon Fibers. *Nano Letters* 2012**,** *12* (2), 844-849.

(71) Xu, Y.; Lin, Z.; Huang, X.; Liu, Y.; Huang, Y.; Duan, X., Flexible Solid-State Supercapacitors Based on Three-Dimensional Graphene Hydrogel Films. *ACS Nano* 2013**,** *7* (5), 4042-4049.

(72) El-Kady, M. F.; Strong, V.; Dubin, S.; Kaner, R. B., Laser scribing of high-performance and flexible graphene-based electrochemical capacitors. *Science* 2012**,** *335* (6074), 1326-1330.

(73) Kaempgen, M.; Chan, C. K.; Ma, J.; Cui, Y.; Gruner, G., Printable Thin Film Supercapacitors Using Single-Walled Carbon Nanotubes. *Nano Letter* 2009**,** *9* (5), 1872-1876.

(74) Yuan, L.; Yao, B.; Hu, B.; Huo, K.; Chen, W.; Zhou, J., Polypyrrole-coated paper for flexible solid-state energy storage. *Energy & Environmental Science* 2013**,** *6* (2), 470-476.

(75) Chen, J.; Bi, H.; Sun, S.; Tang, Y.; Zhao, W.; Lin, T.; Wan, D.; Huang, F.; Zhou, X.; Xie, X.; Jiang, M., Highly Conductive and Flexible Paper of 1D Silver-Nanowire-Doped Graphene. *ACS Applied Materials & Interfaces* 2013**,** *5* (4), 1408-1413.

(76) Liu, S.; Weng, B.; Tang, Z.-R.; Xu, Y.-J., Constructing one-dimensional silver nanowire-doped reduced graphene oxide integrated with CdS nanowire network hybrid structures toward artificial photosynthesis. *Nanoscale* 2015**,** *7* (3), 861-866.

(77) Zhang, W. C.; Wu, X. L.; Chen, H. T.; Gao, Y. J.; Zhu, J.; Huang, G. S.; Chu, P. K., Self-organized formation of silver nanowires, nanocubes and bipyramids via a solvothermal method. *Acta Materialia* 2008**,** *56* (11), 2508-2513.

(78) Roy, D.; Semsarilar, M.; Guthrie, J. T.; Perrier, S., Cellulose Modification by Polymer Grafting: a Review. *Chem. Soc. Rev.* 2009**,** *38* (7), 2046-2064.

(79) Miao, C.; Hamad, W., Cellulose Reinforced Polymer Composites and Nanocomposites: a Critical Review. *Cellulose* 2013**,** *20* (5), 2221-2262.

(80) Zhang, X.; Lin, Z.; Chen, B.; Zhang, W.; Sharma, S.; Gu, W.; Deng, Y., Solid-State Flexible Polyaniline/Silver Cellulose Nanofibrils Aerogel Supercapacitors. *J. Power Sources* 2014**,** *246* (0), 283-289.

(81) Shi, X.; Hu, Y.; Li, M.; Duan, Y.; Wang, Y.; Chen, L.; Zhang, L., Highly Specific Capacitance Materials Constructed via in Situ Synthesis of Polyaniline in a Cellulose Matrix for Supercapacitors. *Cellulose* 2014**,** *21* (4), 2337-2347.

(82) Mahmood, N.; Zhang, C.; Yin, H.; Hou, Y., Graphene-Based Nanocomposites for Energy Storage and Conversion in Lithium Batteries, Supercapacitors and Fuel Cells. *J. Mater. Chem. A* 2014**,** *2* (1), 15-32.

(83) Liu, N.; Luo, F.; Wu, H.; Liu, Y.; Zhang, C.; Chen, J., One-Step Ionic-Liquid-Assisted Electrochemical Synthesis of Ionic-Liquid-Functionalized Graphene Sheets Directly from Graphite. *Adv. Funct. Mater.* 2008**,** *18* (10), 1518-1525.

(84) Lee, J. H.; Shin, D. W.; Makotchenko, V. G.; Nazarov, A. S.; Fedorov, V. E.; Kim, Y. H.; Choi, J.-Y.; Kim, J. M.; Yoo, J.-B., One-Step Exfoliation Synthesis of Easily Soluble Graphite and Transparent Conducting Graphene Sheets. *Adv. Mater.* 2009**,** *21* (43), 4383-4387.

(85) Su, C.-Y.; Lu, A.-Y.; Xu, Y.; Chen, F.-R.; Khlobystov, A. N.; Li, L.-J., High-Quality Thin Graphene Films from Fast Electrochemical Exfoliation. *ACS Nano* 2011**,** *5* (3), 2332-2339.

(86) Parvez, K.; Li, R.; Puniredd, S. R.; Hernandez, Y.; Hinkel, F.; Wang, S.; Feng, X.; Müllen, K., Electrochemically Exfoliated Graphene as Solution-Processable, Highly Conductive Electrodes for Organic Electronics. *ACS Nano* 2013**,** *7* (4), 3598-3606.

(87) Parvez, K.; Wu, Z.-S.; Li, R.; Liu, X.; Graf, R.; Feng, X.; Müllen, K., Exfoliation of Graphite into Graphene in Aqueous Solutions of Inorganic Salts. *J. Am. Chem. Soc.* 2014**,** *136* (16), 6083-6091.

(88) Xia, L.; Zhao, C.; Yan, X.; Wu, Z., High Conductivity of Polyaniline-Silver Synthesized in Situ by Additional Reductant. *J. Appl. Polym. Sci.* 2013**,** *130* (1), 394-398.

(89) Sawangphruk, M.; Suksomboon, M.; Kongsupornsak, K.; Khuntilo, J.; Srimuk, P.; Sanguansak, Y.; Klunbud, P.; Suktha, P.; Chiochan, P., High-Performance Supercapacitors Based on Silver Nanoparticle-Polyaniline-Graphene Nanocomposites Coated on Flexible Carbon Fiber Paper. *J. Mater. Chem. A* 2013**,** *1* (34), 9630-9636.

(90) Li, J.; Liu, L.; Zhang, D.; Yang, D.; Guo, J.; Wei, J., Fabrication of Polyaniline/Silver Nanoparticles/Multi-Walled Carbon Nanotubes Composites for Flexible Microelectronic Circuits. *Synth. Met.* 2014**,** *192* (0), 15-22.

(91) Dhibar, S.; Das, C. K., Silver Nanoparticles Decorated Polyaniline/Multiwalled Carbon Nanotubes Nanocomposite for High-Performance Supercapacitor Electrode. *Ind. Eng. Chem. Res.* 2014**,** *53* (9), 3495-3508.

(92) Bober, P.; Stejskal, J.; Trchová, M.; Prokeš, J., In-Situ Prepared Polyaniline–Silver Composites: Single- and Two-Step Strategies. *Electrochim. Acta* 2014**,** *122* (0), 259-266.

(93) Shi, S.; Xu, C.; Yang, C.; Li, J.; Du, H.; Li, B.; Kang, F., Flexible Supercapacitors. *Particuology* 2013**,** *11* (4), 371-377.

(94) Li, L.; Wu, Z.; Yuan, S.; Zhang, X.-B., Advances and Challenges for Flexible Energy Storage and Conversion Devices and Systems. *Energy Environ. Sci.* 2014**,** *7* (7), 2101-2122.

(95) Du, X. S.; Xiao, M.; Meng, Y. Z., Facile Synthesis of Highly Conductive Polyaniline/Graphite Nanocomposites. *Eur. Polym. J.* 2004**,** *40* (7), 1489-1493.

(96) Zhu, Y.; Murali, S.; Stoller, M. D.; Velamakanni, A.; Piner, R. D.; Ruoff, R. S., Microwave Assisted Exfoliation and Reduction of Graphite Oxide for Ultracapacitors. *Carbon* 2010**,** *48* (7), 2118-2122.

(97) Cong, H.-P.; Ren, X.-C.; Wang, P.; Yu, S.-H., Flexible Graphene-Polyaniline Composite Paper for High-Performance Supercapacitor. *Energy Environ. Sci.* 2013**,** *6* (4), 1185-1191.

(98) Hu, L.; Choi, J. W.; Yang, Y.; Jeong, S.; La Mantia, F.; Cui, L.-F.; Cui, Y., Highly conductive paper for energy-storage devices. *Proc. Natl. Acad. Sci.* 2009**,** *106* (51), 21490-21494.

(99) Hu, L.; Pasta, M.; Mantia, F. L.; Cui, L.; Jeong, S.; Deshazer, H. D.; Choi, J. W.; Han, S. M.; Cui, Y., Stretchable, Porous, and Conductive Energy Textiles. *Nano Lett.* 2010**,** *10* (2), 708-714.

(100) Jost, K.; Perez, C. R.; McDonough, J. K.; Presser, V.; Heon, M.; Dion, G.; Gogotsi, Y., Carbon coated textiles for flexible energy storage. *Energy Environ. Sci.* 2011**,** *4* (12), 5060-5067.

(101) Chen, W.; Rakhi, R. B.; Hu, L.; Xie, X.; Cui, Y.; Alshareef, H. N., High-Performance Nanostructured Supercapacitors on a Sponge. *Nano Lett.* 2011**,** *11* (12), 5165-5172.

(102) Kang, E. T.; Neoh, K. G.; Tan, K. L., Polyaniline: A polymer with many interesting intrinsic redox states. *Prog. Polym. Sci.* 1998**,** *23* (2), 277-324.

(103) Ryu, K. S.; Kim, K. M.; Park, N.-G.; Park, Y. J.; Chang, S. H., Symmetric redox supercapacitor with conducting polyaniline electrodes. *J. Power Sources* 2002**,** *103* (2), 305-309.

(104) Amado, F. D. R.; Rodrigues Jr, L. F.; Rodrigues, M. A. S.; Bernardes, A. M.; Ferreira, J. Z.; Ferreira, C. A., Development of polyurethane/polyaniline membranes for zinc recovery through electrodialysis. *Desalination* 2005**,** *186* (1–3), 199-206.

(105) Huang, Z.-M.; Zhang, Y. Z.; Kotaki, M.; Ramakrishna, S., A review on polymer nanofibers by electrospinning and their applications in nanocomposites. *Compos. Sci. Technol.* 2003**,** *63* (15), 2223-2253.

(106) Agarwal, S.; Greiner, A.; Wendorff, J. H., Electrospinning of Manmade and Biopolymer Nanofibers—Progress in Techniques, Materials, and Applications. *Adv. Funct. Mater.* 2009**,** *19* (18), 2863-2879.

(107) Wang, H.-G.; Yuan, S.; Ma, D.-L.; Zhang, X.-B.; Yan, J.-M., Electrospun materials for lithium and sodium rechargeable batteries: from structure evolution to electrochemical performance. *Energy Environ. Sci.* 2015**,** *8* (6), 1660-1681.

(108) Gao, J.; Hu, M.; Dong, Y.; Li, R. K. Y., Graphite-Nanoplatelet-Decorated Polymer Nanofiber with Improved Thermal, Electrical, and Mechanical Properties. *ACS Appl. Mater. Interfaces* 2013**,** *5* (16), 7758-7764.

(109) Hsiao, S.-T.; Ma, C.-C. M.; Tien, H.-W.; Liao, W.-H.; Wang, Y.-S.; Li, S.-M.; Chuang, W.-P., Preparation and characterization of silver nanoparticle-reduced graphene oxide decorated

electrospun polyurethane fiber composites with an improved electrical property. *Compos. Sci. Technol.* 2015**,** *118,* 171-177.

(110) Ge, J. J.; Hou, H.; Li, Q.; Graham, M. J.; Greiner, A.; Reneker, D. H.; Harris, F. W.; Cheng, S. Z. D., Assembly of Well-Aligned Multiwalled Carbon Nanotubes in Confined Polyacrylonitrile Environments: Electrospun Composite Nanofiber Sheets. *J. Am. Chem. Soc.* 2004**,** *126* (48), 15754-15761.

(111) Hou, H.; Ge, J. J.; Zeng, J.; Li, Q.; Reneker, D. H.; Greiner, A.; Cheng, S. Z. D., Electrospun Polyacrylonitrile Nanofibers Containing a High Concentration of Well-Aligned Multiwall Carbon Nanotubes. *Chem. Mater.* 2005**,** *17* (5), 967-973.

(112) Sen, R.; Zhao, B.; Perea, D.; Itkis, M. E.; Hu, H.; Love, J.; Bekyarova, E.; Haddon, R. C., Preparation of Single-Walled Carbon Nanotube Reinforced Polystyrene and Polyurethane Nanofibers and Membranes by Electrospinning. *Nano Lett.* 2004**,** *4* (3), 459-464.

(113) Shi, Y.; Peng, L.; Ding, Y.; Zhao, Y.; Yu, G., Nanostructured conductive polymers for advanced energy storage. *Chem. Soc. Rev.* 2015**,** *44* (19), 6684-6696.

(114) Wang, L.; Lu, X.; Lei, S.; Song, Y., Graphene-based polyaniline nanocomposites: preparation, properties and applications. *J. Mater. Chem. A* 2014**,** *2* (13), 4491-4509.

(115) Liu, T.; Finn, L.; Yu, M.; Wang, H.; Zhai, T.; Lu, X.; Tong, Y.; Li, Y., Polyaniline and Polypyrrole Pseudocapacitor Electrodes with Excellent Cycling Stability. *Nano Lett.* 2014**,** *14* (5), 2522-2527.

(116) Song, Y.; Liu, T.-Y.; Xu, X.-X.; Feng, D.-Y.; Li, Y.; Liu, X.-X., Pushing the Cycling Stability Limit of Polypyrrole for Supercapacitors. *Adv. Funct. Mater.* 2015**,** *25* (29), 4626-4632.

(117) Ryu, Y. J.; Kim, H. Y.; Lee, K. H.; Park, H. C.; Lee, D. R., Transport properties of electrospun nylon 6 nonwoven mats. *European Polymer Journal* 2003**,** *39* (9), 1883-1889.

(118) Fan, Q.; Zhang, X.; Qin, Z., Preparation of Polyaniline/Polyurethane Fibers and Their Piezoresistive Property. *J. Macromol. Sci., Part B* 2012**,** *51* (4), 736-746.

(119) Tijing, L. D.; Park, C.-H.; Choi, W. L.; Ruelo, M. T. G.; Amarjargal, A.; Pant, H. R.; Im, I.-T.; Kim, C. S., Characterization and mechanical performance comparison of multiwalled carbon nanotube/polyurethane composites fabricated by electrospinning and solution casting. *Composites, Part B* 2013**,** *44* (1), 613-619.

(120) Rangel-Vázquez, N. A.; Salgado-Delgado, R.; García-Hernández, E.; Mendoza-Martínez, A. M., Characterization of Copolymer Based in Polyurethane and Polyaniline (PU/PANI). *J. Mex. Chem. Soc.* 2009**,** *53* (4), 248-252.

(121) Wang, T.-L.; Yang, C.-H.; Shieh, Y.-T.; Yeh, A.-C., Synthesis and properties of conducting organic/inorganic polyurethane hybrids. *Eur. Polym. J.* 2009**,** *45* (2), 387-397.

(122) Gogotsi, Y.; Simon, P., True Performance Metrics in Electrochemical Energy Storage. *Science* 2011**,** *334* (6058), 917-918.

(123) Khomenko, V.; Frackowiak, E.; Béguin, F., Determination of the specific capacitance of conducting polymer/nanotubes composite electrodes using different cell configurations. *Electrochim. Acta* 2005**,** *50* (12), 2499-2506.

(124) Li, Z.-F.; Zhang, H.; Liu, Q.; Liu, Y.; Stanciu, L.; Xie, J., Covalently-grafted polyaniline on graphene oxide sheets for high performance electrochemical supercapacitors. *Carbon* 2014**,** *71*, 257-267.

(125) Kuang, H.; Cao, Q.; Wang, X.; Jing, B.; Wang, Q.; Zhou, L., Influence of the reaction temperature on polyaniline morphology and evaluation of their performance as supercapacitor electrode. *J. Appl. Polym. Sci.* 2013**,** *130* (5), 3753-3758.

(126) Zhu, Y.; Murali, S.; Stoller, M. D.; Ganesh, K. J.; Cai, W.; Ferreira, P. J.; Pirkle, A.; Wallace, R. M.; Cychosz, K. A.; Thommes, M.; Su, D.; Stach, E. A.; Ruoff, R. S., Carbon-Based Supercapacitors Produced by Activation of Graphene. *Science* 2011**,** *332* (6037), 1537-1541.

(127) Valentová, H.; Stejskal, J., Mechanical properties of polyaniline. *Synthetic Metals* 2010**,** *160* (7–8), 832-834.

(128) Xia, C.; Chen, W.; Wang, X.; Hedhili, M. N.; Wei, N.; Alshareef, H. N., Highly Stable Supercapacitors with Conducting Polymer Core-Shell Electrodes for Energy Storage Applications. *Adv. Energy Mater.* 2015**,** *5* (8), n/a-n/a.

(129) Hao, G.-P.; Hippauf, F.; Oschatz, M.; Wisser, F. M.; Leifert, A.; Nickel, W.; Mohamed-Noriega, N.; Zheng, Z.; Kaskel, S., Stretchable and Semitransparent Conductive Hybrid Hydrogels for Flexible Supercapacitors. *ACS Nano* 2014**,** *8* (7), 7138-7146.

(130) Wang, K.; Zhang, X.; Li, C.; Sun, X.; Meng, Q.; Ma, Y.; Wei, Z., Chemically Crosslinked Hydrogel Film Leads to Integrated Flexible Supercapacitors with Superior Performance. *Adv. Mater.* 2015**,** *27* (45), 7451-7457.

(131) Wang, H.; Yang, Y.; Liang, Y.; Robinson, J. T.; Li, Y.; Jackson, A.; Cui, Y.; Dai, H., Graphene-Wrapped Sulfur Particles as a Rechargeable Lithium–Sulfur Battery Cathode Material with High Capacity and Cycling Stability. *Nano Lett.* 2011**,** *11* (7), 2644-2647.

(132) Gao, H.; Zhou, W.; Jang, J.-H.; Goodenough, J. B., Cross-Linked Chitosan as a Polymer Network Binder for an Antimony Anode in Sodium-Ion Batteries. *Adv. Energy Mater.* 2016**,** *6* (6), n/a-n/a.

(133) Destaye, A. G.; Lin, C.-K.; Lee, C.-K., Glutaraldehyde Vapor Cross-linked Nanofibrous PVA Mat with in Situ Formed Silver Nanoparticles. *ACS Appl. Mater. Interfaces* 2013**,** *5* (11), 4745-4752.

(134) Baker, C. O.; Huang, X.; Nelson, W.; Kaner, R. B., Polyaniline nanofibers: broadening applications for conducting polymers. *Chemical Society Reviews* 2017**,** *46* (5), 1510-1525.

(135) Reis, E. F. d.; Campos, F. S.; Lage, A. P.; Leite, R. C.; Heneine, L. G.; Vasconcelos, W. L.; Lobato, Z. I. P.; Mansur, H. S., Synthesis and characterization of poly (vinyl alcohol) hydrogels and hybrids for rMPB70 protein adsorption. *Mat. Res.* 2006**,** *9*, 185-191.

(136) Wang, C.; Zheng, Y.; Qiao, K.; Xie, Y.; Zhou, X., An environmentally friendly preparation and characterization of waterborne polyurethane hydrogels by polyvinyl alcohol physical cross-linking to improve water absorption. *RSC Adv.* 2015**,** *5* (90), 73882-73891.

List of Publications in Ph.D. Research

Journal papers:

- **Khosrozadeh, A.**; Sing, G.; Wang, Q.; Xing, M., Janus Nanofibrous Worm-Like Electrode as Elastic Buffer Leading to Supercapacitor of Extraordinary Cycling Stability and Shape Memory Actuator. *Submitted*.
- **Khosrozadeh, A.**; Darabi, M. A.; Wang, Q.; Xing, M., Polyaniline nanoflowers grown on vibration-isolator-mimetic polyurethane nanofibers for flexible supercapacitors with prolonged cycle life. *Journal of Materials Chemistry A* 2017, 5 (17), 7933-7943.
- Darabi, M. A.; **Khosrozadeh, A.**; Mbeleck, R.; Liu, Y.; Chang, Q.; Jiang, J.; Cai, J.; Wang, Q.; Luo, G.; Xing, M., Skin-Inspired Multifunctional Autonomic-Intrinsic Conductive Self-Healing Hydrogels with Pressure Sensitivity, Stretchability, and 3D Printability. *Advanced Materials* 2017, n/a-n/a.
- **Khosrozadeh, A.**; Darabi, M. A.; Xing, M.; Wang, Q., Flexible Electrode Design: Fabrication of Freestanding Polyaniline-Based Composite Films for High-Performance Supercapacitors. *ACS Applied Materials & Interfaces* 2016, 8 (18), 11379-11389.
- Darabi, M. A.; **Khosrozadeh, A.**; Wang, Q.; Xing, M., Gum Sensor: A Stretchable, Wearable, and Foldable Sensor Based on Carbon Nanotube/Chewing Gum Membrane. *ACS Applied Materials & Interfaces* 2015, 7 (47), 26195-26205.

- **Khosrozadeh, A.**; Darabi, M. A.; Xing, M.; Wang, Q., Flexible Cellulose-Based Films of Polyaniline–Graphene–Silver Nanowire for High-Performance Supercapacitors. *Journal of Nanotechnology in Engineering and Medicine* 2015, 6 (1), 011005-011005.
- **Khosrozadeh, A.**; Xing, M.; Wang, Q., A High-Capacitance Solid-State Supercapacitor Based on Free-Standing Film of Polyaniline and Carbon Particles. *Applied Energy* 2015, 153 (0), 87-93.
- **Khosrozadeh, A.**; Wang, Q.; Varadan, V. K., Molecular Simulations on Separation of Atoms with Carbon Nanotubes in Torsion. *Computational Materials Science* 2014, 81, 280-283.

Conference papers:

- **Khosrozadeh, A.**; Xing, M.; Wang, Q., Flexible Polyaniline-Based Composite Films for High-Performance Supercapacitors, ICEMA 2015: 17th International Conference on Engineering Materials and Applications, Istanbul, (2015).
- **Khosrozadeh, A.**; Wang, Q.; Xing, M., A High-Capacitance Solid-State Supercapacitor Based on Polyaniline and Ground Carbon Fibers, Proceedings of the 14th IEEE International Conference on Nanotechnology, Toronto, (2014) 602-607.